

INVESTIGATION OF THE DIRECT-CAPTURE REACTION, $\text{He}^3(\alpha, \gamma)\text{Be}^7$

Thesis by

Peter Donald MacDougall Parker

In Partial Fulfillment of the Requirements

For the Degree of

Doctor of Philosophy

California Institute of Technology

Pasadena, California

1963

ACKNOWLEDGEMENTS

The author is happy to express his thanks to all the faculty, the technical staff and the graduate students of the Kellogg Radiation Laboratory for their assistance and encouragement that have made this undertaking not only possible, but also enjoyable. Special thanks are due to Professor R. W. Kavanagh for his guidance and stimulus and for his assistance which carried this experiment over many pitfalls. To Dr. T. A. Tombrello special thanks are due for his continuing assistance without which Part II of this thesis would hardly exist. It is also a pleasure to acknowledge the assistance of my wife, Judy, with many of the hum-drum but time-consuming aspects of this work.

Thanks for financial assistance go to the National Science Foundation, the Danforth Foundation, the Woodrow Wilson Foundation and the California Institute of Technology for fellowship grants during the conduct of this work, as well as to the Office of Naval Research and the United States Atomic Energy Commission for the actual support of this experiment.

ABSTRACT

The absolute cross section for the reaction, $\text{He}^3(\alpha, \gamma) \text{Be}^7$, has been measured over the range of energies $181 \leq E_{\text{cm}} \leq 2493$ keV, using a gas target behind a thin nickel entrance foil. Calibrated NaI(Tl) crystals were used to detect the prompt capture radiation. Over the entire energy region the measured total cross section and branching ratio confirm theoretical predictions based on calculations neglecting the contributions to the matrix elements from the region inside the nuclear radius. These cross-section measurements have been used to obtain a new value for the low-energy cross-section factor, S_0 , for this reaction ($S_0 \approx 0.47 \pm .07$ keV barns), and this value has been used to reevaluate the importance of the $\text{He}^3(\alpha, \gamma)\text{Be}^7$ reaction in the termination of the proton-proton chain in nuclear astrophysics.

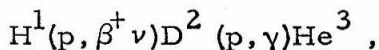
TABLE OF CONTENTS

PART	TITLE	PAGE
I	INTRODUCTION	1
II	THEORETICAL DISCUSSION	4
III	EXPERIMENTAL APPARATUS AND PROCEDURE	16
	A. Target System	16
	B. Detection System	22
	C. Energy Determination	25
	D. Coincidence Measurement	30
	E. Conclusion	31
IV	ANALYSIS OF DATA	34
	A. Conversion of Gamma-Ray Spectra to Absolute Cross Sections	34
	B. Error Analysis.	46
	1. E_{cm}	46
	2. ρ	47
	3. σ_{total}	50
	4. $S(E)$	53
V	RESULTS	54
	A. Nuclear Physical	54
	B. Astrophysical	59
APPENDIX I:	Gamma-Ray Spectrometry	68
	A. Efficiency Calculations	68
	B. Response Function Determinations	74
	1. Characteristics of Gamma-Ray NaI(Tl) Response Functions	74

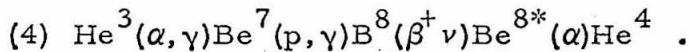
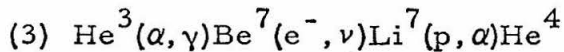
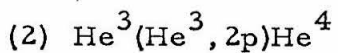
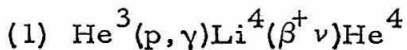
PART	TITLE	PAGE
	2. Experimental Measurement of Response Functions	79
	3. Calculation of Coincidence-Summing Response Functions	82
	C. Photo-Fraction Measurements	83
REFERENCES	90
TABLES	93
FIGURES	96

I. INTRODUCTION

In the study of nuclear astrophysics, one of the important series of nuclear reactions is the proton-proton reaction chain for converting hydrogen into helium. Once three protons have been converted into He^3 by the reactions,



there are four ways that the chain might be completed by converting the He^3 into He^4 :



Termination (1) has been studied (Bashkin *et al.*, 1959) with the conclusions that Li^4 is not particle stable and hence that termination (1) is not an important way to convert He^3 into He^4 . The relative importance of terminations (3) and (4) has been investigated by Kavanagh (1960) with the conclusion that termination (4) will dominate termination (3) only in stars with effective operating temperatures greater than 20×10^6 °K. The relative importance of terminations (2) and (3) (or (2) and (4)) depends on the relative rates of the two He^3 -burning reactions. The importance of determining the roles of terminations (2) and (3) lies in the fact that

(2) requires the production of two He³'s, via the extremely slow H¹(p, β⁺ ν)D² reaction, for each He⁴ produced, while termination (3) requires only one He³ for every He⁴ produced. Thus, in a star, with any appreciable amount of He⁴, operating entirely on (3) the He⁴ production rate will be doubled, and the rate of energy generation almost doubled (x 1.95, due to the additional neutrino losses in the Be⁷ decay), compared to a star operating entirely on termination (2). Hence, there is interest in investigating the relative rates of the two reactions, He³(He³, 2p)He⁴ and He³(α, γ)Be⁷, and, in particular, in determining the magnitudes of their cross sections at energies of the order of 20 keV. These arguments indicate one of the main reasons for investigating the reaction, He³(α, γ)Be⁷.

Another important reason is supplied by the theoretical interest in the class of "direct-capture" reactions of which this reaction is a member. Such reactions may be qualitatively visualized as a process wherein the incident particle is captured non-resonantly from a configuration of definite angular momentum, decaying by gamma-ray emission to a lower lying nuclear level. Calculations of the behavior of the cross sections of such reactions have been developed independently by Christy and Duck (1961) and Tombrello and Phillips (1961). In the reaction He³(α, γ)Be⁷, the entire range of bombarding energy from 0.0 to almost 7.0 MeV is free from any interfering nuclear levels, and thus this reaction also provides an excellent opportunity for studying the validity of the theories noted above.

Because of these reasons, this reaction has not gone unnoticed

until the present investigation. In 1957, on the basis of estimates by Salpeter (1952) as to the mean reaction lifetime of He^3 in stars, Cameron (1957) calculated a "zero-energy cross-section factor", S_0 , (Burbidge et al., 1957) of 0.6 eV-barns for this reaction. Holmgren and Johnston (1959) investigated the reaction experimentally and arrived at a value for S_0 of 1.2 keV-barns, (2000x larger than the previous estimates). On the basis of this determination, Fowler (1958) has shown that for a star with equal masses of hydrogen and helium the $\text{He}^3(\alpha, \gamma)\text{Be}^7$ terminations will dominate the $\text{He}^3(\text{He}^3, 2p)\text{He}^4$ termination when the temperature is greater than 12.5×10^6 °K.

In the summer of 1959, however, Griffiths (1959) indicated that preliminary measurements of the $\text{H}^3(\alpha, \gamma)\text{Li}^7$ reaction (later substantiated - Griffiths et al., 1961) showed a marked disagreement with those measured by Holmgren and Johnston (1959) at the same time as their work on the $\text{He}^3(\alpha, \gamma)\text{Be}^7$ reaction. Griffiths' work indicated cross sections for $\text{H}^3(\alpha, \gamma)\text{Li}^7$ approximately a factor of two larger than those reported by Holmgren and Johnston. A preliminary investigation of the $\text{He}^3(\alpha, \gamma)\text{Be}^7$ reaction in 1960 by this author indicated further disagreements with the measurements of Holmgren and Johnston. In this case, however, the cross sections of Holmgren and Johnston were a factor of two larger than the new results.

It was in the light of these disagreements and in view of the interest in and importance of the reaction, as noted above, that the following investigation of the $\text{He}^3(\alpha, \gamma)\text{Be}^7$ reaction was carried out.

II. THEORETICAL DESCRIPTION

A reasonably successful theoretical description of the class of direct-capture reactions has been developed independently by Christy and Duck (1961) and Tombrello and Phillips (1961). The basis of calculations made on this description is the "extra-nuclear" approximation under which all contributions to the matrix elements from the region inside the nuclear radius are neglected. This allows the wave functions for the initial and final states to be expressed simply in terms of free- and bound-state Coulomb wave functions, without any need to consider the problem of nuclear forces. Such an approximation, neglecting the interior contributions, will, of course, not always be valid, especially in the neighborhood of nuclear resonances, or levels in the compound nucleus. It will, however, tend to be valid in regions removed from such resonances and where the phase shifts of the principal ℓ -waves involved in the capture can be described in terms of hard-sphere phase shifts over large energy ranges, indicating little or no overlap in the nuclear region. These conditions are reasonably well satisfied in the region of Be^7 between the $(\text{He}^3 + \text{He}^4)$ threshold at 1.587 MeV excitation and the neighborhood of the $7/2^-$ state at 4.54 MeV excitation, and therefore a study of the $\text{He}^3(\alpha, \gamma)\text{Be}^7$ reaction in this region is a good way to test the validity of this description.

In addition, rather thorough investigations of the $\text{He}^4(\text{He}^3, \text{He}^3)\text{He}^4$ elastic scattering in this region (Miller and Phillips, 1958; Jones et al., 1962; Tombrello and Parker, 1962) have provided accurate determinations of the various phase shifts necessary for an accurate specification of the

initial-state wave functions needed for the calculations described below. For these calculations the extra-nuclear approximation is retained, but the previous descriptions are expanded to take into account the contributions from all ℓ -waves up through $\ell = 3$.

In general, (Moszkowski, 1955 and Weidenmuller, 1962) we can write the differential cross section from Fermi's golden rule as

$$\frac{d\sigma(\theta)}{d\Omega} = \frac{2\pi}{\hbar v} \frac{dn(E)}{d\Omega} \sum_{m_i, m_f, p} \frac{1}{2s+1} \left| \langle \psi_f^{m_f} | H_{int} | \psi_i^{m_i} \rangle \right|^2$$

where $n(E)$ is the density of states function,

v is the velocity of the incident particle,

p is the polarization of the emitted gamma ray,

s is the channel spin of the system,

$\psi_f^{m_f}$ is the final-state wave function with magnetic quantum number, m_f ,

$\psi_i^{m_i}$ is the initial-state wave function with magnetic quantum number, m_i , and

where the interaction Hamiltonian for a gamma ray with a nuclear system is

$$H_{int} = -\frac{1}{c} \vec{j} \cdot \vec{A}$$

where \vec{j} is the nuclear-charge current vector, and

\vec{A} is the vector potential of the gamma-ray field.

Since we are considering the case where a photon with polarization (p) is created, we will take just the $\vec{A}^* P$ part of this Hamiltonian. Normalizing the total energy to $\hbar\omega$ in a volume, V , we can write the

electric field strength, \vec{E} , as

$$\vec{E}^* \approx \left(\frac{2\pi\hbar\omega}{V}\right)^{\frac{1}{2}} \vec{\chi}_1^* e^{-i\vec{K} \cdot \vec{r}}$$

$$\vec{A} = \frac{1}{iK} \vec{E}$$

where $\vec{\chi}_1^*$ is a spherical unit vector in the direction p, and
where \vec{K} is the gamma-ray momentum, $K = \frac{\omega}{c}$.

Therefore,

$$\vec{A}^* \approx -\frac{c}{i\omega} \left(\frac{2\pi\hbar\omega}{V}\right)^{\frac{1}{2}} \vec{\chi}_1^* e^{-i\vec{K} \cdot \vec{r}}$$

$$H_{int} \approx \left(\frac{1}{i\omega}\right) \left(\frac{2\pi\hbar\omega}{V}\right)^{\frac{1}{2}} \vec{j} \cdot \vec{\chi}_1^* e^{-i\vec{K} \cdot \vec{r}}$$

$\vec{\chi}_1^* e^{-i\vec{K} \cdot \vec{r}}$ can now be expanded in multipoles as,

$$\vec{\chi}_1^* e^{-i\vec{K} \cdot \vec{r}} = \sum_{L=1}^{\infty} \sum_{M=-L}^{L} \sqrt{2\pi(2L+1)} (-i)^L D_L^{*M, p} \left[\vec{A}_L^{*M(m)} - ip \vec{A}_L^{*M(e)} \right]$$

where $D_L^{*M, p}$ is an element of the rotation matrix and where $\vec{j} \cdot \vec{A}_L^{*M(e)}$
can now be written, via Siegert's Theorem, as

$$\vec{j} \cdot \vec{A}_L^{*M(e)} = -ice \sqrt{\frac{L+1}{L}} j_L(Kr) Y_L^{*M}$$

$$Kr \ll 1 \quad -ice \sqrt{\frac{L+1}{L}} \frac{(Kr)^L}{(2L+1)!!} Y_L^{*M}$$

In the same long wavelength approximation, we can write (Moszkowski,
1955)

$$\vec{j} \cdot \vec{A}_L^{*M(m)} = -ic \frac{K^L}{(2L+1)!!} \sqrt{\frac{L+1}{L}} \left[\frac{e\hbar}{m_p c} \frac{1}{L+1} \vec{L} \cdot (\text{grad } r^L Y_L^{*M})^* + \frac{e\hbar}{2m_p c} \vec{\mu} \cdot (\text{grad } r^L Y_L^{*M})^* \right]$$

where m_p is the mass of the proton;

μ is the magnetic moment in nuclear magnetons,

\vec{L} is the angular momentum operator, and

$\vec{\sigma}$ is the Pauli spin operator.

For M1 this reduces to

$$\vec{j} \cdot \vec{A}_1^{*M}(m) = (-1)^M (-i) \frac{e\hbar K}{m_p} \sqrt{\frac{1}{24\pi}} (\vec{L} + \mu \vec{\sigma}) \cdot \vec{\chi}_1^{-M}$$

where $\vec{\chi}_1^{-M}$ is again a spherical unit vector.

Hence, our Hamiltonian may now be written out explicitly as follows, limiting our interest to E1, M1 and E2 transitions, since we have indicated that we will consider only partial waves with $\ell \leq 3$:

$$H_{int} = \left(\frac{2\pi\hbar}{\omega V} \right)^{\frac{1}{2}} \sum_M \left\{ (-1)^M (i) \frac{e\hbar K}{2m_p} D_1^{*M,p} (\vec{L} + \mu \vec{\sigma}) \cdot \vec{\chi}_1^{-M} \right. \\ \left. + \sqrt{\frac{4\pi}{3}} pce D_1^{*M,p} K r Y_1^{*M} \right. \\ \left. - ipce \sqrt{\frac{\pi}{15}} D_2^{*M,p} K^2 r^2 Y_2^{*M} \right\} .$$

Factoring out the common constants, $\left[iceK \left(\frac{2\pi\hbar}{\omega V} \right)^{\frac{1}{2}} \right]$, and removing them from the matrix element we are able to write, where the density of states is

$$\frac{dn(E)}{d\Omega} = \frac{K^2 V}{8\pi^3 \hbar c} ,$$

$$\frac{d\sigma(\theta)}{d\Omega} = \frac{e^2 K^3}{2\pi \hbar v} \sum_{m_i, m_f, p} \frac{1}{2s+1} \left| \langle \psi_f^{m_f} | H'_{int} | \psi_i^{m_i} \rangle \right|^2$$

where H'_{int} is now expressed as

$$H_{int}^i = \sum_M \left\{ (-1)^M \frac{\hbar}{2m_p c} D_1^{*M,p} (\vec{L} + \mu \vec{\sigma}) \cdot \vec{x}_1^{-M} - i \sqrt{\frac{4\pi}{3}} p D_1^{*M,p} r Y_1^{*M} - \sqrt{\frac{\pi}{15}} p D_2^{*M,p} K r^2 Y_2^{*M} \right\}$$

Actually each of these expressions contains an implicit summation over the contributions of all the nucleons in the system. Hence, we should really write

$$(\vec{L} + \mu \vec{\sigma}) \rightarrow \sum_j \left(\frac{z_j}{A_j} \vec{L}_j + \mu_j \vec{\sigma}_j \right)$$

$$r Y_1^{*M} \rightarrow \sum_j z_j r_j Y_1^{*M}(\theta_j, \phi_j), \text{ etc.}$$

This implicit summation can be made explicit, considering two particles, i.e. a He³ and a He⁴ nucleus, and expanding in the center-of-mass system. In this way we can write

$$\sum_j \left(\frac{z_j}{A_j} \vec{L}_j + \mu_j \vec{\sigma}_j \right) = \left(\frac{z_1}{A_1^2} + \frac{z_2}{A_2^2} \right) \frac{A_1 A_2}{A_1 + A_2} \vec{L} + \mu_1 \vec{\sigma}_1 + \mu_2 \vec{\sigma}_2$$

$$\sum_j z_j r_j Y_1^{*M}(\theta_j, \phi_j) = \left(\frac{A_1 A_2}{A_1 + A_2} \right) \left(\frac{z_1}{A_1} - \frac{z_2}{A_2} \right) r Y_1^{*M}(\theta, \phi)$$

$$\sum_j z_j r_j^2 Y_2^{*M}(\theta_j, \phi_j) = \left(\frac{A_1 A_2}{A_1 + A_2} \right)^2 \left(\frac{z_1}{A_1^2} + \frac{z_2}{A_2^2} \right) r^2 Y_2^{*M}(\theta, \phi), \text{ etc.}$$

where r , θ and ϕ are now the relative coordinates of the two particles, and we can now write H_{int}^i in the form

$$H_{int}^i = \sum_M \left\{ (-1)^M \frac{\hbar}{2m_p c} D_1^{*M,p} \left[\frac{A_1 A_2}{A_1 + A_2} \left(\frac{z_1}{A_1} - \frac{z_2}{A_2} \right) \vec{L} + \mu_1 \vec{\sigma}_1 + \mu_2 \vec{\sigma}_2 \right] \cdot \vec{\chi}_1^M \right. \\ - i \sqrt{\frac{4\pi}{3}} p D_1^{*M,p} \left(\frac{A_1 A_2}{A_1 + A_2} \right) \left(\frac{z_1}{A_1} - \frac{z_2}{A_2} \right) r Y_1^{*M} \\ \left. - \sqrt{\frac{\pi}{15}} p D_2^{*M,p} \left(\frac{A_1 A_2}{A_1 + A_2} \right)^2 \left(\frac{z_1}{A_1} - \frac{z_2}{A_2} \right) K r^2 Y_2^{*M} \right\}$$

where z_i is the charge of the i^{th} particle in units of e ,

where A_i is the mass of the i^{th} particle in proton-mass units and where these terms correspond to M1, E1 and E2 radiation respectively.

The differential cross section was calculated from the expression

$$\frac{d\sigma(\theta)}{d\Omega} = \frac{e^2 K^3}{2\pi\hbar v} \sum_{m_i, m_f, p} \frac{1}{2s+1} \left| \langle \psi_f^{m_f} | H_{int}^i | \psi_i^{m_i} \rangle \right|^2$$

using the above form of the interaction Hamiltonian and the following initial-state and final-state wave functions.

The initial-state wave function outside the nucleus may be written in the usual way as a partial wave expansion of the incident Coulomb distorted plane wave plus the outgoing Coulomb distorted spherical wave.

$$\psi_i^{m_i} = \sum_{\ell=0}^{\infty} \sqrt{4\pi(2\ell+1)} (i)^\ell \frac{e^{i\alpha_\ell}}{kr} \left\{ \frac{\ell+1}{2\ell+1} e^{i\delta_\ell^+} R_\ell^+ + \frac{\ell}{2\ell+1} e^{i\delta_\ell^-} R_\ell^- \right\} Y_\ell^0 X_{\frac{1}{2}}^{m_i} \\ + \sum_{\ell=1}^{\infty} \sqrt{\frac{4\pi\ell(\ell+1)}{2\ell+1}} (i)^\ell \frac{e^{i\alpha_\ell}}{kr} \left\{ e^{i\delta_\ell^+} R_\ell^+ - e^{i\delta_\ell^-} R_\ell^- \right\} Y_\ell^{2m_i} X_{\frac{1}{2}}^{-m_i}$$

where

$$R_\ell^\pm = \cos \delta_\ell^\pm F_\ell(kr) + \sin \delta_\ell^\pm G_\ell(kr),$$

$F_\ell(kr)$ and $G_\ell(kr)$ are the regular and irregular Coulomb functions,

$$\alpha_\ell = \sum_{s=1}^{\ell} \tan^{-1} (\eta/s),$$

$$\eta = z_1 z_2 e^2 / \hbar v, \text{ and}$$

δ_ℓ^\pm are the phase shifts for $j = \ell \pm \frac{1}{2}$.

The actual phase shifts used for these calculations were taken from the elastic-scattering work cited above and are listed in Table II. These experimentally determined phase shifts can be described as follows:

- (1) δ_0^- is consistent with the hard-sphere, s-wave phase shift for $R_0 = 2.80$ f. over the entire range of this experiment.
- (2) δ_1^+ and δ_1^- are negative but are not consistent with such a hard-sphere description. The values of these phases were taken from the elastic-scattering experiments, down to $E_\alpha = 3.00$ MeV. At that point the p-wave, hard-sphere phase shift was normalized to these experimental values and used to determine the p-wave phase shifts at lower energies.
- (3) δ_2^+ and δ_2^- are both consistent with the $R_0 = 2.80$ f. hard-sphere, d-wave phase shift over the entire range of this experiment. In agreement with this, $\delta_2^+ = \delta_2^-$, and the initial wave function was simplified accordingly.
- (4) δ_3^+ and δ_3^- are not consistent with a hard-sphere description but are governed by the two $\ell = 3$ resonances just above the range of the present experiment.

The final-state wave function may be written in the following expansion, considering our final states as a p-wave He^3 orbiting around a He^4 :

$$\psi_f^{m_f} = \frac{U_f(r)}{r} \left\{ \langle l m_f - \frac{1}{2}, \frac{1}{2} / J_f m_f \rangle Y_l^{m_f - \frac{1}{2}} X_{\frac{1}{2}} + \langle l m_f + \frac{1}{2}, \frac{1}{2} - \frac{1}{2} / J_f m_f \rangle Y_l^{m_f + \frac{1}{2}} X_{\frac{1}{2}} \right\}$$

where $U_f(r)$ is taken to be the Whittaker function, $W_{\alpha, \ell}(kr)$, the bound-state Coulomb function,

$$W_{\alpha, \ell}(kr) = \frac{(2kr)^{-\alpha} e^{-kr}}{(\ell + \alpha)!} \int_0^\infty t^{\ell + \alpha} e^{-t} \left(1 + \frac{t}{2kr}\right)^{\ell - \alpha} dt$$

where

$$\alpha = z_1 z_2 e^2 \mu / \hbar^2 k ,$$

$$k = \sqrt{2\mu E_B / \hbar^2} ,$$

$$\mu = A_1 A_2 / (A_1 + A_2) , \text{ and}$$

E_B is the binding energy of the final state.

The normalization of $U_f(r)$ is defined in terms of the reduced width, θ^2 , such that if the Wigner limit is taken to be $3\hbar^2 / 2\mu R_o^2$, then

$$\theta^2 \equiv \frac{R_o U_f^2(R_o)}{3 \int_{R_o}^\infty U_f^2(r) dr}$$

where R_o is the nuclear radius.

Combining $\psi_i^{m_i}$, $\psi_f^{m_f}$ and H_{int} and performing the necessary algebra, one can reduce the expression for $\frac{d\sigma(\theta)}{d\Omega}$ to the form (Tombrello and Parker, 1962a),

$$\frac{d\sigma(\theta)}{d\Omega} = \sigma_o (1 + a_1 \cos \theta + a_2 \cos^2 \theta + a_3 \cos^3 \theta + a_4 \cos^4 \theta)$$

from which σ_{total} can be evaluated as

$$\sigma_{\text{total}} = 4\pi\sigma_0 + \frac{4\pi}{3}\sigma_0 a_2 + \frac{4\pi}{5}\sigma_0 a_4$$

The coefficients, (σ_0 , a_1 , a_2 , a_3 and a_4), are complicated functions of the various radial integrals involved. The evaluation of these integrals and their combination to form the various coefficients were performed on the Burroughs' 220 computer.

It is probably worthwhile to pause a moment here to consider briefly the manner in which these radial integrals were evaluated. These integrals were all of the forms,

$$\int_{R_0}^{\infty} U_f r^a F_\ell dr \quad 0 \leq a \leq 2$$
$$0 \leq \ell \leq 3$$
$$\int_{R_0}^{\infty} U_f r^a G_\ell dr$$

Rather than feed the individual wave functions into the computer for each case, the computer was programmed to generate U_f , F_ℓ and G_ℓ for the various integrals, using the method of finite-difference continuation. The wave functions thus generated checked to better than one per cent against the integral evaluation of $W_{\alpha, \ell}(kr)$ and the Coulomb function tables of Tubis (1957).

The method of finite-difference continuation utilizes the sum of the Taylor's series expansions for $f(x_0 + \delta)$ and $f(x_0 - \delta)$ to write, correct to terms of order (δ^6) ,

$$f(x_0 + \delta) \left[1 - \frac{\delta^2}{12} \frac{f''(x_0 + \delta)}{f(x_0 + \delta)} \right] + f(x_0 - \delta) \left[1 - \frac{\delta^2}{12} \frac{f''(x_0 - \delta)}{f(x_0 - \delta)} \right]$$

$$= f(x_0) \left[1 + \frac{5\delta^2}{6} \frac{f''(x_0)}{f(x_0)} \right] + O(\delta^6)$$

For the case of the unbound Coulomb functions, $F_\ell(\rho)$ and $G_\ell(\rho)$,

$$\frac{F_\ell''(\rho)}{F_\ell(\rho)} = (-1 + \frac{2\eta}{\rho} + \frac{\ell(\ell+1)}{\rho^2}) \text{ etc.,}$$

while for the bound-state Coulomb functions

$$\frac{U_f''(\rho)}{U_f(\rho)} = (1 + \frac{2\eta}{\rho} + \frac{\ell(\ell+1)}{\rho^2})$$

Since we will be performing our integrals in increments of r , where $\rho = kr$, (δ) in the expressions above becomes $(k\delta)$. Therefore, defining

$$q(r) = 1 - \frac{\delta^2 k^2}{12} \frac{f''(\rho)}{f(\rho)}$$

we can now rewrite the above as

$$f(r_0 + \delta) q(r_0 + \delta) + f(r_0 - \delta) q(r_0 - \delta) \approx f(r_0) \left[12 - 10q(r_0) \right]$$

where for the free Coulomb functions,

$$q(r) = 1 - \frac{\delta^2 k^2}{12} \left(-1 + \frac{2\eta}{\rho} + \frac{\ell(\ell+1)}{\rho^2} \right)$$

and for the bound-state Coulomb functions,

$$q(r) = 1 - \frac{\delta^2 k^2}{12} \left(1 + \frac{2\eta}{\rho} + \frac{\ell(\ell+1)}{\rho^2} \right)$$

For the bound state functions, two starting values were obtained at large radii, $R_o + N\delta$ and $R_o + (N-1)\delta$, using a WKB approximation (Tombrello and Phillips, 1961), and the complete wave function was then extrapolated inward to the nuclear radius by the method described above. Similarly, for the irregular, free Coulomb function, $G_\ell(\rho)$, a corrected WKB approximation (Tombrello and Phillips, 1961) was used to obtain two starting values and the rest of the function extrapolated inward as above.

For the case of the regular Coulomb function, $F_\ell(\rho)$, however, due to problems with the accumulation of error in the inward extrapolation, the process was reversed, and two starting values were calculated at R_o and $R_o + \delta$ from the expressions of Tubis (1957), and the rest of the function then extrapolated outwards in the manner of continuation described above.

Once the wave functions had thus been generated, the various radial integrals were carried out numerically by the computer, using the trapezoidal rule, and then combined to form the coefficients, (σ_o , a_1 , a_2 , a_3 and a_4).

Calculations of the sort described above were carried out for both of the possible gamma-ray transitions over the entire range of the experiment. The results of these calculations are presented in detail in Part V.

It is interesting to note in conclusion that the only possibly serious approximation that has been made in this discussion is the neglecting of the contributions to the matrix elements of the interior regions of the nucleus. That this is not, in fact, a serious approximation in the

present case is discussed in Part V. It is also worth noting that over the entire range of energies covered in this experiment there are only three parameters, (the nuclear radius, R_o , and the reduced widths of the two final states), which are free to be varied to make the theoretical predictions fit the experimental observations.

III. EXPERIMENTAL APPARATUS AND PROCEDURE

A. Target System.

In line with what was already discussed in the introduction, we would like to measure the cross section for the $\text{He}^3(\alpha, \gamma)\text{Be}^7$ reaction over as large a range of energies as possible. To accomplish this, incident alpha-particle beams of various energies were utilized from the 2-MV and 3-MV Van de Graaff accelerators in Kellogg and the 6-MV Tandem Van de Graaff accelerator in Sloan. With all three of these accelerators 90° magnetic analyzers were utilized to obtain relatively monoenergetic incident alpha-particle beams of known energy, with typical energy resolutions of about 0.002. One aspect of the design of the experiment already indicated in the above is the choice of He^4 as the accelerated particle rather than He^3 . This decision was made because of the tremendous background reduction achieved by accelerating the much more tightly bound alpha particle and in spite of the larger energy losses involved with the alpha-particle beam and the further reduction of the energy available in the center-of-mass system, ($3/7$ of the bombarding energy for He^4 as compared to $4/7$ for He^3).

The chemically inert nature of the He^3 target required the use of a gas target; the construction and design of this target are shown in Figures 2 and 3. This system was used for all the runs on the 3-MV and Tandem accelerators. The system on the 2-MV accelerator, although basically the same, was not as adequate in many ways such as the prevention of carbon build-up on surfaces struck by the beam. However, since the work on that accelerator served only as a

preliminary investigation, the details of that work will not be discussed here.

Beyond the image slits of the magnetic analyzers and just in front of the rest of the target assembly shown in Figure 2, on both the 3-MV and the Tandem accelerators was located an orthogonal slit system which could be used for preliminary beam definition or for further regulation of the accelerator voltage. Also located in that region was an oil diffusion pump with a liquid nitrogen trap and an ion gauge. During runs this vacuum was typically 10^{-6} mm or better and never worse than 2×10^{-6} mm.

The scale drawings of Figures 2 and 3 indicate in detail the construction of the target assembly beyond the slit system and the diffusion pump. The ion gauge in the body of the Circle-Seal valve typically indicated pressures of 4×10^{-6} mm or smaller during runs. The long cylindrical cold trap in the beam tube immediately down stream from the pump and slits and just in front of the ion gauge served to reduce the amount of organic material getting into the neighborhood of the target. All this concern about the problem of carbon build-up and contamination was necessitated by the serious background problems encountered from the neutrons produced by the reaction, $C^{13}(\alpha, n)O^{16}$. This was probably the most bothersome contamination reaction in this experiment, and consequently great effort was expended to reduce the amount of carbon present in the region of the target. This involved the trapping described above, the removal of all unnecessary O-rings, the substitution of glass for lucite wherever electrical insulation was

required and the use of special low-vapor-pressure waxes for the necessary glass-to-metal seals. It is clear from the work of Spear, Larson and Pearson (1962) that more drastic measures could have been employed to good advantage as far as improving the vacuum and reducing the carbon build-up are concerned. In any case the present set up was sufficiently effective to make this experiment feasible.

Beyond the trap and ion gauge described above, the next significant feature of the target assembly is the pair of beam-defining apertures. These were made of .010-inch tantalum, press fitted into their stainless steel retainer and then drilled to a .070-inch-diameter hole. These were used for the final beam definition, to prevent the beam from striking any part of the foil holder, the electron suppressor or any of the insulating material. The thin-walled stainless steel tubing immediately beyond the apertures served to isolate the wax glass-to-metal seals from the heat dissipated by these apertures. The pyrex glass tubing beyond this isolated the electron suppressor electrically from these apertures, while the second piece of pyrex tubing, on the other side of the suppressor, served as electrical insulation between the target and the suppressor. The suppressor itself was operated at a -300 volt d.c. potential and served to prevent secondary electrons from reaching the target from the beam-defining apertures.

The heart of the target assembly lies in the foil holder, the thin nickel entrance foil and the gas cell and associated gas-handling manifold. The entrance foil was soldered to the foil holder using

indium metal because its low melting point reduced the danger of damaging the nickel by splattering from the flux or by oxidation. For the high-energy runs, those with initial alpha-particle energies of 2 MeV and greater, 6,250- \AA nickel foils were used. However, at energies below 2 MeV we were forced to switch to 5,000- \AA nickel foils on which about 1000 \AA of copper was evaporated to improve the thermal conductivity of the foil. In this manner we were able to use beams of at least 0.4 μA over the entire range of energies. The nickel foils were obtained from Chromium Corporation of America, Waterbury, Connecticut.

The gas cell was made of stainless steel. The sides were .006 inches thick, and the back was .014 inches thick. The cell was then lined with an additional .003 inches of platinum to reduce background radiation. The depth of the cell was .530 inches which, allowing for the platinum liner and the .180-inch insertion of the foil holder, makes the effective length .347 inches. The size of this entire system was limited by the requirement of being able to use it inside the 5/8-inch-diameter well of one of the NaI(Tl) detectors.

A thin metal tube was soldered into the side of the gas cell, leading to the gas-handling system. The gas-handling system, shown schematically in Figure 4, was designed to permit the target gas to be changed quickly from He³ to He⁴ for measurement of the background counting rate. At pressures of 100 mm and lower the pressure was read directly on a closed-end mercury manometer. For higher pressures, the measurements were made on a bourdon gauge which was

later calibrated with a mercury manometer. Pressures used ranged from 100 mm at low energies to 494 mm at the higher energies where the energy loss in the target was not as severe and not as important.

The purity of the He^3 gas was taken as stated by the supplier, Mound Corporation, Miamisburg, Ohio. It varied from 99.13% to 99.33%.

The temperature of the gas cell (cooled by compressed air) was determined as approximately 30°C . Robertson, et al. (1961) point out that there may well also be a temperature differential within such a gas target caused by local heating by the incident beam so that the gas along the beam path, where the interaction is taking place, is actually substantially hotter than the target chamber. Such local heating should be proportional to the beam current (the rate of heat deposition) and therefore should lend itself to measurement as a function of beam current. In the present experiment, the effect was measured by looking at the leading edge of the 1.518-MeV resonance of the reaction

$\text{B}^{10}(\alpha, p)\text{C}^{13}$ using a thick B^{10} target at the back of the target chamber with a target of He^4 at a pressure of 368 mm. The beam current was varied from $0.5 \mu\text{A}$ to $0.1 \mu\text{A}$, and the energy shift of the leading edge of the resonance measured. Linear extrapolation to room temperature at zero beam current leads to an effective temperature of 345°K for a beam current of $0.45 \mu\text{A}$, the typical current used in this experiment.

A simple calculation on the basis of heat transport by conductivity by the helium gas, however, allows a temperature differential of only 5°C between the beam path and the target-chamber walls. The only way to understand the size of the observed effect, then, seems to be in terms of intense local heating at the entrance foil and to a smaller extent at

the beam stopper. Indeed, a similar calculation on the basis of the conductivity of the entrance foil, yields a temperature differential of 75°C between the beam spot and the brass foil holder. From the above information regarding the length, temperature and pressure of the target it is possible to determine directly the number of target nuclei present per cm^2 along the beam path, typically 10^{+19} cm^{-2} .

The charge of the incident beam was collected in the gas target which was connected to a current integrator arranged to stop the various scalers and multi-channel pulse-height analyzers after the accumulation of a particular amount of charge, i.e. a particular number of incident alpha particles. The entrance foil was included in the collection system, and therefore any corrections for the effective charge of the incident alpha particles were made unnecessary. The target was operated at a +300 volt d.c. potential to prevent secondary emission. For runs on the Tandem accelerator the charge collection of the beam integrator was calibrated using a measured, constant current and noting the time required for that current to fire the integrator. For runs on the 3-MV accelerator the firing voltage was measured on a meter, and the value of the capacitance was taken as $9.45 \pm .02 \mu\text{f}$ as determined independently by Kavanagh and Brown by charging the capacitor to a known voltage and then measuring the current and time required to discharge it through a 600 volt battery in series with a high resistance, $\sim 500 \text{ M}\Omega$ (Brown, 1962). Such calibrations, except for the determination of the capacitance, were made at the beginning and end of each running day. From this information the number of incident

particles can be determined. For these runs the total charge accumulated at each point was of the order of 2500 μ C, $1.56 \times 10^{+16}$ incident alpha particles, for the He^3 target and an equal amount for the He^4 target.

B. Detection System.

Having discussed the determination of the number of target nuclei and the number of incident, bombarding nuclei, we must now concern ourselves with the detection and measurement of their interaction. The interaction under study involves the emission of prompt gamma radiation. NaI(Tl) scintillators were used to detect this radiation. (The residual nucleus, Be^7 , being radioactive, the experiment could have been run by counting the 478-keV gamma rays involved in 12% of the decays. However, the 53-day half-life of Be^7 and the fact that such a measurement would yield no information about the branching ratio and angular distributions involved make this a much less desirable way to proceed than detecting the prompt capture radiation.) The scintillators were optically coupled to photomultiplier tubes, and the signals from these fed through the usual electronic circuitry to be stored in a multi-channel pulse-height analyzer. This analyzer was gated by a relay in the current integrator so that the stored pulses corresponded to interactions associated with a certain number of incident alpha particles. Since the multi-channel analyzer requires a certain finite amount of time for the analysis of each pulse, during which it will not accept additional pulses, there is associated with its operation a certain amount of dead time. Corrections were made for

this by recording for each integration the actual clock-time of the run and the live-time of the analyzer and then multiplying the stored spectrum by the ratio of the clock-time to the live-time. This correction was always small, the ratio being 1.00 for more than 80% of the runs and always less than 1.17.

Three sizes of crystals were used in the experiment, a 2" \times 2" solid cylindrical crystal, a 3" \times 3" solid cylindrical crystal and a 3" \times 3" cylindrical crystal with a 3/4"-diameter by 2"-deep well along its axis. These were all obtained from The Harshaw Chemical Company, Cleveland, Ohio, and were of their Integral Line type. The geometries in which these were used are shown in Figure 5. The total efficiency (η_0) of each of these was calculated for the geometries involved in the experiment, for both isotropic and $\sin^2\theta$ radiation patterns and for the range of gamma-ray energies from 0.400 MeV to 8.00 MeV. For the details of these calculations see Appendix I.

Such calculations assume a "free" crystal, one with no shielding and removed from all sources of scattering. This situation can not be utilized in most experiments because of the necessary presence of much heavy shielding used to reduce the amount of background radiation interacting with the crystal. (In the present experiment the scintillators were heavily shielded using approximately half a ton of lead, a minimum of 4 inches in all directions and 6 inches in the direction of the accelerator, defining slits, etc. and in front of the crystal on the opposite side of the target.) One way to convert these idealized calculations, so that they can be used in practical situations, is to limit our

interest to the full-energy peak of the gamma-ray spectrum. (See Appendix I for a discussion of gamma-ray spectra and their characteristic features.) Only those quanta whose interactions with the scintillator leave their entire energy in the crystal can contribute counts to the full-energy peak. Consequently the number of full-energy-peak counts is independent of the presence of shielding or other scattering material, and this number can be used as a quantitative measure of the intensity of the gamma radiation. By measuring the ratio (ϕ_o) of the number of full-energy counts to the total number of counts in a "free" crystal, the number of full-energy counts in any situation can be related to the total efficiency, and hence the number of full-energy counts can then be used to measure the absolute intensity of the gamma radiation. This photo-fraction (ϕ_o) was measured in this experiment for the 2" \times 2" crystal at a gamma-ray energy of 432 keV, and for the other two crystals over the energy range from 432 keV to 4.433 MeV. For the details of these measurements see Appendix I.

Furthermore, if one is to be able to measure the absolute intensity at the source, i.e. the absolute number of interactions, corrections must also be made for the absorption by materials between the source and the crystal, such as the housing of the crystal and the walls of the target chamber. Such calculations were also made and are also described in detail in Appendix I. Suffice it to say here that each of the crystals used in this experiment was calibrated so that from the number of counts in the full-energy peak of the spectrum the absolute number of interactions in the target could be determined.

C. Energy Determination.

From the above information it is possible to determine the absolute cross section for the reaction under investigation. Now, however, since such a cross section can be expected to vary with the center-of-mass energy involved, we must determine the energy at which we have measured the cross section. Because we are using a gas target in which the incident beam must pass through an entrance foil before interacting with the target nuclei, determining the energy at which the interaction takes place is not just a simple matter of calibrating the 90° analyzing magnet. There are two ways to get around this difficulty in the present experiment, both of which were utilized. The first of these is the obvious one of actually measuring the energy loss in the entrance foil by observing the energy shift of a resonance resulting from placing the foil in front of a suitable target. In the present experiment the thickness of the foil was measured utilizing the narrow resonance in the reaction, $B^{10}(\alpha, p)C^{13}$, at an alpha-particle energy of 1.518 MeV. (The measured thicknesses of these foils were always within the manufacturer's quoted tolerance of $\pm 20\%$ of the nominal value.) Once the foil thickness is known at one energy, the energy loss in the foil can be calculated at any other energy by making use of the proton stopping-cross-section curves of Whaling (1958). A conversion of these proton stopping-cross-section curves to alpha particles, by the relation

$$\epsilon_\alpha = \overline{(z_\alpha^2)} \epsilon_p (E_\alpha / 3.97)$$

is shown in Figure 17, where $\overline{(z_\alpha^2)}$ is the effective squared charge

as also given by Whaling (1958). This, coupled with a further correction for the energy losses in the gas target and a knowledge of the initial beam energy (E_0), allows one to determine the beam energy at the center of the target (E_α) as

$$E_\alpha = E_0 - \epsilon_\alpha (\text{Ni}) n t_{\text{foil}} - \frac{1}{2} \epsilon_\alpha (\text{He}) n t_{\text{gas target}}$$

$$E_{\text{cm}} = \frac{3}{7} E_\alpha.$$

The second and more direct method of determining the center-of-mass energy at which the interaction took place is made possible by the nature of the direct-capture process, the fact that the energy of the resultant gamma ray (E_γ) depends on the center-of-mass energy (E_{cm}) at which the interaction took place:

$$E_\gamma = E_{\text{cm}} + Q$$

Hence, a measurement of the gamma-ray energy tells one directly the value of E_{cm} . This more straightforward method was used for all but a very few of the runs where the gamma-ray intensity was so low that the gamma-ray energy could not be accurately determined from the spectra. In these latter cases, and in a few others to check the agreement of the two methods, the first method was used. The comparison of the two methods was in all cases within the experimental errors.

The cases utilizing the first method were all run on the 3-MV accelerator, and for that purpose the 90° analyzing magnet on that machine was accurately calibrated by examining the 992.0-keV

resonance in Al²⁷(p,γ) and the 1843.1-keV resonance in Ni⁵⁸(p,γ). Making allowance for the + 300-volt target potential, the magnet constant for singly-charged alpha particles (k_α) was determined to be

$$k_\alpha = 0.085295 \pm 0.00005 \text{ MeV volts}^2$$

where

$$E_\alpha = \frac{k_\alpha}{E_{MA}^2}$$

and where E_{MA} is proportional to the flux-meter current.

To make use of the second method it is necessary to be able to determine accurately the energy of the resultant gamma ray. Such a determination is made possible by the fact that the NaI(Tl) detectors are proportional counters for gamma rays; their output pulse-height is proportional to the energy lost in the crystal. Hence, the position of the full-energy peak in the multi-channel analyzer spectrum will be proportional to the gamma-ray energy, and once the analyzer's response has been calibrated this position can be used to determine the gamma-ray energy. Such a calibration was carried out at the beginning and end of each day of running, by measuring the positions of the full-energy peaks of the following six gamma rays:

511 keV	annihilation radiation (Na ²²)
570 keV	Bi ²⁰⁷
1064 keV	Bi ²⁰⁷
1277 keV	Na ²²
1768 keV	Bi ²⁰⁷
2614 keV	Tl ²⁰⁸

There is, however, one problem associated with this way of determining E_{cm} . This arises from the fact that in a direct-capture reaction the residual nucleus always recoils directly forward, giving rise to a Doppler shift in the gamma-ray energy dependent on the angle at which the gamma ray is emitted by the forward-recoiling nucleus.

The correction for this may be calculated as follows:

$$E_\gamma(\theta) = E_\gamma \frac{\sqrt{1 - \beta^2}}{1 - \beta \cos \theta}$$

where θ is the angle at which the gamma ray is emitted relative to the direction of the recoiling nucleus, which is traveling with a velocity, βc . Since the maximum value of β for the recoils encountered in this experiment is approximately 0.03, second order effects can be neglected, and we can write

$$E_\gamma(\theta) \approx E_\gamma / (1 - \beta \cos \theta)$$

In this experiment, runs were made in three different geometries, with the solid 3" \times 3" crystal at 90° and at 0° to the incident beam and with the 3" \times 3" well crystal aligned along the beam axis with the target at the center of the crystal. (See Figure 5.) From the above equation it is then clear that

$$\text{at } 90^\circ \quad E_\gamma = E_\gamma(90^\circ), \quad \text{and}$$

$$\text{at } 0^\circ \quad E_\gamma = E_\gamma(0^\circ) \times (1 - \beta)$$

The determination of β , however, is somewhat circular since it involves a knowledge of the center-of-mass energy (E_{cm}) or the incident alpha-

particle energy (E_α) which in turn are determined by knowing the gamma-ray energy. However, we can write

$$E_\gamma = Q + \frac{3}{7} E_\alpha \quad Q = 1.587 \text{ MeV}$$

$$= Q + E_{cm}$$

and from conservation of momentum

$$\beta(Be^7) = \frac{4}{7} \beta(\alpha)$$

$$E_\gamma(0^\circ) \cdot (1 - \beta(Be^7)) = Q + \frac{3}{7} E_\alpha$$

$$= Q + \frac{3}{7} (\frac{1}{2} M_\alpha c^2 \beta^2(\alpha))$$

$$= Q + \frac{3}{14} M_\alpha c^2 (\frac{7}{4})^2 \beta^2(Be^7)$$

$$E_\gamma(0^\circ) - E_\gamma(0^\circ) \beta = Q + \frac{21}{32} M_\alpha c^2 \beta^2$$

$$\left[\frac{21}{32} M_\alpha c^2 \right] \beta^2 + \left[E_\gamma(0^\circ) \right] \beta + (Q - E_\gamma(0^\circ)) = 0$$

Therefore,

$$\beta = \frac{-E_\gamma(0^\circ) + \sqrt{E_\gamma^2(0^\circ) + \frac{21}{8} M_\alpha c^2 (E_\gamma(0^\circ) - Q)}}{\frac{21}{16} M_\alpha c^2}$$

where the second solution of β is neglected since it gives rise to negative values for β which are physically meaningless. From this evaluation of β the true gamma-ray energy (E_γ) can now be determined from $E_\gamma(0^\circ)$. A plot of the calculated Doppler shift, $(E_\gamma(0^\circ) - E_\gamma)$, as a function of E_γ is shown in Figure 18. A direct determination of this shift was possible

in a few cases where both 0° and 90° runs were made using the same entrance foil. These determinations are also plotted in Figure 18 for comparison with the calculated shift. They indicate that the shift was actually about 10 keV smaller than calculated. This is easily understood in terms of the large solid angle subtended by the NaI(Tl) crystal at 0° . The calculated shift is the maximum shift, occurring only for gamma rays at 0° , whereas the detector received considerable numbers of counts in its full-energy peak from quanta emitted at angles of 30° and larger. Such a correction to the calculated shift is not necessary at 90° because although the same solid angle is subtended by the scintillator, quanta with $\theta > 90^\circ$ have their energy lowered by the shift whereas quanta with $\theta < 90^\circ$ have their energy raised, so that the net effect at 90° is a Doppler spread in the full-energy peak and not a correction to the calculated shift.

For the well crystal the observed gamma-ray energy was assumed to be the true gamma-ray energy, although it was actually probably somewhat greater since there was a little more detector in front of 90° than behind 90° . In this case, however, the large solid angle subtended, nearly 4π , gave rise to a large Doppler spread in the full-energy peak, nearly twice the calculated Doppler shift at 0° .

D. Coincidence Measurement.

Before summarizing and concluding this chapter, we should consider one more aspect of the experiment, the use of a coincidence technique to obtain an independent measurement of the cross section for the cascade transition, as a check on the unfolding procedures

described in the next chapter. For this measurement a $3'' \times 3''$ and $2'' \times 2''$ NaI(Tl) were placed on opposite sides of the target chamber, as indicated in Figure 5, and the coincidences between a γ_3 event in the $2'' \times 2''$ and a γ_2 event in the $3'' \times 3''$ were counted. (See Figure 1.)

The output of the $2'' \times 2''$ NaI(Tl) was fed into the multi-channel analyzer which was gated by a triple-coincidence circuit with a measured resolving time of 50×10^{-9} seconds. This mixer required a "slow" coincidence between (1) the output of the $3'' \times 3''$ in the region of the full-energy peak of γ_2 , (2) the output of the $2'' \times 2''$ in the region of the full-energy peak of γ_3 , and (3) the output of another mixer requiring a "fast" coincidence between the output of the $3'' \times 3''$ and the output of the $2'' \times 2''$. A detailed description of this circuit has been presented by Pearson (1963).

E. Conclusion.

As a conclusion to this discussion of the experimental apparatus and procedure, it might be helpful to summarize briefly the steps involved in a typical run. First the multi-channel analyzer's response was calibrated with respect to gamma-ray energy, and the current integrator was calibrated to determine how much collected charge was necessary to fire the relays which terminated the data accumulation. Then the detector geometry was arranged and measured. An alpha-particle beam of the desired energy and intensity was then focused on the target. Beam intensities were normally in the neighborhood of 0.45 μ A, an upper limit being established by the ability of the entrance foil to withstand the heating due to the beam and a lower limit by the

time required and the competition of time-dependent background. Runs for a definite number of incident alpha particles, as determined by the current integrator, were then taken starting with He^4 as a target gas and then alternating with runs on He^3 gas. The runs on He^4 were used as background runs to be subtracted from the runs on He^3 to obtain the net $\text{He}^3(\alpha, \gamma)\text{Be}^7$ yield. Gases were normally switched every two integrations, ending with a run on He^4 so that the background radiation was monitored across the entire series of runs. Runs were approximately 500 μC each and as many as ten such runs on each gas were taken in a series at a given energy, although typically the number of integrations on each gas was four or six, depending on the yield at that particular energy. The runs were checked as they progressed by using two scalers as a single-channel analyzer covering the region of the gamma-ray full-energy peaks. In this way any change in yield due to the build-up of carbon or other variation in the background could be monitored and corrective measures taken.

At the low bombarding energies ($E_\alpha \leq 2.00$ MeV) the yield from the reaction becomes small enough so that the time-dependent background began to become important. Due to slight variations in the beam intensity during a series of runs, it was quite possible that there would be a significant difference in the total time represented by the He^3 runs and that of the He^4 runs. Consequently at energies where the time-dependent background was important, total time corrections were made using spectra taken for definite lengths of time with the accelerator in operation but with the beam switched off the target. Finally after all these

runs were made the integrator calibration was checked, the multi-channel analyzer calibration was checked, and the geometry of the detector was checked.

The detailed analysis of the spectra resulting from such a series of runs is discussed in the next section.

IV. DATA ANALYSIS

A. Conversion of Gamma-Ray Spectra to Absolute Cross Sections

Having described in detail in the preceding chapter how the number of target nuclei, the number of incident nuclei and the energy of interaction were all determined, it is necessary to go into more detail here to describe how the resulting gamma-ray spectra were handled to determine the number of interactions that occurred.

The first step was to check the reliability of the series of runs at a particular energy to see if a reasonably accurate background subtraction could be performed. This testing was done first by checking the runs using a single-channel analyzer, as described in the previous chapter, and second by comparing the individual spectra from such a series of runs. This latter phase consisted of checking that those runs on He^4 all matched each other reasonably well and similarly for the He^3 runs, and that all the spectra matched in the high-energy region beyond the structure of the gamma rays from $\text{He}^3(\alpha, \gamma)\text{Be}^7$. These requirements could not always be satisfied, but it was possible to accept, in addition, those cases where there was only a small, but smooth variation in the spectra, since the method of alternating the target gas throughout the series of runs compensated for such an effect. Once a set of runs at a particular energy had been found acceptable as described above, the Burroughs' 220 computer was used to reduce the spectra by (1) applying dead-time corrections to the individual spectra, (2) combining all He^3 runs and all He^4 runs, (3) applying any necessary total-time corrections and (4) then subtracting the total He^4 runs from the total He^3 runs to

yield the net $\text{He}^3(a, \gamma)\text{Be}^7$ gamma-ray spectrum. (See Figure 19.)

Having thus reduced the data to yield the spectrum of the gamma radiation due only to the $\text{He}^3(a, \gamma)\text{Be}^7$ reaction, the direction in which further analysis proceeded depended on the set of runs involved, since slightly different conditions involved in various runs invalidated the application of certain of the methods of analysis. To understand better the specific problems involved, it is perhaps best to elaborate briefly at this point on the nature and energy of the gamma rays involved in this experiment. From Figure 1, it is apparent that a direct-capture event in the energy range, $0.0 \leq E_a \leq 6.0$ MeV, can produce two specific gamma-ray events:

(1) The ground-state transition with only one gamma ray,

$$(\gamma_1). E_{\gamma_1} = (1.587 + \frac{3}{7} E_a) \text{ MeV}.$$

(2) The cascade transition with one gamma ray, (γ_2) ,

followed by a second gamma ray, (γ_3) .

$$E_{\gamma_2} = (1.155 + \frac{3}{7} E_a) \text{ MeV}, \text{ and}$$

$$E_{\gamma_3} = 0.432 \text{ MeV}.$$

Since the spin of the 432-keV state is known to be $1/2$, the angular correlation between γ_2 and γ_3 will be isotropic. Further, since the energy difference between γ_1 and γ_2 is 432 keV, the full-energy peak of γ_2 will lie only 79 keV above the single-escape peak of γ_1 , and the two will not be resolvable. (See Appendix I.) The same argument applies to the single-escape peak of γ_2 and the double-escape peak of γ_1 . It should be noted that there will also be a peak, coincident with the full-energy peak of γ_1 , due to the summing of γ_2 and γ_3 in the NaI(Tl)

detector. Because of the low energy of γ_3 its full-energy peak was always well down in the noise, and, since the fitting procedures were never extended to such low energies, this peak was neglected in all the analysis except for the coincidence data where its use is discussed explicitly.

The first method of analysis is a procedure directly suggested by Salmon (1961), although worked on by numerous other authors, (Childers, 1959; Mollenauer, 1961; West, 1960; and Heath, 1962). This involves the use of gamma-ray shape fitting to unfold complex combinations of gamma-ray spectra using electronic computers. To accomplish this the NaI(Tl) crystals involved were first calibrated with regard to their shape responses to monoenergetic gamma rays of various energies. See Appendix I for the details of this calibration. These shape-response functions were then stored in the Burroughs' 220 computer, and, given a gamma-ray energy in the range $1.277 \leq E_{\gamma} \leq 4.433$ MeV (the range of calibration), the computer was programmed to interpolate the appropriate response function. In the present experiment, E_{γ_1} was determined either from an examination of the individual spectra from each run and the calibration of the multi-channel analyzer, or from a knowledge of the beam energy, the foil thickness, the target thickness and the Q-value of the reaction,

$$E_{\gamma_1} = Q + \frac{3}{7}(E_o - \Delta E_{\text{foil}} - \frac{1}{2}\Delta E_{\text{gas}})$$

as described in the previous chapter. E_{γ_2} was taken as

$$E_{\gamma_2} = E_{\gamma_1} - 0.432 \text{ MeV}$$

The computer first determined the response function for γ_1 and then the response function for γ_2 . Next the response function of the crystal for the summation of γ_2 and γ_3 was determined by folding together the response function of γ_2 and that of γ_3 , stored in the computer separately. The details of this folding procedure are discussed in Appendix I.

Having now separately obtained the response functions for γ_2 (1) when there is no summing with γ_3 and (2) when there is summing with γ_3 , we would now like to combine the two into a total response function for γ_2 . The amount of summing in such a total response function is determined by the efficiency of the scintillator for detecting γ_3 . Considering the number of counts in the full-energy peak of each response function, we can say first that for N cascade transitions in the target there will be $\{\eta(2)\phi_o(2)\eta(3)\phi_o(3)N\}$ counts in the full-energy peak of the summing response function, (where $\eta(i)$ is the probability of γ_i interacting with the crystal at all and $\phi_o(i)$ is the fraction of such interacting photons which contribute counts to the full-energy peak) since the probability of such an interaction is the product of the probabilities of both γ_2 and γ_3 depositing all their energy in the scintillator. Similarly we can say that under the same circumstances there will be $\{\eta(2)\phi_o(2)[1-\eta(3)]N\}$ counts in the full energy peak of the γ_2 response function. The ratio of full-energy counts in the summing response function to the full-energy counts in the γ_2 response function is thus $\eta(3)\phi_o(3)/(1-\eta(3))$. Therefore, the summing response function was re-normalized to agree with the above ratio, and then the two response

functions were combined to form the desired total cascade response function.

The ground-state response function and the cascade response function were then combined to give a least-squares fit to the net $\text{He}^3(a, \gamma)\text{Be}^7$ spectrum, utilizing all the available points or channels. (See Figure 20.) At each of the "n" points (n typically the order of 80 or 100) we may write the following:

$$C_i = A_i X + B_i Y + Z_i$$

where

C_i = the number of counts in channel i of the net $\text{He}^3(a, \gamma)\text{Be}^7$ spectrum,

A_i = the number of counts in channel i of the ground-state response function,

B_i = the number of counts in channel i of the cascade response function,

Z_i = a random error,

and where the best values of X and Y are obtained by the least-squares requirement of minimizing the following function, R , with respect to both X and Y .

$$R \equiv \sum_{i=1}^n (C_i - A_i X - B_i Y)^2$$

$$\frac{\partial R}{\partial X} \equiv 0 \rightarrow \sum_i (C_i - A_i X - B_i Y) A_i = 0$$

$$\frac{\partial R}{\partial Y} \equiv 0 \rightarrow \sum_i (C_i - A_i X - B_i Y) B_i = 0$$

Therefore,

$$X \sum_i A_i^2 + Y \sum_i A_i B_i = \sum_i A_i C_i$$

$$X \sum_i A_i B_i + Y \sum_i B_i^2 = \sum_i B_i C_i$$

Defining α , β , η , λ and ξ so that

$$\alpha X + \beta Y = \lambda$$

$$\beta X + \eta Y = \xi$$

we see that

$$X = \frac{(\lambda\eta - \beta\xi)}{(\alpha\eta - \beta^2)} \pm \left[\frac{R}{n-2} \frac{\eta}{(\alpha\eta - \beta^2)} \right]^{1/2}$$

$$Y = \frac{(\alpha\xi - \beta\lambda)}{(\alpha\eta - \beta^2)} \pm \left[\frac{R}{n-2} \frac{\alpha}{(\alpha\eta - \beta^2)} \right]^{1/2}$$

This method of fitting experimental gamma-ray spectra has an advantage over the more traditional graphical approach, where successive full-energy peaks are fitted in order of decreasing energy, since the least-squares method uses all the response functions at each point and thus does not accumulate error in the low energy direction. Furthermore, in this particular case where the full-energy peaks of both response functions are coincident and the secondary peaks of one are not resolvable from those of the other, the successive graphical peak-fitting method could only have been employed utilizing some sort of iterative procedure.

Having obtained a least-squares fit to the experimental spectrum, from the number of full-energy counts in each of the fitted response functions, $[XA_i]$ and $[YB_i]$, and a knowledge of the photo-fractions and total efficiencies for γ_1 , γ_2 and γ_3 , as determined in Appendix I, it is then possible to determine independently the number of ground-state events and the number of cascade events. From this, coupled with our measurements of the number of target nuclei (N_t) and the number of incident alpha particles (N_a), we can determine $\sigma(\gamma_1)$ and $\sigma(\gamma_2)$ independently and thus also determine σ_{Total} and the branching ratio, ρ .

$$\sigma(\gamma_1) = \frac{Y_\phi(\gamma_1)}{N_a N_t \eta(\gamma_1) \phi_o(\gamma_1)}$$

$$\sigma(\gamma_2) = \frac{Y_\phi(\gamma_2 + \gamma_3)}{N_a N_t \eta(\gamma_2) \eta(\gamma_3) \phi_o(\gamma_2) \phi_o(\gamma_3)}$$

$$\sigma_{\text{Total}} = \sigma(\gamma_1) + \sigma(\gamma_2)$$

$$\rho = \sigma(\gamma_2)/\sigma(\gamma_1)$$

where $Y_\phi(\gamma_i)$ is the number of counts in the full-energy peak of the least-squares fitted response function of γ_i .

The decision as to the presentation of the data in terms of σ_{Total} and ρ , instead of $\sigma(\gamma_1)$ and $\sigma(\gamma_2)$, was made on the basis of the following considerations. For reasons explained below, about half of the data could not be analyzed as described above, and the alternate methods of analysis did not allow the independent determination of $\sigma(\gamma_1)$ and $\sigma(\gamma_2)$. In such cases, a value of the branching ratio was assumed in line with

measurements obtained above and a corresponding value obtained for σ_{Total} . Values for $\sigma(\gamma_1)$ and $\sigma(\gamma_2)$ obtained from these methods of analysis would not have been independent, and their presentation as such would have been misleading. This, coupled with the fact that σ_{Total} is much less sensitive to errors in ρ than either $\sigma(\gamma_1)$ or $\sigma(\gamma_2)$, makes σ_{Total} a much more meaningful value to present in such cases.

The cases where the least-squares method of analysis was not applicable can be separated into the following three distinct categories:

- (1) cases where the net experimental spectrum had too few counts to do any detailed shape fitting,
- (2) cases where problems of background variation prevented accurate subtraction and thus prevented the attainment of a good fit, and
- (3) cases where the use of absorbers between the scintillator and the target, to reduce the intensity of low-energy X-rays and gamma rays, invalidated the use of the response functions obtained in the absence of such absorbers.

It is true that in the last case response functions could have been obtained with each of the absorbers used, but this was deemed unnecessarily tedious. Case (2) is certainly a highly subjective condition, and it should be added here that the existence of such a poor fit was determined primarily on the basis of how the total number of counts in the full-energy peak of the net experimental spectrum compared to the sum of the counts in the full-energy peaks of the two fitted response functions. Case (1) applies to data taken at the low energy end of the region covered in this

experiment, where the total cross section has fallen to much less than a microbarn.

To analyze the data which fell in the above three categories, two methods were available. The simpler of these involves an analysis of only the peak corresponding to the full-energy peak of γ_1 and the full-energy peak of the sum spectrum of γ_2 and γ_3 . It is thus clear that such a method can not yield information about ρ , and to obtain any value for σ_{Total} one must assume a value for ρ . For such an analysis the total capture cross section, σ_{Total} , can be expressed directly in terms of the number of counts (N_ϕ) in the peak in question, the branching ratio assumed (ρ), and the various efficiencies of the detector.

$$\sigma_{\text{Total}} = \frac{N_\phi}{N_a N_t} \frac{(1 + \rho)}{\eta(\gamma_1)\phi_o(\gamma_1) + \rho\eta(\gamma_2)\phi_o(\gamma_2)\eta(\gamma_3)\phi_o(\gamma_3)}$$

The second method of analysis for the three cases noted above involves what might be described as an integral approach. It involves an analysis of the entire available spectrum and consequently is not well suited to handling cases (2) and (3) but is instead designed for use with case (1) where poor statistics have invalidated a point-by-point fitting of the experimental spectrum, and where, instead, we now will use a fit of the integrated spectrum, covering a large number of points. For this method of analysis, once the net experimental spectrum has been obtained, the various response functions are obtained and combined to form the cascade and ground-state response functions as before. At this point, because of the poor statistics involved, the ground-state and

cascade response functions are further combined under the assumption of a particular value of ρ to form the total response function. The number of counts (Σ) in a given region of the spectrum (excluding the low-energy region near the full-energy peak of γ_3) is then divided by Φ , the ratio of the counts in the same region of the total response function to the total number of counts in the total response function (excluding, as always, the contributions due to single γ_3 interactions).

In this way the total capture cross section is obtained as

$$\sigma_{\text{Total}} = \frac{\Sigma}{\Phi N_a N_t} \frac{1 + \rho}{(\eta(\gamma_1) + \rho \eta(\gamma_2))}$$

An upper limit for the region to be analyzed was established at $(E_{\gamma_1} + 600 \text{ keV})$, and the lower limit was varied to include various fractions of the spectrum. As the lower limit of this region is moved to lower and lower energies and the statistics improve, one would ideally expect the value of $\frac{\Sigma}{\Phi}$ to approach a constant. How good a value of $\frac{\Sigma}{\Phi}$ had been obtained was determined by plotting this quantity as a function of the lower limit of the region under analysis and looking for the expected asymptotic approach to a constant value. In all four of the cases analyzed in this manner this was found to be true, the variation of $\frac{\Sigma}{\Phi}$ about such a value always becoming less than 4%.

It is clear that both of the secondary methods of analysis could also be applied to the runs which could be analyzed by the primary method of detailed fitting. Such a comparison of the primary and secondary methods was carried out and in general indicated good agreement between the three methods, deviations typically falling in the range from 0% to 3%.

Before leaving this discussion of the methods used to obtain σ_{Total} and ρ by an analysis of the net experimental gamma-ray spectrum, mention should be made of the analysis of the coincidence data obtained to check on the values of ρ derived from the method of least-squares fitting. Such a check was made by measuring the cascade cross section $\sigma(\gamma_2)$ independently of the ground-state cross section by looking only at coincidences between the γ_2 and γ_3 members of such a cascade using the techniques described in the preceding chapter. The net experimental gamma-ray spectrum thus obtained, after the usual background subtraction, in this case represents the spectrum of gamma radiation in the 2" x 2" NaI(Tl) in the region of 432 keV in coincidence with events in the neighborhood of the full-energy peak of γ_2 in the 3" x 3" NaI(Tl) crystal. However, this region of the gamma-ray spectrum of the 3" x 3" crystal contains a good deal more than events due to a γ_2 interacting with the crystal. Many of these events either can not give rise to a coincident pulse in the 2" x 2" crystal or will be removed by the usual process of background subtraction. However, there are two notable and important cases in which coincident counts not due to γ_3 will occur in the second detector which can not be removed by the usual subtraction of background. These are events due to a γ_1 or a γ_2 interacting with the 3" x 3" crystal in a Compton or pair-production event in which one of the secondary quanta escape and interact with the 2" x 2" detector. This is possible since that portion of the 3" x 3" spectrum considered contains (1) that portion of the γ_1 and γ_2 spectra corresponding to Compton events in which the low energy "backscattered" quanta escape from this crystal, (2) that portion of the γ_1 spectrum corresponding to

pair-production events in which either one or two of the annihilation quanta escape from the crystal and (3) that portion of the γ_2 spectrum corresponding to pair-production events in which one of the annihilation quanta escape from the crystal. One would then expect to find in the $2'' \times 2''$ coincident spectrum, in addition to the peak at 432 keV due to γ_3 , peaks at 511 keV due to annihilation radiation and at roughly 230 keV due to backscattered quanta from γ_1 and γ_2 (2.965 and 2.533 MeV respectively for the case under consideration). Indeed, all three of these peaks are observed in the spectrum. The backscattered peak is of low enough energy compared to E_{γ_3} so that it can easily be corrected for by essentially ignoring it and dealing with only the full-energy peak of γ_3 . Correction for the annihilation radiation is slightly more difficult and involves the fitting of the 511-keV peak to the experimentally determined response function of the $2'' \times 2''$ crystal for 511-keV radiation and subtracting this contribution. In this way the number of coincident counts in the full-energy peak of γ_3 , $(Y_{\phi_c}(\gamma_3))$, was determined. Further, it was necessary to determine what fraction (x_2) of the γ_2 response function is included in the gating window of the $3'' \times 3''$ detector. This was done by determining the response function for γ_2 , using the computer program described above, and then measuring x_2 with a planimeter ($x_2 = 0.483 \pm 0.02$). The cascade cross section can now be expressed in terms of these measurements as

$$\sigma(\gamma_2) = \frac{Y_{\phi_c}(\gamma_3)}{N_a N_t} \frac{1}{x_2 \eta(\gamma_2) \eta(\gamma_3) \phi_o(\gamma_3)}$$

B. Error Analysis

Before discussing the results of the experiment we should discuss here the errors involved in the measurements described above so as to make the results and their associated errors more meaningful. Margenau and Murphy (1956) give the expression for the probable error of a function as follows:

for $Z = f(x, y, \dots)$

$$P_z^2 = P_x^2 \left(\frac{\partial f}{\partial x} \right)^2 + P_y^2 \left(\frac{\partial f}{\partial y} \right)^2 + \dots$$

where P_a is the probable error of the quantity "a".

On the basis of this, for the various quantities measured and calculated in this experiment we can calculate the following probable errors.

1. E_{cm}

In the case of our determination of the center-of-mass energy at which a particular measurement was made there are two types of errors to produce an uncertainty in our determination. First, there is simply the inaccuracy of our determination; this was approximately ± 10 keV both in the cases where E_{cm} was determined from an examination of the position of the full-energy peak of γ_1 and in the cases where E_{cm} was found from a measurement of the thickness of the entrance foil. Second, a lack of definition in E_{cm} was introduced by the spread in energy of our supposedly monoenergetic beam. This spread was caused by straggling in the entrance foil and by the thickness of the gas

target. In the case of foil-straggling the effect was measured by observing the width of the 1.518 MeV-resonance in $B^{10}(a, p)C^{13}$ with and without entrance foils in front of the target. The straggling was found to be approximately 60 keV (in the lab system) at this energy, and, since the theory of straggling by Bohr (1915) predicts that straggling should be independent of the energy of the incident particle, this figure was assumed to hold over the whole range of alpha particle energies used in this experiment. Any error in this assumption is probably not too serious since at high energies, where such an error would occur, straggling amounts to only about 12% of the total error in E_{cm} . In the case of beam width induced by the thickness of the target, the spread can be calculated simply from the energy of the beam in the target and the number of atoms per cm^2 in the target; the spread is just equal to the mean energy loss of the beam from the front to the back of the target.

Thus the probable error of the center-of-mass energy is

$$(\delta E_{cm})^2 = \left(\frac{3}{7} \cdot \frac{1}{2} \Delta E_{gas}(\text{lab})\right)^2 + \left(\frac{3}{7} \cdot 30 \text{ keV}\right)^2 + (10 \text{ keV})^2.$$

2. ρ

For the cases where a least-squares fit was possible we have shown above that the branching ratio (ρ) is given by

$$\begin{aligned} \rho &= \sigma(\gamma_2)/\sigma(\gamma_1) \\ &= \frac{Y_\phi(\gamma_2 + \gamma_3)}{N_a N_t \eta(\gamma_2) \phi_o(\gamma_2) \eta(\gamma_3) \phi_o(\gamma_3)} / \frac{Y_\phi(\gamma_1)}{N_a N_T \eta(\gamma_1) \phi_o(\gamma_1)} \\ &= \frac{Y_\phi(\gamma_1 + \gamma_3) \eta(\gamma_1) \phi_o(\gamma_1)}{Y_\phi(\gamma_1) \eta(\gamma_2) \phi_o(\gamma_2) \eta(\gamma_3) \phi_o(\gamma_3)}. \end{aligned}$$

Therefore,

$$\left(\frac{\Delta \rho}{\rho}\right)^2 = \left(\frac{\Delta Y_\phi(2+3)}{Y_\phi(2+3)}\right)^2 + \left(\frac{\Delta Y_\phi(1)}{Y_\phi(1)}\right)^2 + \left(\frac{\Delta \eta(1)}{\eta(1)}\right)^2 + \left(\frac{\Delta \phi_o(1)}{\phi_o(1)}\right)^2 + \left(\frac{\Delta \eta(2)}{\eta(2)}\right)^2 \\ + \left(\frac{\Delta \phi_o(2)}{\phi_o(2)}\right)^2 + \left(\frac{\Delta \eta(3)}{\eta(3)}\right)^2 + \left(\frac{\Delta \phi_o(3)}{\phi_o(3)}\right)^2.$$

Errors in the efficiency, η , are contributed from two sources, the accuracy of the calculation and the accuracy with which the source-detector geometry could be determined. The first of these is assigned a value of $\pm 3\%$ on the basis of the accuracy of the tabulated cross sections (Grodstein, 1957). The second is determined by the accuracy with which the distance from the crystal to the source could be measured; this was typically of the order of $\pm (1/64)''/(25/64)''$ or $\pm 4\%$. When this is then compared to the efficiency curves (Figures 7-9, 11-14) it yields an error of $\pm 2\%$ in efficiency in the region of interest. Hence $(\Delta \eta/\eta)$ is assigned a value of $\pm 3.5\%$.

The errors in determining the photo-fraction, ϕ_o , were normally approximately $\pm 4\%$, with $\pm 3.5\%$ due to inability to accurately determine the zero-intercept as described in Appendix I and $\pm 1\%$ due to the use of the planimeter. In the case of γ_3 , however, due to problems of background subtraction this figure should be somewhat more generous, or of the order of $\pm 6\%$ overall.

In considering the errors associated with the various terms in the expression for ρ we see right away that errors in $\eta(\gamma_1)$ and $\eta(\gamma_2)$ will cancel each other since both $\eta(\gamma_1)$ and $\eta(\gamma_2)$ are determined

by interpolation from the same set of calculations. Identical arguments apply to $\phi_o(\gamma_1)$ and $\phi_o(\gamma_2)$.

To determine the errors associated with $Y_\phi(\gamma_1)$ and $Y_\phi(\gamma_2)$ we must recall in detail how these terms are obtained. They represent the number of counts in the full-energy peaks of the response function for γ_1 and the response function for the summation of $(\gamma_2 + \gamma_3)$ after these response functions have been fitted to the net experimental spectrum. It is evident then that the sources of error for the Y_ϕ 's are in (1) the statistics of the net experimental spectrum, (2) the accuracy of the least-squares fit and (3) the accuracy of the response functions. The latter contribution was taken to be $\pm 5\%$.

Therefore,

$$\left[\frac{\Delta Y_\phi(\gamma_1)}{Y_\phi(\gamma_1)} \right]^2 = \left[\left(\frac{(\text{He}^3 + \text{He}^4)^{1/2}}{\text{He}^3 - \text{He}^4} \right)^2 + \left(\frac{\Delta X}{X} \right)^2 + (0.05)^2 \right]$$

$$\left[\frac{\Delta Y_\phi(\gamma_2 + \gamma_3)}{Y_\phi(\gamma_2 + \gamma_3)} \right]^2 = \left[\left(\frac{(\text{He}^3 + \text{He}^4)^{1/2}}{\text{He}^3 - \text{He}^4} \right)^2 + \left(\frac{\Delta Y}{Y} \right)^2 + (0.05)^2 + (0.05)^2 \right]$$

where the first term in these expressions represents the statistical accuracy of the net experimental spectrum and where X and Y are the coefficients determined by the least-squares analysis discussed earlier in this chapter. $\Delta X/X$ and $\Delta Y/Y$ were typically $\pm 2\%$ and $\pm 5\%$ respectively. It should be noted that $Y_\phi(\gamma_2 + \gamma_3)$ has two terms due to inaccuracies of the response functions, since the response functions for $(\gamma_2 + \gamma_3)$ were not determined experimentally but are rather a combination of two experimentally determined response functions.

As a further simplification, it should be noted that, in the case of the branching ratio, the statistical errors of the net spectrum cancel out. Furthermore, the errors in the response functions for γ_1 and γ_2 will also cancel since $E_{\gamma_1} \approx E_{\gamma_2}$ and since both functions are obtained by the same interpolation routine from the same data. Hence, we are able to reduce our expression for $\Delta\rho/\rho$ to

$$\left(\frac{\Delta\rho}{\rho}\right)^2 = \left(\frac{\Delta X}{X}\right)^2 + \left(\frac{\Delta Y}{Y}\right)^2 + (0.05)^2 + (0.035)^2 + (0.06)^2.$$

3. σ_{Total}

In the case of the least-squares-fitting method of analysis,

$$\sigma_{\text{Total}} = \sigma(\gamma_1) + \sigma(\gamma_2)$$

$$= \frac{Y_\phi(\gamma_1)}{N_a N_t \eta(\gamma_1) \phi_o(\gamma_1)} + \frac{Y_\phi(\gamma_2 + \gamma_3)}{N_a N_t \eta(\gamma_2) \phi_o(\gamma_2) \eta(\gamma_3) \phi_o(\gamma_3)}.$$

Therefore,

$$\begin{aligned} \Delta\sigma_{\text{Total}} = & \left[\left(\frac{\Delta N_a}{N_a} \sigma_{\text{Total}} \right)^2 + \left(\frac{\Delta N_t}{N_t} \sigma_{\text{Total}} \right)^2 + \left(\frac{\Delta Y_\phi(1)}{Y_\phi(1)} \sigma(\gamma_1) \right)^2 \right. \\ & + \left(\frac{\Delta Y_\phi(2+3)}{Y_\phi(2+3)} \sigma(\gamma_2) \right)^2 + \left(\frac{\Delta \eta(1)}{\eta(1)} \sigma(\gamma_1) \right)^2 + \left(\frac{\Delta \eta(2)}{\eta(2)} \sigma(\gamma_2) \right)^2 \\ & + \left(\frac{\Delta \eta(3)}{\eta(3)} \sigma(\gamma_2) \right)^2 + \left(\frac{\Delta \phi_o(1)}{\phi_o(1)} \sigma(\gamma_1) \right)^2 + \left(\frac{\Delta \phi_o(2)}{\phi_o(2)} \sigma(\gamma_2) \right)^2 \\ & \left. + \left(\frac{\Delta \phi_o(3)}{\phi_o(3)} \sigma(\gamma_2) \right)^2 \right]^{1/2}. \end{aligned}$$

$(\Delta N_a/N_a)$ was taken to be ± 0.01 . The stability of the instruments used was somewhat better than that (of the order of a few tenths of a percent in twelve hours); however, the absolute accuracy of the integrators was probably closer to this more generous figure.

$(\Delta N_t/N_t)$ represents an accumulation of many errors. Errors due to the measurement of the length of the target chamber and any variation in effective target thickness due to the angular spread of the beam in passing through the entrance foil (mean scattering angle $\sim 4^\circ$) are less than ± 0.01 and have been neglected compared to the other uncertainties. The uncertainty in the pressure measurement varies from 1% to 4% depending on the magnitude of the pressure. The temperature correction due to local heating in the target chamber amounts to 17% above room temperature, and is accurate to about $\pm 30\%$ so that it represents an uncertainty in N_t of $\pm 5\%$. $(\Delta N_t/N_t)$ thus is in the range from $\pm 5\%$ to $\pm 7\%$.

$(\Delta Y_\phi(i)/Y_\phi(i))$, $(\Delta \eta(i)/\eta(i))$ and $(\Delta \phi_o(i)/\phi_o(i))$ are all determined as discussed above in the error analysis of the branching ratio.

In the case of the integral method of analysis,

$$\sigma_{\text{Total}} = \frac{\Sigma}{\Phi N_a N_t} \frac{(1 + \rho)}{\eta(\gamma_1) + \rho \eta(\gamma_2)}$$

$$\begin{aligned} \frac{\Delta \sigma_{\text{Total}}}{\sigma_{\text{Total}}} = & \left[\left(\frac{\Delta \Sigma}{\Sigma} \right)^2 + \left(\frac{\Delta \Phi}{\Phi} \right)^2 + \left(\frac{\Delta N_a}{N_a} \right)^2 + \left(\frac{\Delta N_t}{N_t} \right)^2 + \left(\frac{\Delta \eta(1)}{\eta(1) + \rho \eta(2)} \right)^2 \right. \\ & \left. + \left(\frac{\Delta \eta(2)\rho}{\eta(1) + \rho \eta(2)} \right)^2 + \left(\frac{\Delta \rho}{1 + \rho} - \frac{\Delta \rho \eta(2)}{\eta(1) + \rho \eta(2)} \right)^2 \right]^{1/2}. \end{aligned}$$

$(\Delta\Sigma/\Sigma)$ is determined by the counting statistics and by how well the value of (Σ/Φ) approaches a constant.

$(\Delta\Phi/\Phi)$ is determined on the same basis as $(\Delta\phi_o(i)/\phi_o(i))$ and as such is assigned a value of $\pm 4\%$.

$(\Delta\rho/\rho)$ is determined from an analysis of the various determinations of ρ made by the least-squares fitting. From such an analysis $(\Delta\rho/\rho) = \pm 15\%$.

The remaining terms are discussed in the case of the least-squares analysis above.

Finally in the case of the single, full-energy peak analysis,

$$\sigma_{\text{Total}} = \frac{Y_\phi}{N_a N_t} \frac{1 + \rho}{\eta(\gamma_1)\phi_o(\gamma_1) + \rho\eta(\gamma_2)\phi_o(\gamma_2)\eta(\gamma_3)\phi_o(\gamma_3)}$$

$$\begin{aligned} \frac{\Delta\sigma_{\text{Total}}}{\sigma_{\text{Total}}} &= \left[\left(\frac{\Delta Y_\phi}{Y_\phi} \right)^2 + \left(\frac{\Delta N_a}{N_a} \right)^2 + \left(\frac{\Delta N_t}{N_t} \right)^2 \right. \\ &\quad + \frac{(\Delta\eta(1)\phi_o(1))^2 + (\Delta\phi_o(1)\eta(1))^2}{[\eta(1)\phi_o(1) + \rho\eta(2)\phi_o(2)\eta(3)\phi_o(3)]^2} \\ &\quad + \frac{(\rho\eta(2)\phi_o(2)\eta(3)\phi_o(3))^2}{[\eta(1)\phi_o(1) + \rho\eta(2)\phi_o(2)\eta(3)\phi_o(3)]^2} \left[\left(\frac{\Delta\eta(2)}{\eta(2)} \right)^2 \right. \\ &\quad \left. + \left(\frac{\Delta\phi_o(2)}{\phi_o(2)} \right)^2 + \left(\frac{\Delta\eta(3)}{\eta(3)} \right)^2 + \left(\frac{\Delta\phi_o(3)}{\phi_o(3)} \right)^2 \right] \\ &\quad \left. + \left(\frac{\eta(1)\phi_o(1) - \eta(2)\phi_o(2)\eta(3)\phi_o(3)}{(1+\rho)[\eta(1)\phi_o(1) + \rho\eta(2)\phi_o(2)\eta(3)\phi_o(3)]} \right)^2 (\Delta\rho)^2 \right]^{1/2}. \end{aligned}$$

$(\Delta Y_\phi / Y_\phi)$ is determined by counting statistics, while the remaining terms have all already been described in the cases above.

4. $S(E_{cm})$

For the cross-section factor, $S(E_{cm})$, defined by Burbidge et al. (1957) the errors discussed above for σ_{Total} and E_{cm} have the following combined effect:

$$S(E_{cm}) = \sigma_{Total}(E_{cm}) \cdot E_{cm} \cdot \exp(31.28 Z_1 Z_o A^{1/2} E_{cm}^{-1/2})$$

where Z_1 and Z_o are the atomic numbers of the interacting nuclei and A is the reduced mass of the system in amu.

Therefore,

$$\frac{\Delta S}{S} = \left[\left(\frac{\Delta \sigma_{Total}}{\sigma_{Total}} \right)^2 + \left(1 - \frac{1}{2} (31.28 Z_1 Z_o A^{1/2} E_{cm}^{-1/2})^2 \right)^2 \left(\frac{\Delta E_{cm}}{E_{cm}} \right)^2 \right]^{1/2}$$

where $(\Delta \sigma_{Total}/\sigma_{Total})$ and $(\Delta E_{cm}/E_{cm})$ are determined as indicated on the preceding several pages.

Having described in detail the methods used to obtain and analyze the data, we now pass on to a discussion of the results of all of this.

V. RESULTS

A. Nuclear Physical

As indicated in the discussions above, the primary object of all of this work was to obtain absolute measurements, as a function of the center-of-mass energy, of the direct-capture cross section for the reaction, $\text{He}^3(a, \gamma)\text{Be}^7$, and to use these measurements, (1) to obtain a value for the S_0 cross-section factor for this reaction at stellar energies and (2) to compare with the theoretical predictions for this type of reaction.

The experimentally determined total cross section for the reaction (including both possible gamma transitions) is shown in Figure 21 and tabulated in Table I. These values of σ_{Total} were obtained (as described in the previous chapter) in some cases by summing the cross sections for each transition and in other cases by analysis assuming a value for the branching ratio involved. Included in Table I is a notation as to which method of analysis was used in each case. These measurements cover the entire region from 181 keV to 2493 keV in the center-of-mass system, or roughly 6.0 MeV in the lab system, and cover a variation of the cross section by a factor of more than 200 from 0.018 μbarns to 3.90 μbarns .

Attempts were made to extend the measurements up into the region of the $7/2^-$ level in Be^7 at an excitation of 4.54 MeV ($E_{\text{cm}} \doteq 2950$ keV); however, the rapid rise in the background radiation in this region, due to $\text{C}^{13}(a, n\gamma)\text{O}^{16}$ and $\text{C}^{12}(a, a'\gamma)\text{C}^{12}$, made this impossible. A hint at the problems encountered is seen in the larger

relative error associated with the point at 2493 keV due primarily to poor statistics and background subtraction problems.

Since in roughly half of the cases it was possible to determine the cross sections for each transition independently, it was possible to obtain a measurement of the branching ratio between these two transitions as a function of energy. This is plotted in Figure 23, where the branching ratio is defined as the ratio of the cascade transition's cross section to that of the crossover transition. From the experimental measurements it is not possible to say much about the energy dependence of ρ other than that it is essentially constant. Analysis as such indicates that over this energy region

$$\rho = 0.374 \pm 0.056,$$

or, in other words, that 73% of the captures proceed directly to the ground state via γ_1 , while 27% go through the 432 keV excited state via γ_2 .

The energy range covered in these measurements is somewhat smaller than in the total cross-section measurements, mainly due to the fact that at alpha-particle energies of 4 MeV and higher, thin lead absorbers were used between the crystal and the target to reduce the amount of low-energy radiation swamping the detector and thereby invalidated the shape fitting technique described in the last chapter.

The errors indicated on these plots are the relative errors described in the preceding chapter and do not include the absolute uncertainties of the experiment. In the case of the branching ratio, however, due to its insensitivity to such absolute errors, the value of 0.374

can be quoted independent of any absolute errors. For the case of the total cross section, however, when the absolute uncertainty is combined with the roughly 10% relative uncertainty in each point, the total uncertainty should probably be quoted as $\pm 15\%$.

Also indicated on both of these plots are the theoretical predictions as to the energy behavior of these two quantities as derived from Part II. In both of these cases the agreement between theory and experiment is very close. It should also be remembered, as noted at the end of Part II, that only three parameters are available to obtain these fits, the nuclear radius (R_o) and the reduced widths for each final state ($\theta_{3/2}^2$ and $\theta_{1/2}^2$), where the subscript denotes the J-value of the state. R_o was varied around the value of 2.80 fermis deduced from the elastic scattering of He^3 and He^4 (Miller and Phillips, 1958; Jones et al., 1962; Tombrello and Parker, 1962), and for each value of R_o the two reduced widths were varied to normalize each of the two curves to the data. Listed below are the resulting values of the parameters,

$R_o = 2.4 \text{ fermis} \rightarrow$	$\theta_{3/2}^2 = 1.86$
	$\theta_{1/2}^2 = 1.55$
	$\theta_{3/2}^2 = 1.25$
$R_o = 2.8 \text{ fermis} \rightarrow$	$\theta_{1/2}^2 = 1.05$
	$\theta_{3/2}^2 = 0.88$
$R_o = 3.2 \text{ fermis} \rightarrow$	$\theta_{1/2}^2 = 0.73$

Actually it turned out that the fits of σ_{Total} and ρ were completely independent of the choice of R_o , and so the value of 2.80 fermis was

adopted in agreement with the elastic scattering analysis cited above and in agreement with the value of 2.84 fermis obtained by Hofstadter (1957). Hence, it can be said that the fits shown were obtained with the use of only two energy independent parameters.

It is somewhat surprising that the extra-nuclear approximation under which the theoretical calculations were made should be valid over such a large range of energy as demonstrated by the quality of the fits obtained. The validity of this approximation depends, it was noted, on the closeness of the various phase shifts to their corresponding hard-sphere phase shifts. It has been shown in the various elastic scattering experiments (Miller and Phillips, 1958; Jones et al., 1962; and Tombrello and Parker, 1962) that the s-wave phase shift and both the d-wave phase shifts are accurately described by their hard-sphere phases for a nuclear radius of 2.80 fermis, over the entire region covered in this experiment. The p-wave and the f-wave phase shifts, however, do not satisfy this condition. In the case of the f-waves this is due to the effects of the two $\ell = 3$ resonances just above this region. (See Table II.)

Figure 22 depicts graphically the way in which the various ℓ -waves contribute to the total cross section in the theoretical calculations. These curves indicate vividly that almost all the contributions to the total cross section come from the E1 transitions which are contributed by the s- and d-waves. The contributions of the p-waves and f-waves, combined in the M1 and E2 cross sections, never amount to more than four per cent of the total cross section. This, combined with the agreement of the s- and d-wave phase shifts with the $R_o = 2.80$ fermis

hard-sphere phases, indicates why we were able to obtain such a good fit over such a large region of energy in spite of our neglect of the contributions to our matrix elements from the region inside the nuclear radius. Any change in $\sigma(M1)$ or $\sigma(E2)$ from such contributions, even to the extent of increasing them by a factor of 5 or so, would not have had an appreciable effect on the total cross section.

Before leaving Figure 22 it is also interesting to note that it is the rapidly increasing d-wave cross section that is keeping the total non-resonant cross section still rising almost linearly at $E_a = 6.00$ MeV, while the s-wave contribution has almost completely leveled off at about 2.0 μ barns.

As noted in the previous sections, to check the accuracy of the shape-fitting and unfolding analysis utilized above, a point was taken using a coincidence technique to measure only the cross section for the cascade transition, $\sigma(\gamma_2)$. This measurement agreed well with the other determinations of $\sigma(\gamma_2)$ and, converted to σ_{Total} using the measured branching ratio, is shown on Figure 21 at a center-of-mass energy of 1378 keV as the solid square.

Attempts were also made to measure the angular distribution of the capture radiation as a function of energy in order to compare it with the theoretically predicted values of the parameters a_1 , a_2 , a_3 and a_4 . Measurements of the yield were made with the solid crystal at 90° and 0° to the incident beam and with the well crystal. However, due mainly to the poor angular resolution of the crystals in the close-up geometry necessitated by the low cross sections involved, the results

were indefinite and the best that could be said was that the radiation was isotropic to $\pm 20\%$. Therefore, all the data were analyzed under the assumption that the radiation pattern was isotropic. A plot of the theoretically predicted values of a_i as a function of alpha-particle energy is shown in Figure 24. From these curves it is apparent that any predicted anisotropy is small. A calculation at 3.00 MeV, near the maximum anisotropy, predicts a 0° to 90° asymmetry of only 7%. Applying smoothing due to the crystal geometry reduces the effect to 3% and shows that such an effect is well buried in our 10% uncertainties.

B. Astrophysical

The final phase of the discussion of the results of this experiment involves the conversion of the experimental and theoretical cross sections to the cross-section factor defined by Burbidge et al. (1957),

$$S(E_{cm}) = \sigma(E_{cm})E_{cm} \exp(31.28 Z_1 Z_o A^{1/2} E_{cm}^{-1/2}) \text{keV-barns.}$$

This quantity is tabulated in Table I and plotted in Figure 25. On the basis of the accuracy of the theoretical fit to the experimental measurements, the theoretical calculation was used to extrapolate $S(E)$ to zero-energy and obtain the low-energy cross-section factor, S_0 ,

$$S_0 = 0.47 \pm 0.07 \text{ keV-barns.}$$

This is considerably smaller than the value of 1.2 keV-barns arrived at by Holmgren and Johnston (1959) and substantially reduces the importance of this reaction (Fowler, 1960) as a termination for the proton-proton chain at temperatures below 15×10^6 $^\circ\text{K}$.

The expression for the reaction rate (r_{pp}) of the $H^1(p, \beta^+ \nu)D^2$ reaction has been given by Burbidge et al. (1957). The He^4 production rate (R_a) may then be related to r_{pp} as follows,

$$R_a = F_a r_{pp}$$

where F_a is one-half the factor $\phi(a)$ defined by Fowler (1958) since we are relating R_a to r_{pp} and not to the equilibrium rate of the $He^3(He^3, 2p)He^4$ reaction. Hence, once equilibrium has been established between the He^3 -producing and the He^3 -destroying reactions (at a temperature of about 10×10^6 °K in stars like the sun), F_a is given by the following expression,

$$F_a(\xi) = \frac{1}{2} \left[1 - \xi + \xi \left(1 + \frac{2}{\xi} \right)^{1/2} \right],$$

where

$$\xi = \frac{(f_{34} S_{34})^2}{f_{11} S_{11} f_{33} S_{33}} \left(\frac{X_{He}}{4X_H} \right)^2 \exp(-100 T_6^{-1/3}),$$

and where

$$S_{34} = S_o \text{ for } He^3(a, \gamma)Be^7$$

$$S_{11} = S_o \text{ for } H^1(p, \beta^+ \nu)D^2$$

$$S_{33} = S_o \text{ for } He^3(He^3, 2p)He^4.$$

The f 's are the respective electron screening corrections (see Fowler, 1960); the X_i 's are the concentrations by mass, and T_6 is the temperature in 10^6 °K.

F_a was calculated in this manner over the range $10 \leq T_6 \leq 30$, using the following values of the various parameters (Fowler, 1962),

and is plotted in Figure 28:

$$S_{11} = 3.5 \times 10^{-22} \text{ keV-barns} \quad f_{11} S_{11} = 3.7 \times 10^{-22} \text{ keV-barns}$$

$$S_{33} = 1300 \text{ keV-barns} \quad f_{33} S_{33} = 1600 \text{ keV-barns}$$

$$S_{34} = 0.47 \text{ keV-barns} \quad f_{34} S_{34} = 0.59 \text{ keV-barns}$$

$$\left(\frac{X_{\text{He}}}{X_{\text{H}}} \right) = 1.0$$

At temperatures below $10 \times 10^6 \text{ }^{\circ}\text{K}$, where equilibrium has not been established between the $\text{H}^1(\text{p}, \beta^+ \nu)\text{D}^2$ reaction and the various termination reactions, F_a is governed by the fact that the proton-proton chain at such temperatures tends to stop at the production of He^3 , reducing F_a to zero at $5 \times 10^6 \text{ }^{\circ}\text{K}$. In this region F_a is independent of the value of S_{34} measured in this experiment; hence, it can be taken correctly as one-half of the factor, $\phi(a)$, plotted by Fowler (1960) and is plotted as such in Figure 28 for temperatures below $10 \times 10^6 \text{ }^{\circ}\text{K}$.

The variation of F_a over the range $5 \leq T_6 \leq 30$ can be summarized qualitatively as follows:

(1) In the region $5 \leq T_6 \leq 10$ the $\text{He}^3(\text{He}^3, 2\text{p})\text{He}^4$ reaction rate decreases rapidly, and the proton-proton chain tends to stop at the production of He^3 , reducing F_a to zero at $5 \times 10^6 \text{ }^{\circ}\text{K}$.

(2) When equilibrium is first reached between the He^3 -producing and the He^3 -destroying reactions in the neighborhood of $10 \times 10^6 \text{ }^{\circ}\text{K}$, F_a takes on the value of 0.500 since at that temperature all of the terminations go through the $\text{He}^3(\text{He}^3, 2\text{p})\text{He}^4$ reaction which requires

two $H^1(p, \beta^+\nu)D^2$ reactions for the production of each He^4 .

- (3) At this point, the alternate terminations through the $He^3(a, \gamma)Be^7$ reaction which require only one $H^1(p, \beta^+\nu)D^2$ reaction for each He^4 produced begin to become important, and F_a gradually increases to its new equilibrium value of 1.00 at temperatures in excess of $20 \times 10^6 \text{ }^\circ\text{K}$.

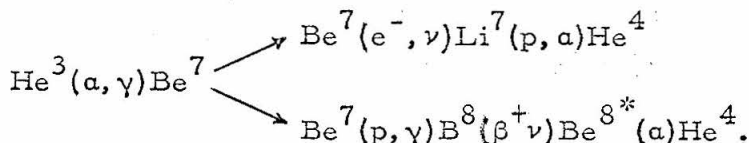
Once F_a has been calculated in this manner, it is of interest to determine what fraction of the He^4 is formed through each termination. It can be shown that the fraction going through the Be^7 terminations is given by

$$Be^7/He^4 = 2 - \frac{1}{F_a}.$$

The fraction going through the $He^3(He^3, 2p)He^4$ reaction is therefore,

$$\begin{aligned} [He^3(He^3, 2p)He^4]/He^4 &= 1 - \frac{Be^7}{He^4} \\ &= \frac{1}{F_a} - 1. \end{aligned}$$

Furthermore, there are two possible ways that the Be^7 termination may go



The fraction going through the B^8 reaction is given by

$$B^8/Be^7 = \frac{\tau_e}{\tau_e + \tau_p}$$

where τ_e is the mean lifetime of Be^7 for electron-capture in a fully ionized region,

$$\tau_e = \frac{10^4}{1.83} \frac{T_6^{1/2}}{\rho(1+x_H)} \text{ days,} \quad (\text{Bahcall, 1962})$$

and where τ_p is the mean lifetime of Be^7 for proton-capture,

$$\tau_p = \frac{0.933 \times 10^{-10}}{\rho x_{H17} f_{17} S_{17}} \left(\frac{e^7}{\tau^2} \right) \text{ days,} \quad (\text{Burbidge et al., 1957})$$

$$\tau = 42.48 \left(Z_o^2 Z_1^2 \frac{A}{T_6} \right)^{1/3}.$$

ρ is the density of the medium; x_H is the concentration by mass of hydrogen. The Z 's are the atomic numbers of the interacting nuclei, and A is the reduced mass of the system. $S_{17} = S_o$ for $Be^7(p,\gamma)B^8$, and f_{17} is the screening factor mentioned above.

The fraction (B^8/Be^7) was calculated in this manner over the range, $10 \leq T_6 \leq 30$, using the following values for the parameters (Fowler, 1962):

$$S_{17} = 0.030 \text{ keV-barns} \quad f_{17} S_{17} = 0.037 \text{ keV-barns}$$

$$x_H = 0.50.$$

The fraction of Be^7 terminations going through the Li^7 reaction is thus

$$\text{Li}^7/\text{Be}^7 = 1 - \frac{\text{B}^8}{\text{Be}^7},$$

and these two fractions may now be combined with the Be^7/He^4 fraction to determine the fraction of the He^4 produced through each termination.

In summary, therefore,

$$[\text{He}^3(\text{He}^3, 2p)\text{He}^4]/\text{He}^4 = 1 - \frac{\text{Be}^7}{\text{He}^4}$$

$$\text{Li}^7/\text{He}^4 = \frac{\text{Be}^7}{\text{He}^4} \cdot \frac{\text{Li}^7}{\text{Be}^7}$$

$$\text{B}^8/\text{He}^4 = \frac{\text{Be}^7}{\text{He}^4} \cdot \frac{\text{B}^8}{\text{Be}^7}.$$

All three of these curves and the ratio, Be^7/He^4 , are plotted in Figure 26 to show the way that the importance of each termination varies with temperature. The dependence of the ratio Be^7/He^4 on the relative abundances of helium and hydrogen is shown in Figure 27 for the cases of $(X_{\text{He}}/X_{\text{H}}) = 0.25, 1.00$ and 2.00 . The first value corresponds roughly to the initial conditions in the sun (Fowler, 1958), while the present sun as a whole falls near the value of 1.00 , approaching 2.00 at the center (Bahcall et al., 1963). This indicates that in the present sun, with an effective temperature of 15×10^6 °K (Fowler, 1962), the proton-proton chain goes to completion through the $\text{He}^3(a, \gamma)\text{Be}^7$ reaction approximately one-half of the time.

Once the fraction of He^4 produced through each termination is known, it is of interest to calculate the way in which the rate of energy

production (R_ϵ) also varies with temperature because of the differences in the He^4 -production rates of the various terminations and the differences in the effective Q 's of those terminations due to the various neutrino energy losses.

Consistent with the fact that at high temperatures one He^4 is produced for each $\text{H}^1(p, \beta^+\nu)\text{D}^2$ reaction and with the fact that the maximum effective Q for the completed chain is 26.2 MeV, we may write

$$R_\epsilon = F_\epsilon \cdot \epsilon_{pp}$$

where

$$\epsilon_{pp} = 26.2 r_{pp} \text{ MeV} .$$

(This is just twice the value given by Burbidge et al. (1957) under the assumption that the only termination was the $\text{He}^3(\text{He}^3, 2p)\text{He}^4$ reaction.)

F_ϵ , the energy generation rate factor similar to F_a , can now be calculated on the basis of a knowledge of the effective Q 's for each termination and a knowledge of the fraction of He^4 produced through each of those terminations as determined above. Hence,

$$F_\epsilon = F_a \left[\left(1 - \frac{\text{Be}^7}{\text{He}^4}\right) \frac{26.2}{26.2} + \left(\frac{\text{Li}^7}{\text{He}^4}\right) \frac{25.6}{26.2} + \left(\frac{\text{B}^8}{\text{He}^4}\right) \frac{19.1}{26.2} \right].$$

This curve is plotted in Figure 28 with F_a , and, as is the case of F_a , the region below $T_6 = 10$ is taken from Fowler (1960).

The variation of F_ϵ over the range $5 \leq T_6 \leq 30$ can be described qualitatively as follows:

- (1) At temperatures below 10×10^6 °K the p-p chain tends to terminate at the $D^2(p, \gamma)He^3$ reaction, and F_ϵ decreases, approaching at 5×10^6 °K a value of 0.255, the ratio of the effective Q for the formation of He^3 from three protons (6.68 MeV) to the maximum effective Q for the chain (26.2 MeV).
- (2) After equilibrium has been reached between the termination reactions and the $H^1(p, \beta^+ \nu)D^2$ reaction in the neighborhood of 10×10^6 °K, F_ϵ becomes 0.500 since at that point all of the terminations go through the $He^3(He^3, 2p)He^4$ reaction which requires two $H^1(p, \beta^+ \nu)D^2$ reactions for each He^4 produced.
- (3) As the temperature is increased, the Li^7 termination becomes increasingly important, and, requiring only one $H^1(p, \beta^+ \nu)D^2$ reaction for each He^4 produced, pushes F_ϵ up towards 0.98.
- (4) As the temperature continues to increase, however, the onset and eventual domination of the B^8 termination, with its large energy losses due to the energetic β -decay of B^8 , prevent F_ϵ from reaching 0.98, and after going through a maximum of 0.89 at just above 20×10^6 °K, F_ϵ approaches a value of 0.73, the ratio of effective Q of the B^8 termination (19.1 MeV) to the maximum effective Q (26.2 MeV).

SUMMARY

The absolute cross section for the $\text{He}^3(\alpha, \gamma)\text{Be}^7$ reaction has been measured with a total error of $\pm 15\%$ over the range of center-of-mass energies from 181 keV to 2493 keV. Over this entire range these measurements have confirmed the direct-capture theories of Christy and Duck (1961) and Tombrello and Phillips (1961). The measurements have been used to obtain a new value for the low-energy cross-section factor, $S_0 = 0.47 \pm 0.07$ keV-barns, for this reaction, and this value of S_0 has been used to recompute the effect of this reaction on the termination of the proton-proton chain in nuclear astrophysics.

APPENDIX I

Gamma-Ray Spectrometry

Although there are other ways of detecting gamma radiation, such as geiger counters, ionization chambers, pair-spectrometers, etc., the inability of the first two devices to determine the gamma-ray energy without the use of a series of absorbers and the bulkiness of the last device together with its insensitivity to gamma radiation with energy below the pair-production threshold, as well as the low efficiency of all such devices, have made the use of scintillation phosphors with their high sensitivity to gamma radiation and the proportionality of their response to the energy of the incident gamma ray, the standard method for detecting nuclear gamma radiation. Of the various scintillation phosphors available, NaI(Tl) is the one accepted for general use when considering all the various characteristics of density, decay time and relative pulse height. For particular applications where one of these factors may be especially critical, however, the choice may be quite different. For instance, by going from NaI(Tl) to a liquid phosphor a reduction of the decay time by a factor of 100 is possible (Harshaw, 1962).

A. Efficiency Calculations

In general, given a source and a detector, in order to say anything quantitative about how many interaction or decays take place in the target we must be able to say (1) how many gamma rays have interacted with the crystal and (2) what fraction of the emitted gamma rays

interact with the NaI(Tl) crystal. Considering the second point first, because its solution is much more straightforward, we will discuss below the calculation of the efficiencies of NaI(Tl) crystals for detecting gamma rays.

The probability of a gamma ray interacting with a NaI(Tl) crystal is $\{1 - e^{-\sigma \rho l}\}$ where σ is the total cross section for such an interaction in (cm^2/g) as tabulated by Grodstein (1957), ρ is the density of NaI (3.667 g/cm^3) and l is the length of the path which the gamma ray travels in the crystal. For a particular source-crystal geometry and a particular gamma-ray energy we can then calculate the total efficiency (η_o) of the crystal by multiplying the probability of interaction by the number of gamma rays per steradian ($dN(\theta, \phi)$), dividing by the total number of such gamma rays (N_o) emitted by the source and then integrating the expression over the whole crystal.

The number of gamma rays per steradian is given by,

$$dN(\theta, \phi) = \frac{N_o}{4\pi} W(\theta, \phi) \sin \theta d\theta d\phi$$

where $W(\theta, \phi)$ depends on the angular distribution of the gamma rays emitted by the source. In the present case efficiencies were calculated for the cases of isotropic and $\sin^2 \theta$ radiation patterns.

$$dN(\theta, \phi)_{\text{isotropic}} = \frac{N_o}{4\pi} \sin \theta d\theta d\phi$$

$$dN(\theta, \phi)_{\sin^2 \theta} = \frac{3N_o}{8\pi} \sin^3 \theta d\theta d\phi$$

Thus, we can write

$$\eta_o(\text{iso}) = \frac{1}{4\pi} \iint_{\text{crystal}} [1 - e^{-\sigma\rho l(\theta, \phi)}] \sin \theta d\theta d\phi,$$

$$\eta_o(\sin^2 \theta) = \frac{3}{8\pi} \iint_{\text{crystal}} [1 - e^{-\sigma\rho l(\theta, \phi)}] \sin^3 \theta d\theta d\phi.$$

In the present experiment the geometries of interest were (1) the well crystal with the beam axis ($\theta = 0^\circ$) along the axis of the crystal for both isotropic and $\sin^2 \theta$ radiation, (2) the solid crystal at 0° and 90° for isotropic radiation and (3) the solid crystal at 0° and 90° for $\sin^2 \theta$ radiation. In all but the last case ($\sin^2 \theta$ at 90°) there is sufficient cylindrical symmetry so that $l(\theta, \phi) = l(\theta)$, and we may write

$$\eta_o(\text{iso.}) = \frac{1}{2} \int_{\text{crystal}} (1 - e^{-\sigma\rho l(\theta)}) \sin \theta d\theta,$$

$$\eta_o(\sin^2 \theta @ 0^\circ) = \frac{3}{4} \int_{\text{crystal}} (1 - e^{-\sigma\rho l(\theta)}) \sin^3 \theta d\theta.$$

In order to eliminate the ϕ -dependence in the $\sin^2 \theta$ efficiency at 90° we can reexpress the integral as

$$\eta_o(\sin^2 \theta @ 90^\circ) = \frac{3}{8\pi} \int_0^{90^\circ} d\beta \int_0^{2\pi} da \sin^2 \theta \sin \beta (1 - e^{-\sigma\rho l(\beta)})$$

where a and β correspond to ϕ and θ respectively in the crystal's coordinate system. Then after the method of Rose (1953) we can re-express $\sin^2 \theta$ as

$$\sin^2 \theta = \frac{2}{3} (1 - P_2(\cos \theta))$$

$$P_2(\cos \theta) = P_2(\cos \beta) P_2(\cos 90^\circ) + \dots \cos a + \dots \cos 2a.$$

Therefore,

$$\begin{aligned} \eta_o(\sin^2 \theta @ 90^\circ) &= \frac{3}{8\pi} \int_0^{\beta_o} d\beta \int_0^{2\pi} da \frac{2}{3} [1 + \frac{1}{2} P_2(\cos \beta)] \sin \beta (1 - e^{-\sigma \rho l(\beta)}) \\ &\quad + \frac{3}{8\pi} \int_0^{\beta_o} d\beta \int_0^{2\pi} da \frac{2}{3} [\dots \cos a + \dots \cos 2a] \sin \beta (1 - e^{-\sigma \rho l(\beta)}), \end{aligned}$$

where the second double integral goes to zero on integration over a .

Therefore,

$$\begin{aligned} \eta_o(\sin^2 \theta @ 90^\circ) &= \frac{3}{4} \int_0^{\beta_o} d\beta \frac{2}{3} (1 + \frac{1}{2}(1 - \frac{3}{2} \sin^2 \beta)) \sin \beta (1 - e^{-\sigma \rho l(\beta)}) \\ &= \frac{3}{4} \left(\int_0^{\beta_o} (1 - e^{-\sigma \rho l(\beta)}) \sin \beta d\beta \right. \\ &\quad \left. - \frac{1}{2} \int_0^{\beta_o} (1 - e^{-\sigma \rho l(\beta)}) \sin^3 \beta d\beta \right) \\ &= \frac{3}{2} \eta_o(\text{iso}) - \frac{1}{2} \eta_o(\sin^2 \theta @ 0^\circ). \end{aligned}$$

The integrals in question were evaluated numerically using Simpson's rule on the Burroughs' 220 computer, using the following expressions for $l(\theta)$, (see Figure 6):

Well crystal: (Figure 6B)

$$\begin{array}{ll} 0^\circ \leq \theta \leq \theta_1 & \epsilon(\theta) = b/\cos \theta \\ \theta_1 \leq \theta \leq \theta_2 & \epsilon(\theta) = \frac{b+a}{\cos \theta} - \frac{R_1}{\sin \theta} \\ \theta_2 \leq \theta \leq \theta_3 & \epsilon(\theta) = (R_2 - R_1)/\sin \theta \\ \theta_3 \leq \theta \leq \theta_4 & \epsilon(\theta) = \frac{b+a}{\cos \theta} - \frac{R_1}{\sin \theta} \end{array}$$

Solid crystal: (Figure 6A)

$$\begin{array}{ll} 0^\circ \leq \theta \leq \theta_1 & \epsilon(\theta) = b/\cos \theta \\ \theta_1 \leq \theta \leq \theta_2 & \epsilon(\theta) = \frac{R}{\sin \theta} - \frac{a}{\cos \theta} \end{array}$$

The efficiencies thus calculated over the range of gamma-ray energies from 0.400 to 8.00 MeV are presented in Figures 7, 8, 9, 11-14.

Before leaving the problem of efficiency calculations, it should be noted that while the above calculations have assumed a point source, in the cases where the detector is at 0° (Figure 5A) the target region in which the gamma rays are produced is actually a line source perpendicular to the face of the crystal. The effective efficiency in this configuration, assuming a uniform source, can be written as

$$\eta_o = \int_a^b \eta_o(x) dx / (b - a)$$

where $(b - a)$ is the length of the line source. These calculations were also carried out for the present experiment but were not considered of general enough interest to be presented in detail.

Having thus determined η_0 for all the cases of interest, it is further necessary to apply absorption corrections to η_0 to take into account the loss of photons in the various materials between the target and the crystal, namely the platinum liner in the target chamber, the target chamber and the crystal housing, as well as the lead absorbers used in a few cases. This correction was performed by multiplying η_0 by the attenuation factor, $e^{-\sum_i \sigma_i \rho_i l_i}$ where σ_i , ρ_i and l_i are the terms discussed previously for the various materials.

Hence

$$\eta = \eta_0 e^{-\sum_i \sigma_i \rho_i l_i}$$

where l_i was taken as an average value of the thickness of material traversed by the gamma rays. An exact calculation of this attenuation would have required the expansion of l_i as $l_i(\theta, \phi)$, and the integration of the expression over the solid angle of the crystal as

$$\eta = \int_{\text{crystal}} \frac{1}{4\pi} W(\theta, \phi) [1 - e^{-\sigma \rho l(\theta, \phi)}] e^{-\sum_i \sigma_i \rho_i l_i(\theta, \phi)} \sin \theta d\theta d\phi .$$

Since the attenuation correction typically amounted to only about 2.5% this exact calculation was considered unnecessary and the approximate expression noted above was utilized.

In this way then, the number of gamma-ray interactions in the detector was related to the number of gamma rays emitted by the source for all the situations encountered in the experiment, and we are now brought to the problem of deciding how many interactions take place in

the crystal.

B. Response Function Determination

1. Characteristics of Gamma-Ray Response Functions

Given a monochromatic gamma-ray source, a NaI(Tl) detector and a pulse-height analyzer one soon discovers that the pulse-height spectrum of the output of the scintillator is not characterized by a simple pulse-height distribution. Instead, one finds that the output pulse-height distribution has as many as four or five peaks superimposed on a broad distribution stretching from zero-energy to almost the full photon energy. See, for example, Figures 15 and 16. Furthermore, the number of peaks in this spectrum as well as their relative importance and shape and the magnitude of the broad, underlying structure, depends strongly on the gamma-ray energy, the size of the crystal and the geometry involved.

The complicated pulse-height distribution of the output of such a spectrometer is caused by the large variety of ways in which a gamma ray can interact with the NaI(Tl) crystal. Evans (1955) lists the following four different kinds of interactions that the photons can have with matter:

- (1) Interaction with atomic electrons,
- (2) Interaction with nucleons,
- (3) Interaction with the electric field surrounding the nuclei and electrons, and
- (4) Interaction with the meson field surrounding the nucleons.

In each of these interactions the photon may be either fully absorbed, elastically scattered or inelastically scattered, thus providing a total of twelve different events that may occur. Only three of these turn out to be important for the interaction of gamma rays with NaI(Tl) crystals, in the energy range $0.400 \leq E_{\gamma} \leq 4.500$ MeV. These are (1) photoelectric absorption, (2) Compton scattering and (3) pair production. Detailed discussions of the nature of these interactions and their dependence on the energy of the incident gamma ray are available elsewhere, e.g. Evans (1955), and there seems little to be gained from repeating that information here. We will pause here only briefly to discuss the characteristic features of such a gamma-ray spectrum and their origins in the various mechanisms by which the gamma ray can interact with the scintillator.

In photoelectric events the entire energy of the incident photon is transferred to an atomic electron. If this electron is stopped within the scintillator the entire energy of the gamma ray is transferred to the crystal, and the output pulse of the spectrometer corresponds to the full energy of the incident quantum. If the size of the crystal is large compared to the range of the photo-ejected electron, then such full-energy events will be the most likely result of a photoelectric interaction, and one would expect the output spectrum of such events to have a large peak at the high energy end of the spectrum (the full-energy peak) followed by a smooth tail stretching to lower energies and corresponding to cases where the electron escaped from the crystal before losing all its energy.

The range of such secondary electrons in NaI(Tl) is given approximately by Woodbury (1953) as,

(1) $E_e < 2 \text{ MeV}$, the range is 1.2 mm/MeV .

(2) $E_e > 3 \text{ MeV}$, the range is 1.5 mm/MeV .

Hence, for an electron with an energy of 4 MeV (the maximum encountered in this experiment) the range is only of the order of 6 mm and is therefore much smaller than the crystal dimensions of three inches or approximately 75 mm .

In Compton scattering the incident photon of energy (E_γ) is scattered by an atomic electron through an angle θ and degraded to an energy (E'_γ) where

$$\left[E_\gamma / \left(1 + \frac{2E_\gamma}{m_0 c^2} \right) \right] \leq E'_\gamma \leq E_\gamma$$

the upper limit holding for the case of forward scattering ($\theta = 0^\circ$) where no energy is transferred to the crystal and lower limit for the case of backward scattering ($\theta = 180^\circ$). The energy of the scattered electron is thus given by

$$0 \leq E_e \leq \left(E_\gamma - \frac{E_\gamma}{1 + \frac{2E_\gamma}{m_0 c^2}} \right)$$

and from this interaction one would thus expect some sort of a broad distribution of pulse-heights stretching from zero energy to some limit or shoulder at $\left(E_\gamma - \frac{E_\gamma}{1 + \frac{2E_\gamma}{m_0 c^2}} \right)$. The scattered photon, however, still

has the possibility of further interacting with the crystal so as to eventually lose its entire energy to the crystal. Such events would yield further contributions to the full-energy peak discussed above.

Finally, for the case of pair production the entire energy of the incident photon is transferred into an electron-positron pair. As discussed above if the size of the scintillator is large compared to the ranges of the pair, their entire kinetic energy ($E_{\gamma} - 2m_0c^2$) will be transferred to the crystal. The remaining 1.022 MeV of the energy appears in the two 511-keV gamma rays arising from the annihilation of the created positron. These two gamma rays are, of course, free to further interact with the scintillator or to escape from it completely. The latter situation will give rise to another peak in the pulse height spectrum 1.022 MeV lower than the full-energy peak which will be referred to as the double-escape peak. If one of the annihilation quanta loses its full energy to the crystal it will give rise to another peak 511 keV below the full energy peak (the single-escape peak), and if both of the annihilation quanta are completely absorbed in the crystal the event will contribute a count to the full-energy peak. Further, of course, these annihilation quanta may interact but not lose their entire energy to the crystal, undergoing Compton scattering and giving rise to additional Compton distributions between the double- and single-escape peaks and between the single-escape and full-energy peaks. The latter is, however, the position of the shoulder of the primary Compton distribution, and this will undoubtedly mask the secondary effect.

Hence, in conclusion, starting from the full-energy peak we would

expect to find the following characteristic features in the pulse-height spectrum of a monoenergetic gamma ray, assuming that the range of all electrons and positrons is small compared to the crystal dimensions: (Naturally those structures applying to pair production will occur only for gamma rays whose energy is greater than the threshold for such an interaction, 1.022 MeV.)

- (1) the full-energy peak at $\langle E_{\gamma} \rangle$ with contributions from photoelectric events, Compton scattering events where the scattered quantum eventually loses its entire energy to the crystal and pair production events in which both of the annihilation quanta are totally absorbed in the crystal,
- (2) the shoulder of the primary Compton distribution,
- (3) the single-escape peak at $(E_{\gamma} - 511 \text{ keV})$,
- (4) the shoulder of the Compton distribution for one annihilation quantum,
- (5) the double-escape peak at $(E_{\gamma} - 1022 \text{ keV})$, and
- (6) the tail of the primary Compton distribution.

All of these features may indeed be seen in Figures 15 and 16, the response functions of the crystals used in this experiment.

It is interesting to note one significant difference in the appearance of the response functions of these two crystals in the shape of the shoulder of the primary Compton distribution; for the solid 3" x 3" crystal this shoulder is much sharper and more pronounced than for the 3" x 3" well crystal. This can easily be understood by realizing that events in this part of the Compton distribution arise from cases where the incident

photon is scattered backwards and the low-energy back-scattered quantum escapes from the crystal. In the case of the well crystal, since the source is in the center of the crystal, in almost all directions a back-scattered photon must travel through at least 1.125 inches of the crystal before completely escaping, whereas in the entire front one third of the solid 3" x 3" crystal it is possible for the back-scattered quanta to escape through less crystal than that. Hence, since the half-thickness of NaI(Tl) to such a back-scattered quantum is approximately 3/8", in the well crystal it is always extremely likely that the back-scattered gamma ray will be absorbed in the crystal transferring the event from the Compton distribution to the full-energy peak.

2. Experimental Measurement of Response Functions

Given such a complicated spectral response, if only one gamma-ray transition is involved (i.e. a monoenergetic source) the analysis of the spectrum, although somewhat indefinite, is none-the-less reasonably straightforward. When a second gamma-ray transition is added to the spectrum, however, any analysis of the two transitions must require a separation of the total spectrum into its two component spectra, one for each transition, each of which can then be handled independently as the spectrum of a monoenergetic source. Such a prerequisite separation can be performed only if the response functions of the detector for the various gamma-ray energies are known, and since such response functions are highly dependent on E_γ and the experimental arrangement, the only logical way to approach the problem is to obtain these response

functions experimentally under conditions closely approximating those of the experiment to be analyzed.

In the present case, since the gamma-ray energies encountered cover the range $0.432 \leq E_{\gamma} \leq 4.080$ MeV, the response functions of each of the various scintillators were measured at a number of points covering this region so as to allow reasonably accurate interpolation for intermediate energies. The choice of the reactions to be used to obtain such functions is governed by the considerations (1) that there be no strong competing gamma radiation which might confuse the desired function and (2) that the reaction be reasonably strong so that the subtraction of background can be accomplished with reasonable accuracy and reliability. On the basis of such considerations the following reactions were chosen for various values of E_{γ} covering the energy range noted above:

$E_{\gamma} = 0.432$ MeV	$B^{10}(p, a_1)Be^7$
1.277 MeV	$F^{19}(a, p_1)Ne^{22}$
1.632 MeV	$Na^{23}(p, a_1)Ne^{20}$
1.980 MeV	$O^{18}(p, p_1)O^{18}$
2.367 MeV	$C^{12}(p, \gamma)N^{13}$
3.51 MeV	$C^{12}(p, \gamma)N^{13}$
3.560 MeV	$Be^9(p, a_2)Li^6$
4.433 MeV	$N^{15}(p, a_1)C^{12}$

In each of these cases, runs on the target in question were made for a definite charge accumulation and then immediately followed by background runs in the same geometry for an identical accumulation of

charge. Depending on the reaction, these background runs were made either at exactly the same energy on the target backing or on exactly the same target at a beam energy just slightly removed from the resonant energy. Because of the dependence of such response functions on the target-crystal geometry and shielding, all of these runs were taken in geometries as close as possible to those of the data-runs and with identical shielding. Dead time corrections were applied to each of the spectra by multiplying them by the ratio of the clock-time for the run to the live-time of the analyzer during the run. The background spectrum was then subtracted from the target spectrum, the net spectrum normalized to 1.000 at the top of the full energy peak and this spectrum then plotted as a function of $(E - E_{\gamma})$. Such a calibration was carried out over the full range of energies listed above for the 3" x 3" crystal (Figure 15) and the 3" x 3" well crystal (Figure 16). A similar calibration was performed for the 2" x 2" crystal over the range from 432 keV to 661 keV, since it was used only in the coincidence experiment and then only in the energy region around 432 keV.

The use of $(E - E_{\gamma})$ as an abscissa was suggested by a paper of Okano (1960). The actual decision to use this coordinate was made on the basis that in such a representation related structures (e.g. the single-escape peaks) remain fixed thus eliminating all problems due to the crossing of these structures as they move along the abscissa, making the interpolation functions monotonic and facilitating interpolation since as the gamma-ray energy is varied only one coordinate of the various structures changes, their height relative to that of the full-energy peak.

3. Calculation of Coincidence-Summing Response Functions

Before discussing the use of these response functions to sort out complex gamma-ray spectra, we should pause a moment to describe how these single response functions can be combined to give the coincidence-sum response function corresponding to two single gamma rays interacting with the crystal simultaneously to produce a pulse-height distribution with a full-energy peak at an energy corresponding to the sum of the individual gamma-ray energies. It is clear that the probability of finding a count in a particular energy interval of the sum spectrum is just the sum of the probabilities of all possible coincidences which have a total energy in that interval, where these latter probabilities are just determined by the individual response functions. Denoting the response function of a particular gamma ray as $\Psi_{\gamma_i}(E)$, we can express this as

$$\Psi_{\gamma_1 + \gamma_2}(E) = \sum_{E_i=0}^E \Psi_{\gamma_1}(E_i) \Psi_{\gamma_2}(E - E_i).$$

For the case of three or more coincident gamma rays, the extension of this is clear, e.g. for the case of three coincident gamma rays,

$$\Psi_{\gamma_1 + \gamma_2 + \gamma_3}(E) = \sum_{E_i=0}^E \Psi_{\gamma_1}(E_i) \sum_{E_j=0}^{E-E_i} \Psi_{\gamma_2}(E_j) \Psi_{\gamma_3}(E - E_i - E_j).$$

The Burroughs' 220 was programmed to carry out this summing for the case of two coincident gamma rays, the case encountered in the present experiment with the cascade transition.

From the calibration described on the preceding pages one can then interpolate the response function at any intermediate gamma-ray energy for a single gamma ray and produce the sum spectrum of the coincidence of any two such gamma rays. However, these response functions are normally limited to the high energy end of the spectra, $-1.20 \text{ MeV} \leq (E - E_{\gamma})$, because of the difficulties in obtaining calibration spectra which are anywhere near accurate over their whole extent due to such problems as (1) the tremendous increase in background at the low-energy end of the spectrum, (2) the frequent occurrence of strong, low-energy transitions arising from Coulomb excitation of the target backing, (3) the near impossibility of finding calibrations in which there are no other gamma rays in the spectrum either from contaminants or from the target itself, or (4) the scattering of photons by material such as shielding in the vicinity of the crystal. This practical limitation, however, is not a complete tragedy, as a knowledge of the spectrum in just the high-energy region is usually quite sufficient. For quantitative work, however, it will require additional knowledge as to what fraction of the total spectrum is in this high-energy region.

C. Photo-Fraction Measurements

As one can easily see, it turns out that actually the only part of the spectrum which is not effected by the presence of heavy shielding around the crystal is the full-energy peak, since only those quanta which leave their entire energy in the crystal can contribute to that peak. Hence, we must know the ratio, (ϕ_0) , of the counts in the full-energy peak, (Y_ϕ) , to the total number of counts in the response function, in

order to relate the full-energy peak to the number of gamma rays of that energy emitted by the source, (N_o).

$$Y_\phi / (\eta \cdot \phi_o) = N_o$$

To accomplish this the most difficult task is to obtain response functions, in the absence of all scattering material, from which the total number of counts in the spectrum due to the gamma ray can be determined reliably. This was achieved in the present experiment by removing all of the lead shielding and as much of the other material as possible from the vicinity of the crystal. The response functions of the crystal were then redetermined using the same reactions and the same techniques listed previously. The same problems were, of course, encountered in the low-energy region of these spectra, thus preventing an immediate determination of the total number of counts in the spectrum. The customary way of getting around this problem has been to use the spectrum as far back as possible and then use a horizontal extrapolation to zero-energy. Zerby and Moran (1961), however, have pointed out a more sensible way to approach the problem by calculating exactly the zero-intercept of the response function and using this point to interpolate the function through the region where it is distorted by the effects noted previously. The zero-intercept is subject to an exact calculation since the only events which can give rise to a count in that energy interval are events in which the incident gamma ray is scattered exactly forward giving up no energy to the crystal.

The "number-energy" distribution of Compton electrons (i.e. the Compton distribution in a NaI(Tl) spectrum) can be expressed as (Evans, 1955)

$$\frac{d\sigma}{dT} = \frac{d\sigma}{d\Omega} \frac{2\pi}{a^2 m_0 c^2} \left[\frac{(1+a)^2 - a^2 \cos^2 \phi}{(1+a)^2 - a(2+a)\cos^2 \phi} \right]^2$$

where

$$\frac{d\sigma}{d\Omega} = \frac{r_o^2}{2} \left(\frac{E'}{E_\gamma} \right)^2 \left(\frac{E'}{E_\gamma} + \frac{E'}{E_\gamma} - \sin^2 \theta \right)$$

and where

$$a = E_\gamma / m_0 c^2$$

E_γ is the initial gamma-ray energy,

E' is the scattered gamma-ray energy,

θ is the scattering angle of the photon, and

ϕ is the scattering angle of the electron.

As the energy transfer goes to zero, $\theta \rightarrow 0^\circ$; $\phi \rightarrow 90^\circ$, and it is clear that

$$\frac{d\sigma}{dT} \rightarrow \frac{2\pi r_o^2 m_0 c^2}{E_\gamma^2}$$

Since we are interested in the number of counts in a finite energy region we can integrate this over the zeroth channel of the analyzer, assuming $d\sigma/dT$ is roughly constant, to get

$$\sigma(0^{TH} \text{ channel}) = \frac{2\pi r_o^2 m_0 c^2}{E_\gamma^2} (\Delta E_{\text{channel}}).$$

The number of quanta incident on the crystal is given by

$$\frac{N_o}{4\pi} \int_0^{2\pi} d\phi \int_0^{\theta_o} d\theta \sin \theta.$$

Of these,

$$\frac{N_o}{4\pi} \int_0^{2\pi} d\phi \int_0^{\theta_o} d\theta e^{-\sigma\rho l(\theta)} \sin \theta$$

have no other interaction with the crystal. The number of available electrons/cm² in the crystal is just $N_e \cdot l(\theta)$ where N_e is the electron density. Therefore, the number of zero-energy interactions is given by

$$\frac{N_e N_o}{2} \left(2\pi \frac{r_o^2 m_o c^2}{E_\gamma^2} \right) (\Delta E_{\text{channel}}) \int_0^{\theta_o} l(\theta) e^{-\sigma\rho l(\theta)} \sin \theta d\theta,$$

and the fraction (f_o) of a response function in the last channel becomes

$$f_o = \frac{N_e \pi r_o^2 m_o c^2}{\eta E_\gamma^2} (\Delta E_{\text{channel}}) \int_0^{\theta_o} l(\theta) \sin \theta e^{-\sigma\rho l(\theta)} d\theta.$$

f_o was evaluated numerically on the Burroughs' 220 computer using the expressions for $l(\theta)$ listed previously. From f_o the zero intercept of a response function can be determined by a process of iterative integrations of the function.

With the zero-intercept determined, the total number of counts in the "free-crystal" response function can then be determined and thus the photo-fraction, ϕ_o . This was carried out for the crystals used in

this experiment and the resulting photo-fractions are shown graphically in Figures 10 and 14.

From the combination of these calculations of the efficiency (η) and the photo-fraction (ϕ_o) into the photo-efficiency ($\eta\phi_o$) together with the response-function calibration of the crystals, we are thus in a position, given a complex spectrum, to sort out the various gamma-ray contributions and from the area of their full-energy peaks determine the number of each of the gamma rays emitted from the target.

All of this sounds fine on paper and is in any event the most sensible way to approach the problem of determining absolute gamma-ray yields. In the present experiment, however, a serious difficulty was found in a comparison of the absolute determinations of the 3" x 3" solid and the 3" x 3" well crystals. This comparison indicated that the photo-efficiency of one of the crystals was off by approximately 15 to 20%, independent of gamma-ray energy. A check against other crystals indicated that the trouble was probably in the well crystal, and so the photo-efficiency of the well crystal was measured directly at one energy to check with the photo-efficiencies derived above.

This measurement was carried out at a gamma-ray energy of 1.277 MeV using a Na^{22} source. The source was placed in the well crystal and two 3" x 3" NaI(Tl) crystals placed on either side of the well crystal. A coincidence was then required between a 511 keV annihilation quantum in each of the 3" x 3" crystals, using the same type of fast-slow coincidence mixer described in Part III of the text. The well-crystal spectrum was stored in the multi-channel analyzer gated

by the coincidences of the two annihilation quanta. Background runs were made with the two 3" x 3" crystals at 90° to each other to remove real coincidences that were not double-annihilation coincidences. Random coincidences were removed using the singles spectrum. For every double-annihilation coincidence there was a possibility (just the photo-efficiency) of there being a count stored in the multi-channel analyzer in the full-energy peak of the 1.277 MeV gamma ray spectrum. The photo-efficiency ($\eta\phi_0$) is thus just the ratio of full-energy counts to double-annihilation coincidences. This measurement gave

$$\eta\phi_0(1.277 \text{ MeV}) = 0.167 \pm 0.001.$$

This, compared to the value of 0.144 determined for $\eta\phi_0$ by a calculation of η and a measurement of ϕ_0 as described previously, shows just the expected discrepancy of 16.1% in the proper direction to make the two crystals now agree in their absolute determinations. No explanation for this discrepancy with the well crystal has been found. The measured point, corrected upwards to ($\eta_0\phi_0 = 0.172$) is plotted in Figure 14 and a line drawn through it parallel to the other $\eta_0\phi_0$ line indicating a 16.1% correction applied uniformly at all energies, in line with the fact that this discrepancy was observed to be independent of gamma-ray energy.

Thus, in conclusion, it can be said that with the techniques described in this appendix each of the crystals used in the experiment described in the body of this thesis was calibrated so that complex spectra could be sorted out, and so that from the full-energy peaks of the resulting

components the absolute number of gamma decays occurring in the target could be determined.

REFERENCES

- J. N. Bahcall, 1962, Phys. Rev. 128, 1297.
- J. N. Bahcall, W. A. Fowler, I. Iben and R. L. Sears, 1963, Ap. J. (to be published).
- S. Bashkin, R. W. Kavanagh and P. D. Parker, 1959, Phys. Rev. Letts., 3, 518.
- N. Bohr, 1915, Phil. Mag. 30, 581.
- R. E. Brown, 1962, Ph.D. Thesis, California Institute of Technology.
- E. M. Burbidge, G. R. Burbidge, W. A. Fowler and F. Hoyle, 1957, Rev. Modern Phys. 29, 547.
- A. G. W. Cameron, 1957, Report No. AECL/454.
- H. M. Childers, 1959, Rev. Sci. Instr. 30, 810.
- R. F. Christy and I. Duck, 1961, Nuclear Physics 24, 89.
- R. D. Evans, 1955, The Atomic Nucleus (McGraw-Hill Book Co., Inc., New York, N.Y.), Chapters 23, 24, and 25, pages 672 ff.
- W. A. Fowler, 1958, Ap. J. 127, 551.
- W. A. Fowler, 1960, Memoires Soc. Roy. Science de Liege Series 5, 3, 207.
- W. A. Fowler, 1962, private communication.
- G. M. Griffiths, 1959, private communication.
- G. M. Griffiths, R. A. Morrow, P. J. Riley and J. B. Warren, 1961, Can. J. Phys. 39, 1397.
- G. W. Grodstein, 1957, N.B.S. Circular 583.
- Harshaw Chemical Co., 1962, Scintillation Phosphors (2nd edition).
- R. L. Heath, 1962, U.S. AEC Report IDO-16784.
- R. Hofstadter, 1957, Ann. Rev. Nuc. Sci., 7, 231.
- H. D. Holmgren and R. L. Johnston, 1959, Phys. Rev. 113, 1556.

- C. M. Jones, A. C. L. Barnard and G. C. Phillips, 1962, private communication.
- R. W. Kavanagh, 1960, Nuclear Physics 15, 411.
- T. Lauritsen and F. Ajzenberg-Selove, 1962, Nuclear Data Sheets, Sets 5 and 6, 1961 (National Academy of Sciences-National Research Council; Washington D.C.).
- H. Margenau and G. M. Murphy, 1956, The Mathematics of Physics and Chemistry (D. Van Nostrand Co., Inc., Princeton, N.J.), Chapter 13, pages 467 ff.
- P. D. Miller and G. C. Phillips, 1958, Phys. Rev. 112, 2048.
- J. F. Mollenauer, 1961, Report No. UCRL-9748.
- S. A. Moszkowski, 1955, "Theory of Multipole Radiation," in K. Siegbahn, Editor, Beta- and Gamma-Ray Spectroscopy, Chapter 13, pages 373 ff.
- K. Okano, 1960, J. Phys. Soc. Japan 15, 28.
- J. D. Pearson, 1963, Ph.D. Thesis, California Institute of Technology.
- L. P. Robertson, B. L. White and K. L. Erdman, 1961, Rev. Sci. Instr., 32, 1405.
- M. E. Rose, 1953, Phys. Rev. 91, 610.
- L. Salmon, 1961, Nuc. Instr. and Methods 14, 193.
- E. E. Salpeter, 1952, Phys. Rev. 88, 547.
- R. H. Spear, J. D. Larson and J. D. Pearson, 1962, Nuclear Physics (to be published).
- T. A. Tombrello and G. C. Phillips, 1961, Phys. Rev. 122, 224.
- T. A. Tombrello and P. D. Parker, 1962, Phys. Rev. (to be published).
- T. A. Tombrello and P. D. Parker, 1962a, Phys. Rev. (to be published).
- A. Tubis, 1957, LASL Report No. LA-2150.
- H. A. Weidenmüller, 1962, Theoretical Nuclear Physics, (unpublished lecture notes).
- H. I. West, Jr. and B. Johnston, 1960, IRE Trans. Nuc. Sci. NS-7, 111.

W. Whaling, 1958, Handbuch der Physik 34, 193.

H. H. Woodbury, 1953, Ph. D. Thesis, California Institute of Technology.

C. D. Zerby and H. S. Moran, 1961, Report No. ORNL-3169.

TABLE I: Experimental Total Cross Sections (σ_{Total}) and Cross-Section Factors ($S(E)$) for $\text{He}^3(a, \gamma)\text{Be}^7$ as a Function of the Center-of-Mass Energy (E_{cm}).

The total cross sections are derived from the gamma-ray spectra as described in Part IV (A). The last column notes the method of analysis used in each case: "L.S." → least-squares analysis, see page 36, "F.E." → analysis of only the full-energy peak, see page 42, and "Int." → analysis of the integrated spectrum, see page 42. See text page 54 and Figure 21.

$S(E)$ is the cross-section factor defined by Burbidge et al. (1957). See text page 59 and Figure 25.

TABLE I

E_{cm} (keV)	σ_{Total} (μ -Barns)	$S(E_{cm})$ (keV-Barns)	Notes
181 ± 20	0.018 ± 0.007	0.631 ± 0.432	F.E.
280 ± 20	0.092 ± 0.014	0.459 ± 0.145	F.E.
290 ± 20	0.101 ± 0.013	0.440 ± 0.129	F.E.
370 ± 19	0.205 ± 0.027	0.378 ± 0.080	Int.
384 ± 19	0.247 ± 0.032	0.404 ± 0.084	Int.
407 ± 19	0.282 ± 0.031	0.385 ± 0.069	Int.
407 ± 19	0.324 ± 0.045	0.442 ± 0.088	Int.
415 ± 19	0.322 ± 0.027	0.414 ± 0.071	F.E.
486 ± 23	0.415 ± 0.044	0.340 ± 0.056	L.S.
515 ± 19	0.546 ± 0.058	0.383 ± 0.055	L.S.
523 ± 19	0.587 ± 0.059	0.396 ± 0.054	L.S.
545 ± 20	0.589 ± 0.048	0.358 ± 0.049	F.E.
595 ± 22	0.732 ± 0.073	0.359 ± 0.048	L.S.
596 ± 22	0.690 ± 0.071	0.337 ± 0.046	L.S.
600 ± 22	0.761 ± 0.070	0.366 ± 0.048	L.S.
625 ± 23	0.814 ± 0.066	0.356 ± 0.046	F.E.
708 ± 22	1.009 ± 0.078	0.337 ± 0.040	F.E.
708 ± 31	0.904 ± 0.081	0.302 ± 0.041	L.S.
713 ± 26	0.962 ± 0.077	0.316 ± 0.040	F.E.
747 ± 24	1.007 ± 0.092	0.301 ± 0.036	L.S.
753 ± 25	0.971 ± 0.089	0.286 ± 0.034	L.S.
795 ± 23	1.145 ± 0.104	0.303 ± 0.034	L.S.
803 ± 26	1.209 ± 0.094	0.314 ± 0.037	F.E.
804 ± 23	1.017 ± 0.094	0.264 ± 0.030	L.S.
838 ± 37	1.164 ± 0.101	0.279 ± 0.036	L.S.
868 ± 29	1.299 ± 0.113	0.293 ± 0.034	L.S.
898 ± 32	1.453 ± 0.110	0.308 ± 0.036	F.E.
923 ± 28	1.286 ± 0.113	0.260 ± 0.029	L.S.
924 ± 28	1.362 ± 0.119	0.275 ± 0.031	L.S.
955 ± 34	1.302 ± 0.125	0.249 ± 0.029	L.S.

TABLE I (Cont.)

E_{cm} (keV)	σ_{Total} (μ -Barns)	$S(E_{cm})$ (keV-Barns)	Notes
1038 \pm 33	1.706 \pm 0.148	0.286 \pm 0.032	L. S.
1041 \pm 30	1.744 \pm 0.133	0.291 \pm 0.032	F. E.
1093 \pm 32	1.530 \pm 0.134	0.237 \pm 0.026	F. E.
1138 \pm 28	1.965 \pm 0.150	0.287 \pm 0.030	F. E.
1141 \pm 31	1.805 \pm 0.156	0.263 \pm 0.028	L. S.
1145 \pm 31	1.709 \pm 0.147	0.248 \pm 0.027	L. S.
1243 \pm 30	2.057 \pm 0.175	0.266 \pm 0.028	L. S.
1243 \pm 30	1.684 \pm 0.148	0.218 \pm 0.023	F. E.
1248 \pm 30	1.768 \pm 0.153	0.228 \pm 0.024	L. S.
1248 \pm 30	1.984 \pm 0.171	0.255 \pm 0.027	L. S.
1340 \pm 28	1.814 \pm 0.157	0.213 \pm 0.022	F. E.
1343 \pm 28	2.009 \pm 0.174	0.235 \pm 0.024	L. S.
1343 \pm 26	2.596 \pm 0.197	0.304 \pm 0.031	F. E.
1353 \pm 29	2.201 \pm 0.188	0.256 \pm 0.026	L. S.
1553 \pm 24	3.035 \pm 0.231	0.301 \pm 0.031	F. E.
1618 \pm 26	2.810 \pm 0.245	0.267 \pm 0.027	F. E.
1638 \pm 26	2.813 \pm 0.244	0.264 \pm 0.027	F. E.
2096 \pm 23	3.717 \pm 0.324	0.279 \pm 0.028	F. E.
2111 \pm 23	3.427 \pm 0.308	0.256 \pm 0.026	F. E.
2113 \pm 23	3.787 \pm 0.329	0.282 \pm 0.028	F. E.
2143 \pm 23	3.767 \pm 0.327	0.278 \pm 0.028	F. E.
2493 \pm 22	3.903 \pm 0.508	0.259 \pm 0.034	F. E.

Coincident Measurement:

$$E_{cm} = 1378 \pm 29 \text{ keV}$$

$$\sigma(\gamma_2) = 0.684 \pm 0.062 \text{ } \mu\text{-barns} \rightarrow \sigma_{Total} = 2.507 \pm 0.355 \text{ } \mu\text{-barns}$$

TABLE II: Elastic-Scattering Phase Shifts Used in the Theoretical Calculations

These phase shifts were taken from the $\text{He}^4(\text{He}^3, \text{He}^3)\text{He}^4$ elastic-scattering experiments. (Miller and Phillips, 1958; Jones et al., 1962; Tombrello and Parker, 1962).

The s-wave and d-wave phase shifts, δ_0 and δ_2^\pm , are taken to be just the respective hard-sphere phase shifts for $R_0 = 2.80$ fm, in agreement with these experiments.

The two p-wave phase shifts, δ_1^+ and δ_1^- , are taken from the experiments down to $E_{\text{cm}} = 12.67$ keV. At that point the p-wave, hard-sphere phase shift was normalized to each of these experimental values and used to give the values of δ_1^+ and δ_1^- at lower energies.

The two f-wave phase shifts, δ_3^+ and δ_3^- , are governed by the two $\ell = 3$ resonances just above the region of this experiment. The values used were taken from the experiments listed above.

See text pages 10 and 57.

TABLE II
 E_{cm}
 δ_0
 δ_1^-
 δ_1^+
 δ_2^\pm
 δ_3^-
 δ_3^+
(Degrees)

86	-0. 3839 x 10 ⁻⁴	-0. 1175 x 10 ⁻⁴	-0. 2520 x 10 ⁻⁴	-0. 2865 x 10 ⁻⁵	0. 0000	0. 0000		
171	-0. 6639 x 10 ⁻³	-0. 1250 x 10 ⁻²	-0. 2680 x 10 ⁻²	-0. 4584 x 10 ⁻⁵	0. 0000	0. 0000		
257	-0. 6378 x 10 ⁻¹	-0. 1350 x 10 ⁻¹	-0. 2880 x 10 ⁻¹	-0. 5443 x 10 ⁻⁴	0. 0000	0. 0000		
343	-0. 2413	-0. 5700 x 10 ⁻¹	-0. 1220	-0. 2687 x 10 ⁻³	0. 0000	0. 0000		
429	-0. 5894	-0. 1540	-0. 3290	-0. 8594 x 10 ⁻³	0. 0000	0. 0000		
514	-1. 1264	-0. 3240	-0. 6940	-0. 2088 x 10 ⁻²	0. 0000	0. 0000		
600	-1. 8444	-0. 5810	-1. 250	-0. 4257 x 10 ⁻²	0. 0000	0. 0000		
686	-2. 726	-0. 9370	-2. 010	-0. 7691 x 10 ⁻²	0. 0000	0. 0000		
771	-3. 744	-1. 390	-2. 980	-0. 1273 x 10 ⁻¹	0. 0000	0. 0000		
857	-4. 877	-1. 960	-4. 19	-0. 1970 x 10 ⁻¹	0. 0000	0. 0000		
1071	-8. 059	-3. 82	-8. 17	-0. 4766 x 10 ⁻¹	0. 0000	0. 0000		
1286	-11. 539	-6. 30	-13. 50	-0. 9442 x 10 ⁻¹	0. 0000	+1. 000		
1500	-15. 15	-7. 70	-16. 10	-0. 1640	0. 0000	+1. 750		
1714	-18. 79	-9. 30	-17. 50	-0. 2599	+0. 250	+2. 50		
1929	-22. 39	-11. 20	-19. 00	-0. 3846	+0. 500	+3. 70		
2143	-25. 94	-13. 00	-21. 10	-0. 5401	+0. 750	+5. 00		
2571	-32. 79	-18. 00	-24. 10	-0. 9488	+2. 50	+10. 00		

FIGURE 1: Energy Level Diagram of Be⁷ (Lauritsen, 1962)

This diagram indicates the Q-values involved in the present experiment as well as the locations, spins and parities of the levels referred to in the text. The gamma transitions referred to in the text as γ_1 , γ_2 and γ_3 are labelled.

See text pages 31 and 35.

FIGURE I

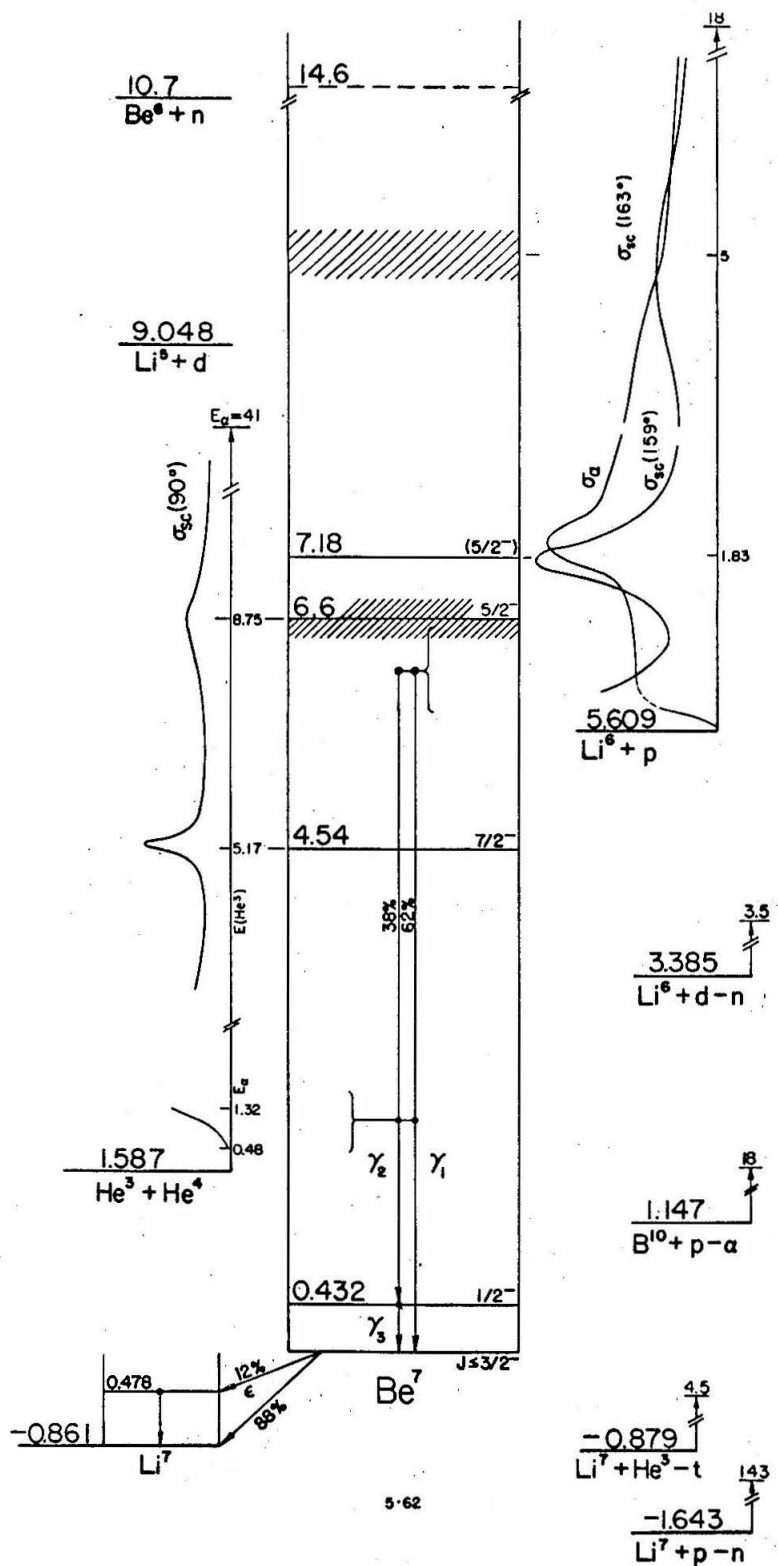


FIGURE 2: Target Assembly and Associated Beam Tube

This is a scale drawing of the beam-tube construction immediately in front of the target assembly, indicating the locations of the liquid-nitrogen cold trap, the ion gauge, the pumping lines and the gas target assembly. (See Figure 3 for details of the target assembly.) Points (A) and (B) are connected to the corresponding points in Figure 4.

See text page 16.

FIGURE 2

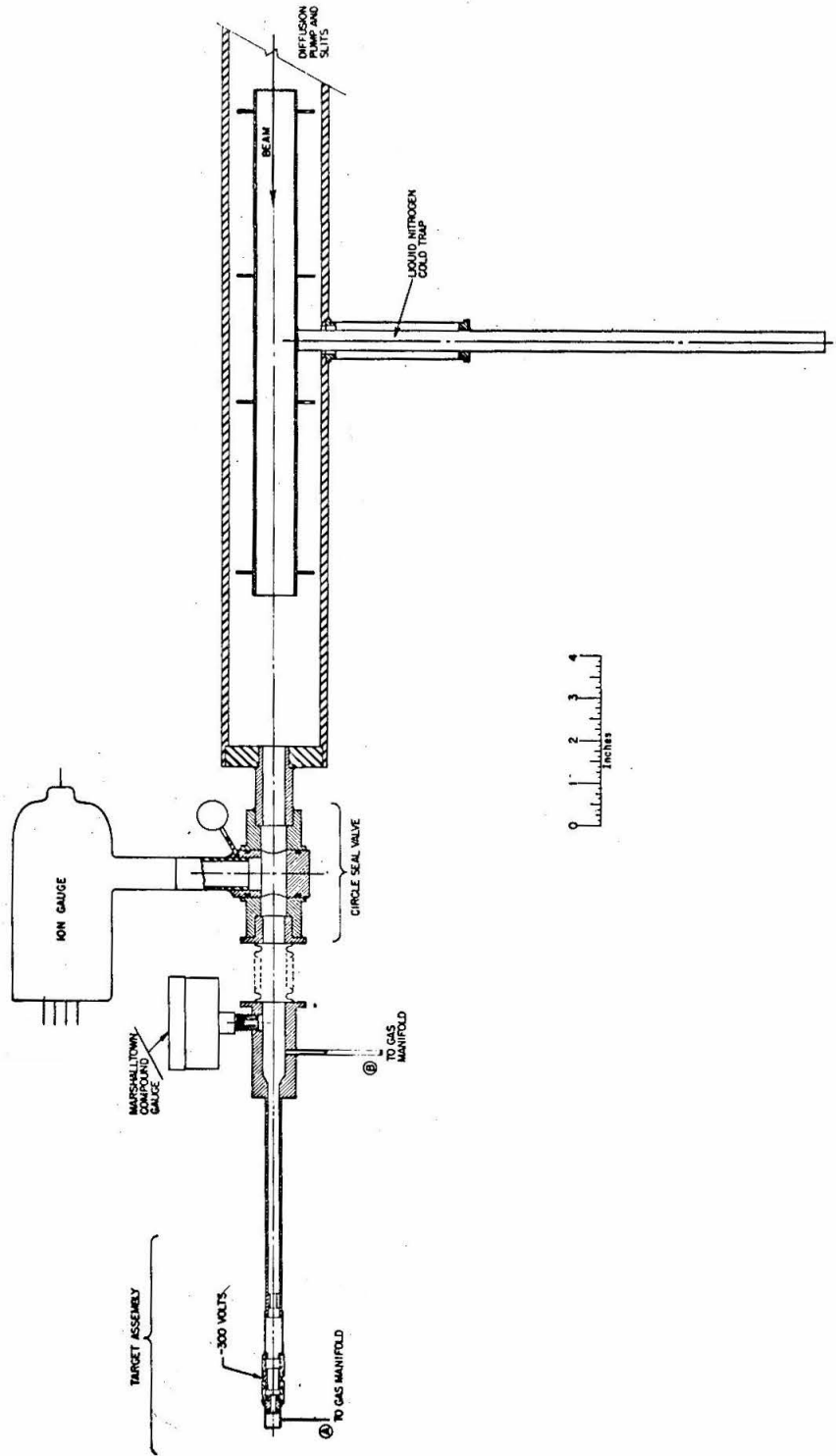


FIGURE 3: Target Assembly

This scale drawing indicates the locations of the beam-defining apertures, the electron suppressor, the foil holder and the entrance foil, as well as the details of the gas target chamber. Point  is connected to the corresponding point in Figure 4.

See text page 16.

FIGURE 3

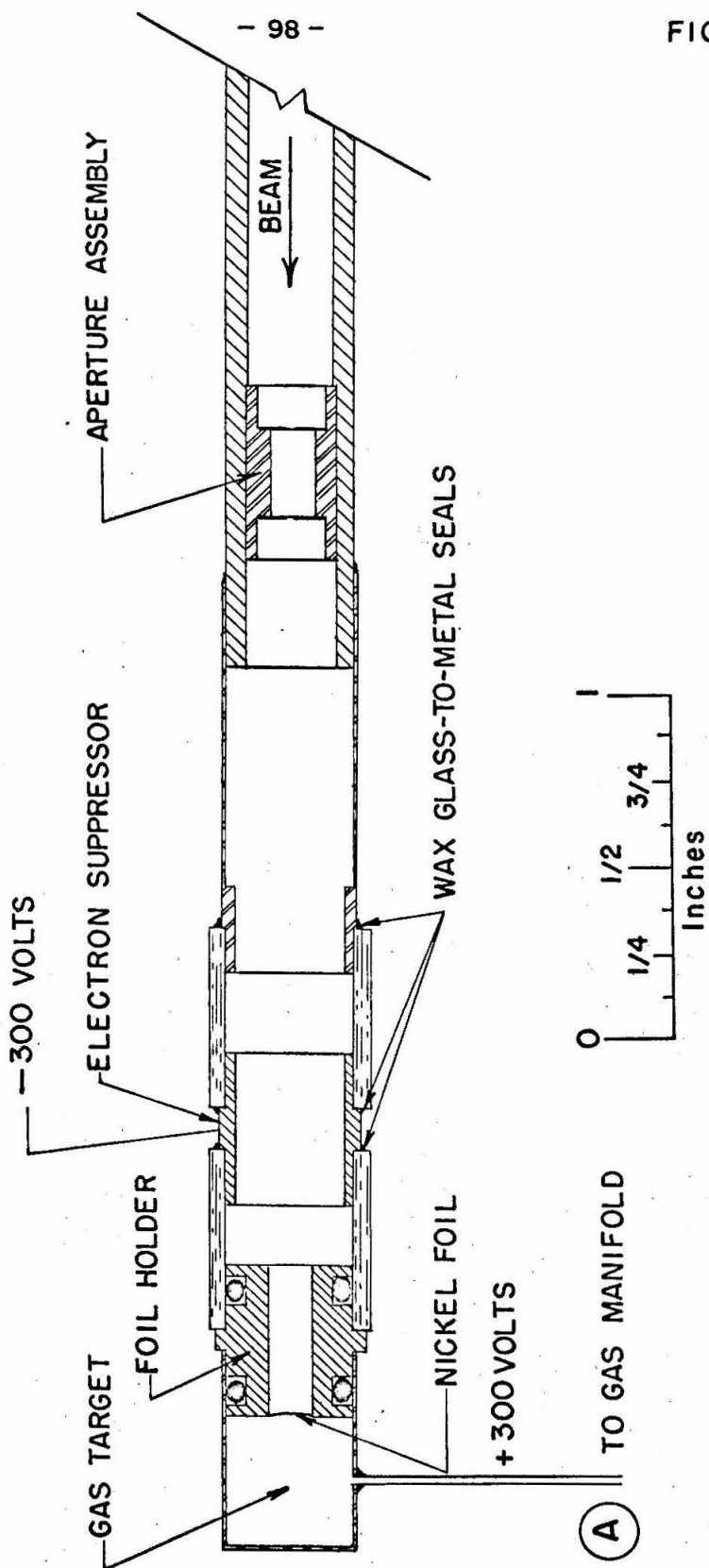


FIGURE 4: Gas Manifold

This is a schematic representation of the manifold system used for filling the target with the appropriate gas and measuring the gas pressure in the target. Points (A) and (B) are connected to the corresponding points in Figures 2 and 3. (X)'s mark the location of Hoke needle valves.

See text page 19.

FIGURE 4

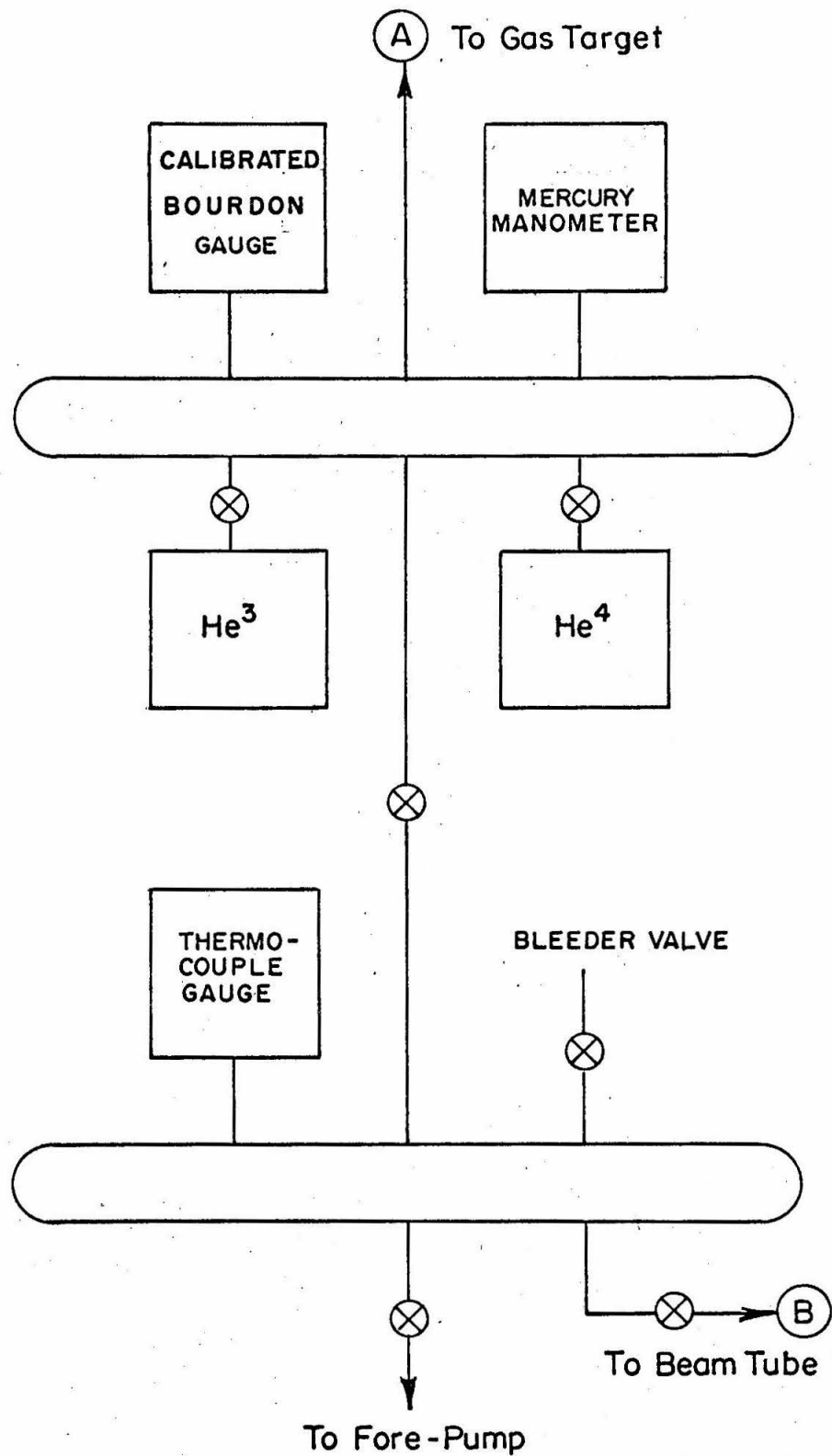
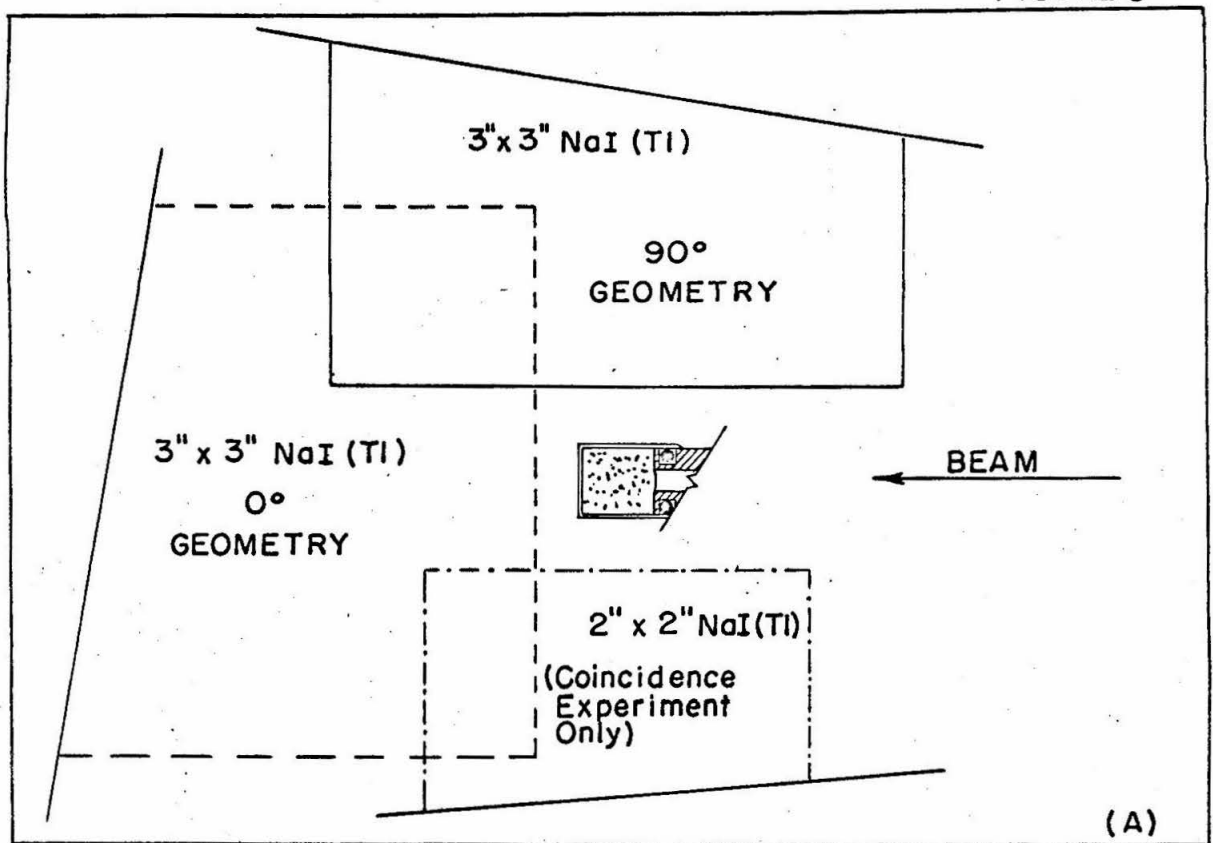


FIGURE 5: Target-Detector Geometry

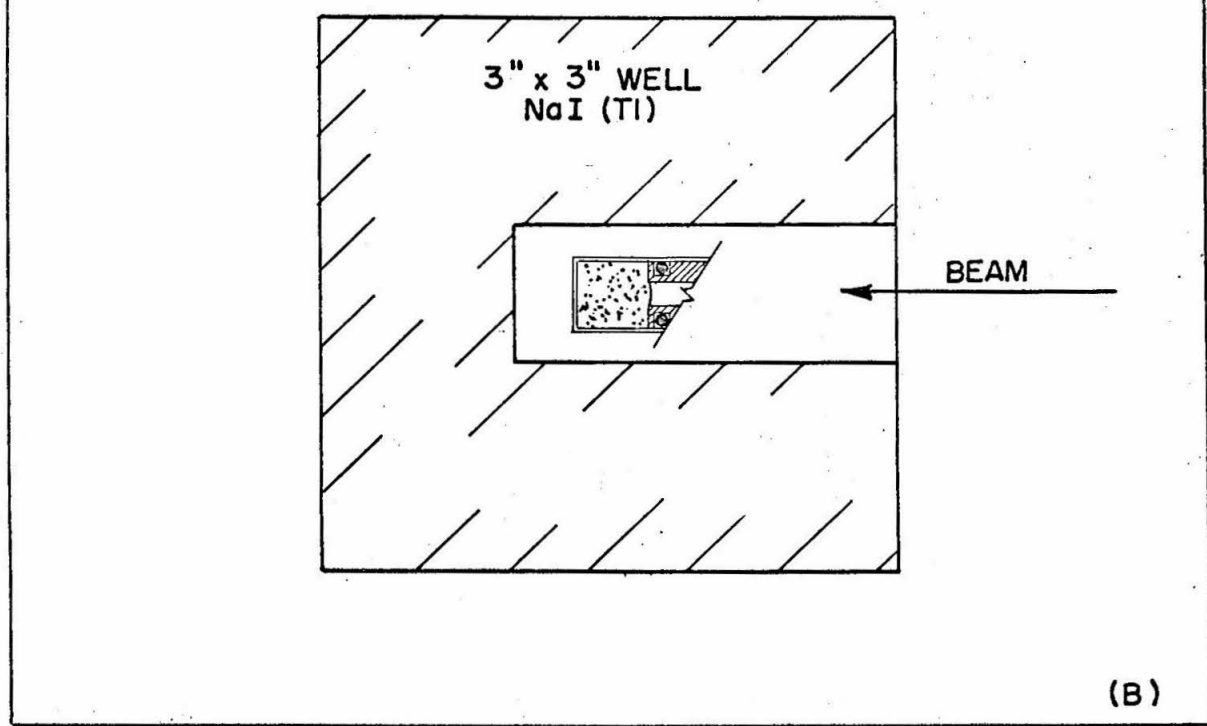
In (A) the target-detector geometry of the 3" x 3" NaI(Tl) is indicated for the runs made at 0° and 90°. The location of the 2" x 2" crystal used for the coincidence run with the 3" x 3" crystal at 90° is also shown. See text pages 23, 28, 31 and 72.

In (B) the target-detector geometry is shown for the well crystal. See text pages 23 and 28.

FIGURE 5



(A)



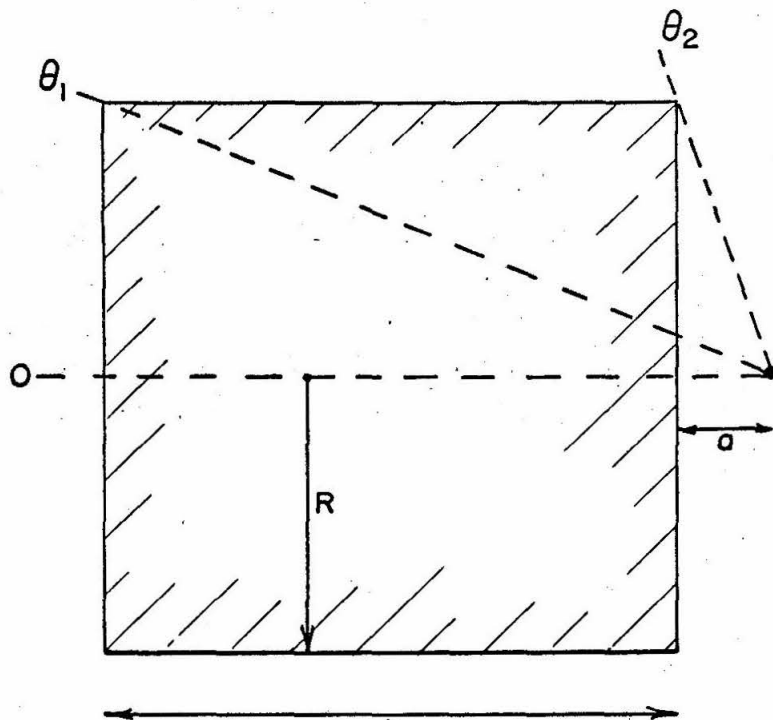
(B)

FIGURE 6: NaI(Tl) Scintillators

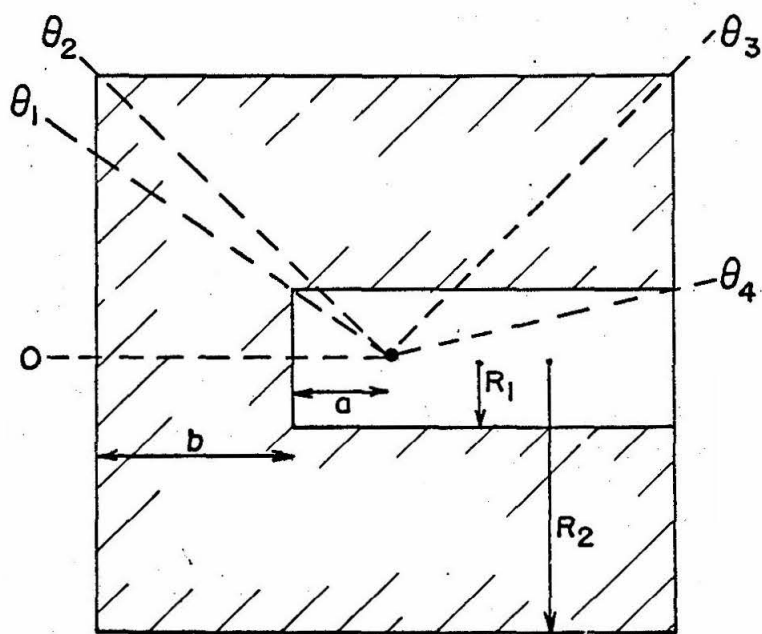
These figures define the parameters used in the calculation of the total efficiency (η_0) for the solid crystals (A) and for the well crystal (B). The symmetry axis of these cylindrical crystals is defined as 0.

See text pages 71 and 72.

FIGURE 6



(A)



(B)

FIGURE 7: 2" x 2" NaI(Tl) Efficiencies

The total efficiency (η_0) for a .2" x 2" NaI(Tl) solid, cylindrical crystal is plotted as a function of gamma-ray energy (E_γ) for an isotropic radiation pattern from a point source. The source was located on the axis of the crystal at a distance "a". (Figure 6A) from the front face, where curves are indicated for values of "a" ranging from 1/4" to 3/4" in 1/8" steps.

See text page 48 and 72.

FIGURE 7

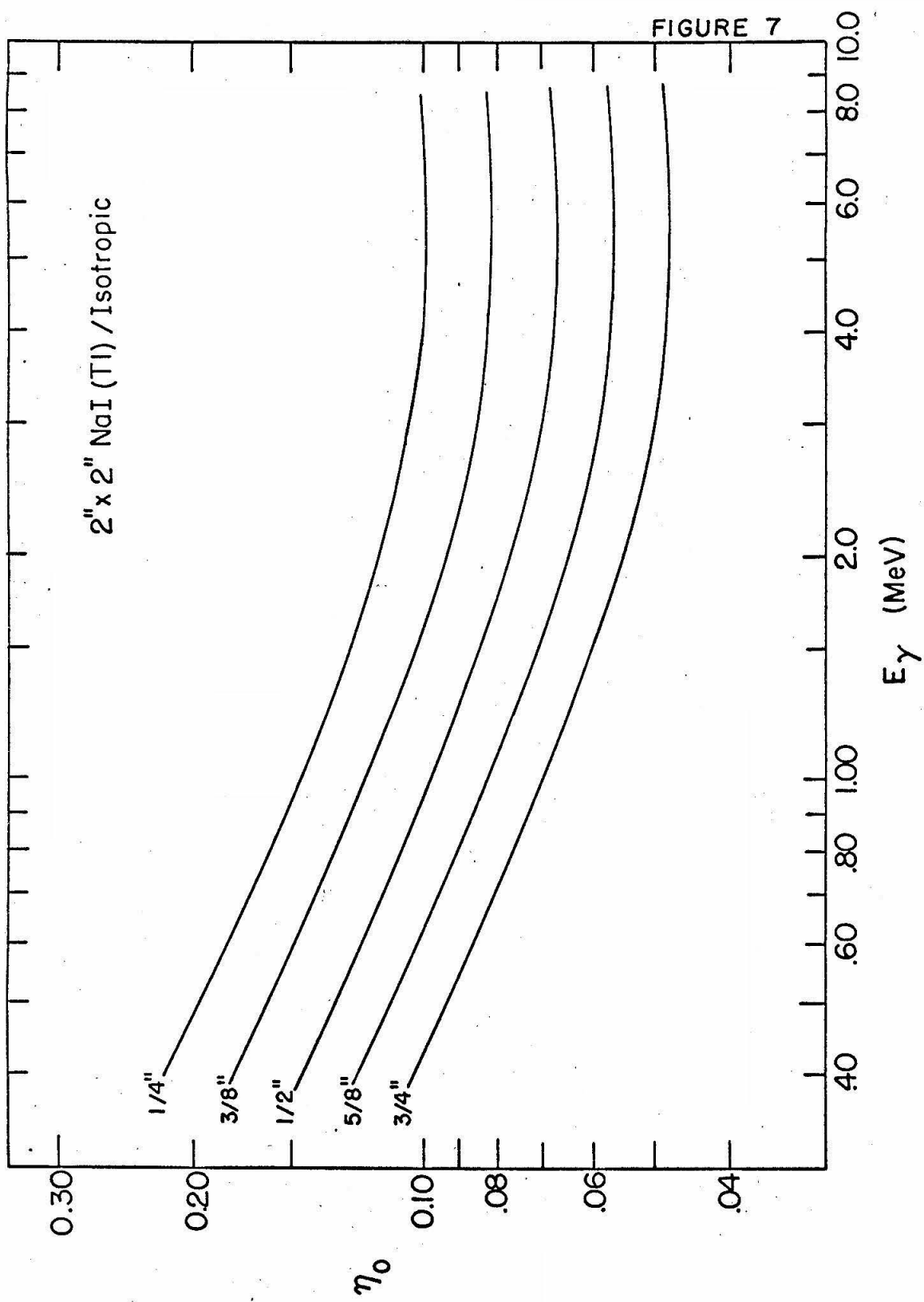


FIGURE 8: 2" x 2" NaI(Tl) Efficiencies

The total efficiency (η_0) for a 2" x 2" NaI(Tl) solid, cylindrical crystal is plotted as a function of gamma-ray energy (E_γ) for $a \sin^2 \theta$ radiation pattern from a point source with the crystal axis at $\theta = 0^\circ$. The source is located on the axis of the crystal at a distance "a" (Figure 6A) from the front face, where curves are indicated for values of "a" ranging from 1/4" to 3/4" in 1/8" steps.

See text pages 48 and 72.

FIGURE 8

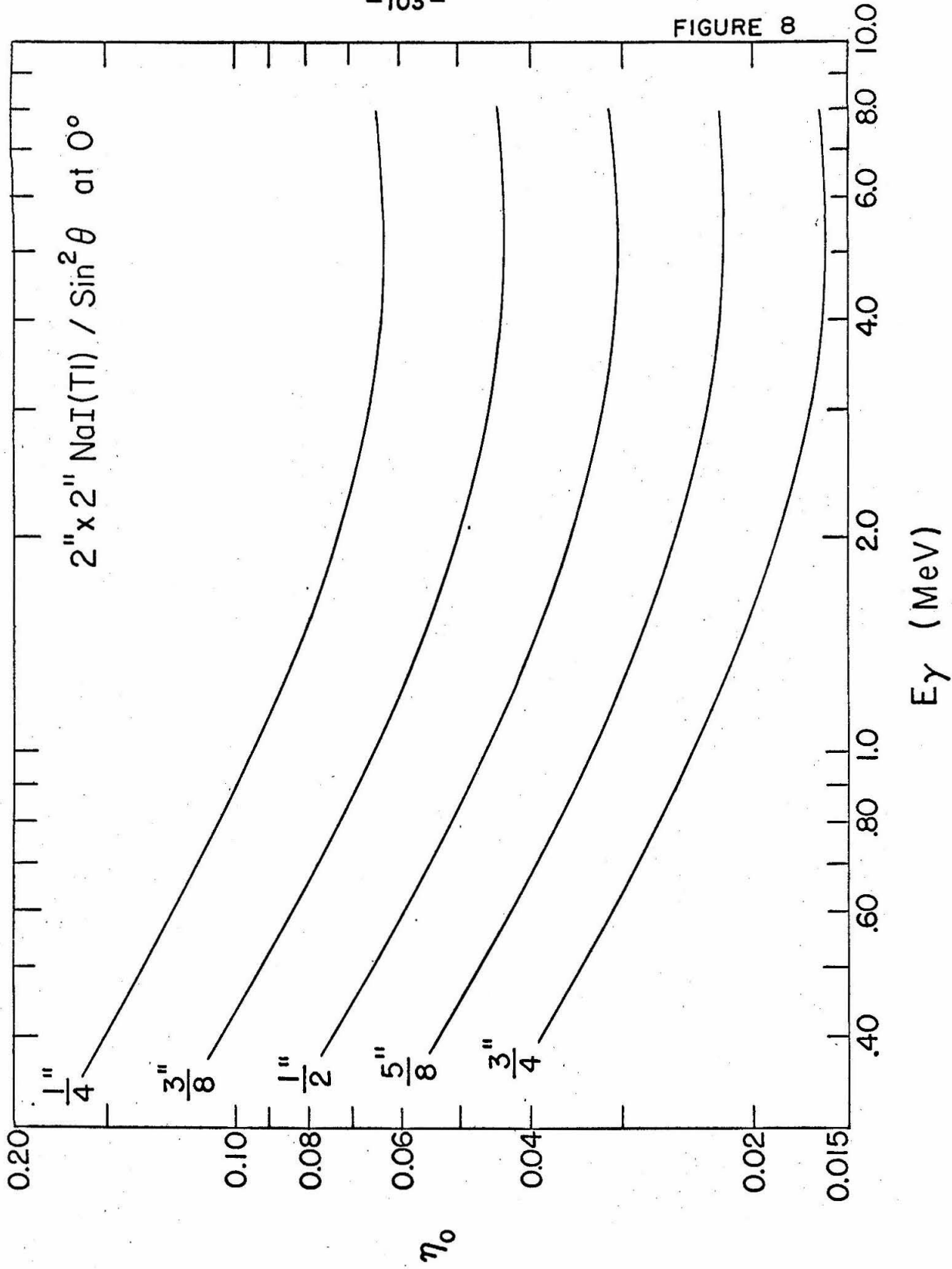


FIGURE 9: 2" x 2" NaI(Tl) Efficiencies

The total efficiency (η_0) for a 2" x 2" NaI(Tl) solid, cylindrical crystal is plotted as a function of gamma-ray energy (E_γ) for a $\sin^2 \theta$ radiation pattern from a point source with the crystal axis at $\theta = 90^\circ$. The source was located on the axis of the crystal at a distance "a" (Figure 6A) from the front face, where curves are indicated for values of "a" ranging from 1/4" to 3/4" in 1/8" steps.

See text pages 48 and 72.

FIGURE 9

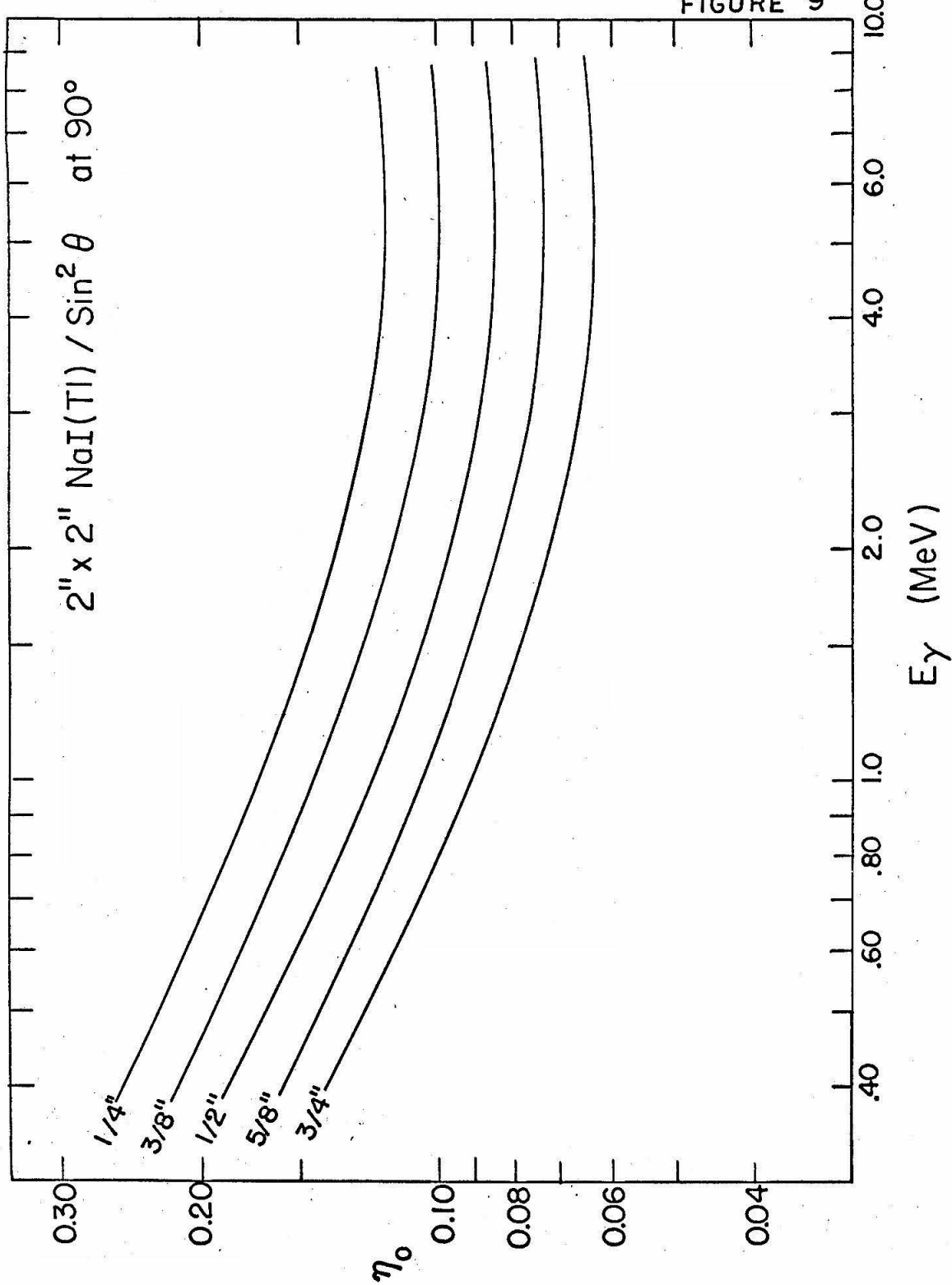


FIGURE 10: Photo-Fraction for 3" x 3" NaI(Tl) Crystal

The experimentally determined photo-fractions are plotted for the 3" x 3" NaI(Tl) crystal as a function of gamma-ray energy, and a smooth curve drawn through the points for interpolation. These measurements were made with the crystal completely unshielded and approximately 7/16" from the target spot at 90° to the incident beam.

See text page 87.

FIGURE 10

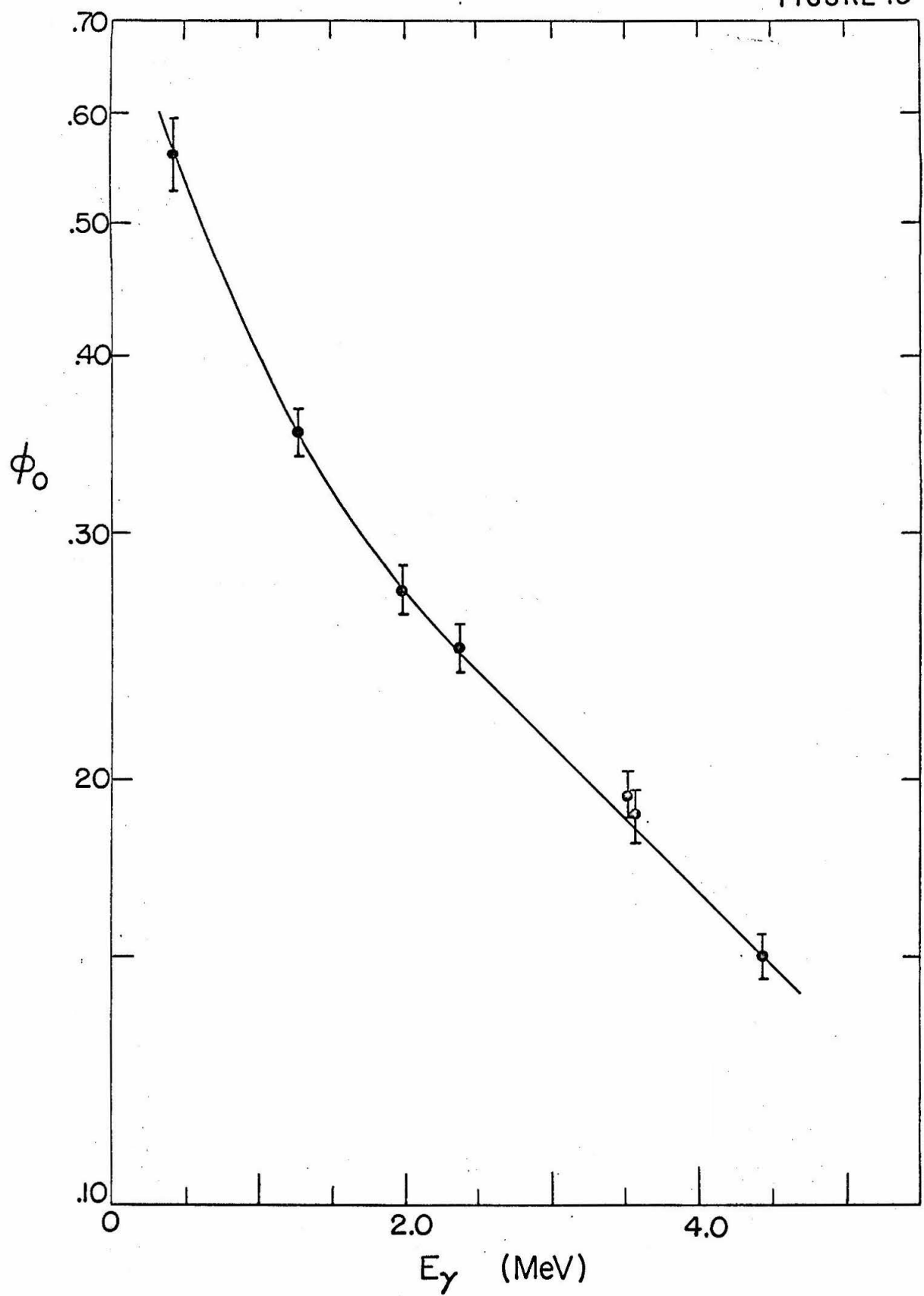


FIGURE 11: 3" x 3" NaI(Tl) Efficiencies

The total efficiency (η_0) for a 3" x 3" NaI(Tl) solid, cylindrical crystal is plotted as a function of gamma-ray energy (E_γ) for an isotropic radiation pattern from a point source.

The source was located on the axis of the crystal at a distance "a" (Figure 6A) from the front face, where curves are indicated for values of "a" ranging from 1/8" to 3/4" in 1/8" steps.

See text pages 48 and 72.

FIGURE II

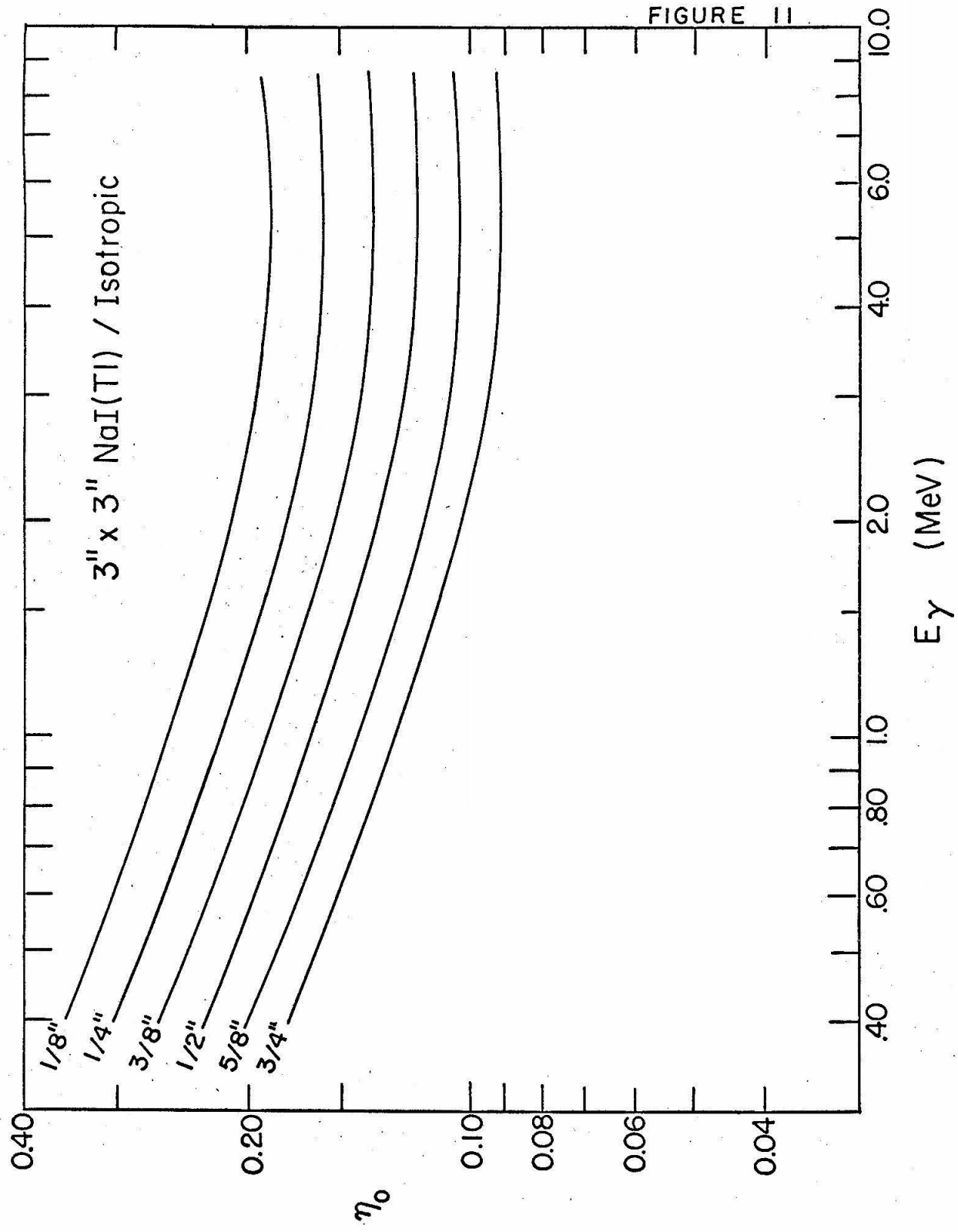


FIGURE 12: 3" x 3" NaI(Tl) Efficiencies

The total efficiency (η_o) for a 3" x 3" NaI(Tl) solid, cylindrical crystal is plotted as a function of gamma-ray energy (E_Y) for a $\sin^2\theta$ radiation pattern from a point source with the crystal axis at $\theta = 0^\circ$. The source was located on the axis of the crystal at a distance "a" (Figure 6A) from the front face, where curves are indicated for values of "a" ranging from 1/8" to 3/4" in 1/8" steps.

See text pages 48 and 72.

FIGURE 12

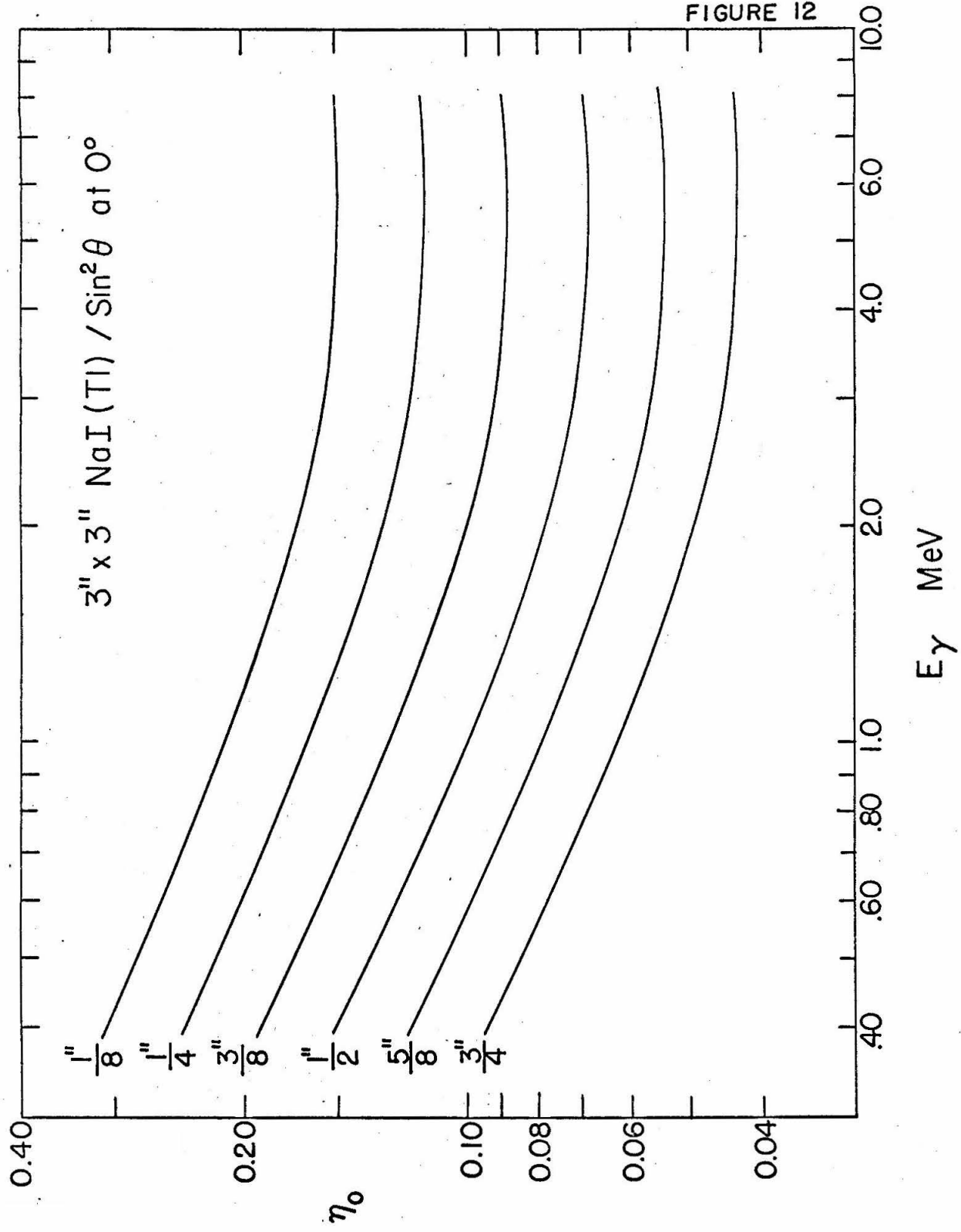


FIGURE 13: 3" x 3" NaI(Tl) Efficiencies

The total efficiency (η_o) for a 3" x 3" NaI(Tl) solid, cylindrical crystal is plotted as a function of gamma-ray energy (E_γ) for a $\sin^2 \theta$ radiation pattern from a point source with the crystal axis at $\theta = 90^\circ$. The source was located on the axis of the crystal at a distance "a" (Figure 6A) from the front face, where curves are indicated for values of "a" ranging from 1/8" to 3/4" in 1/8" steps.

See text pages 48 and 72.

FIGURE 13

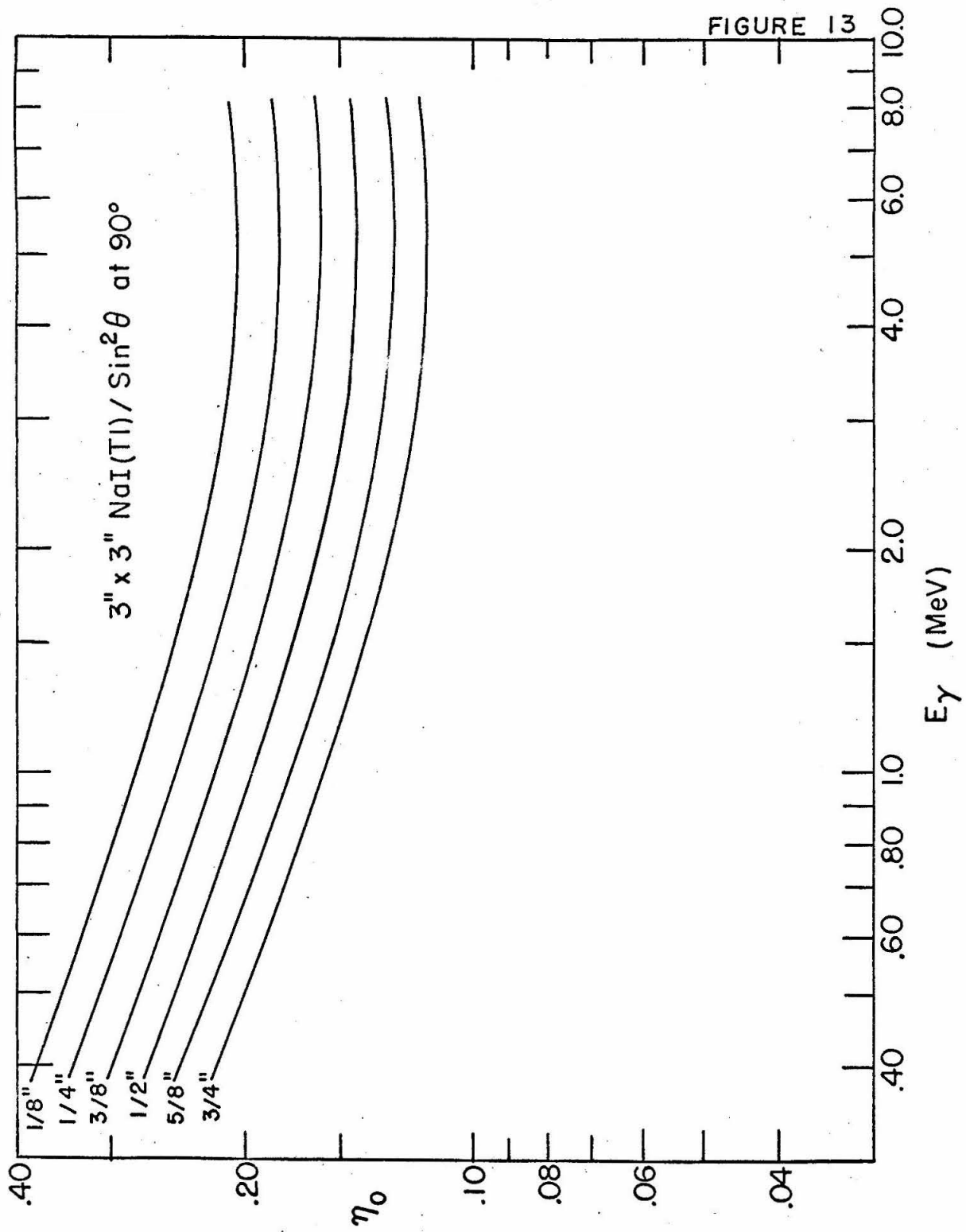


FIGURE 14: Detection Properties of the 3" x 3" Well NaI(Tl) Crystal

The following properties were determined as a function of gamma-ray energy (E_γ) for a 3" x 3" cylindrical NaI(Tl) crystal with a 3/4" diameter by 2" deep well along its axis and with a point source located at the center of the crystal (Figure 6B):

- (a) The total efficiency for point sources with isotropic or $\sin^2\theta$ radiation patterns.

See text pages 48 and 72.

- (b) The photo-fraction measured with the crystal completely unshielded. See text page 87.
(c) The photo-efficiency for isotropic radiation, determined as a product of the appropriate curves in (a) and (b). See text page 88.
(d) The photo-efficiency for isotropic radiation determined experimentally at 1.277 MeV (indicated by the circled point) and extrapolated parallel to the curve in section (c).
See text page 88.

FIGURE 14

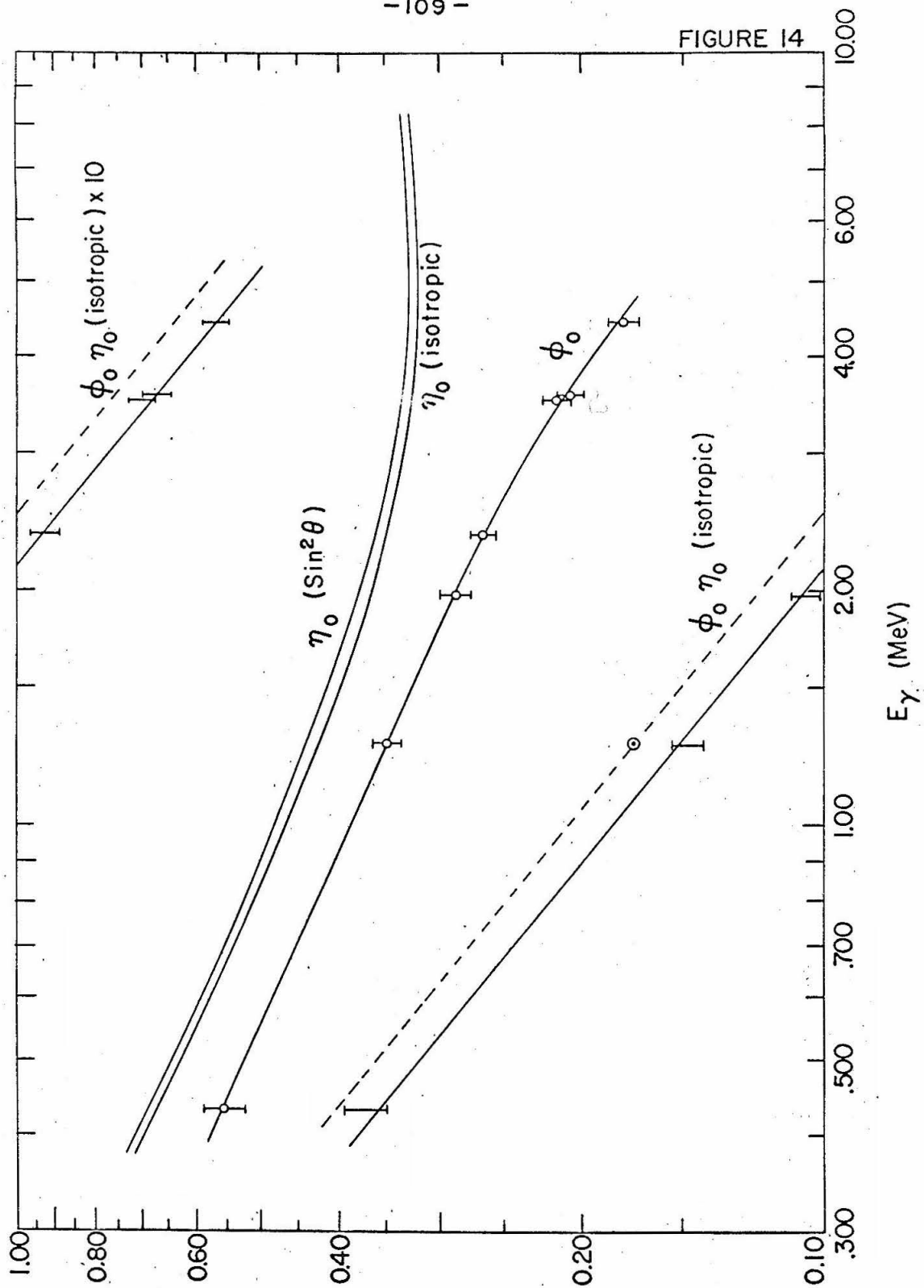


FIGURE 15: Response Functions for a Heavily Shielded 3" x 3" NaI(Tl) Crystal

These response functions, normalized to 1.000 at the full-energy peak, were obtained with the NaI(Tl) crystal heavily shielded and were used with interpolation to unfold the various components on the complex experimental spectra. The gamma-ray energy is indicated at the low energy end of each function.

See text pages 74, 78 and 81.

FIGURE 15

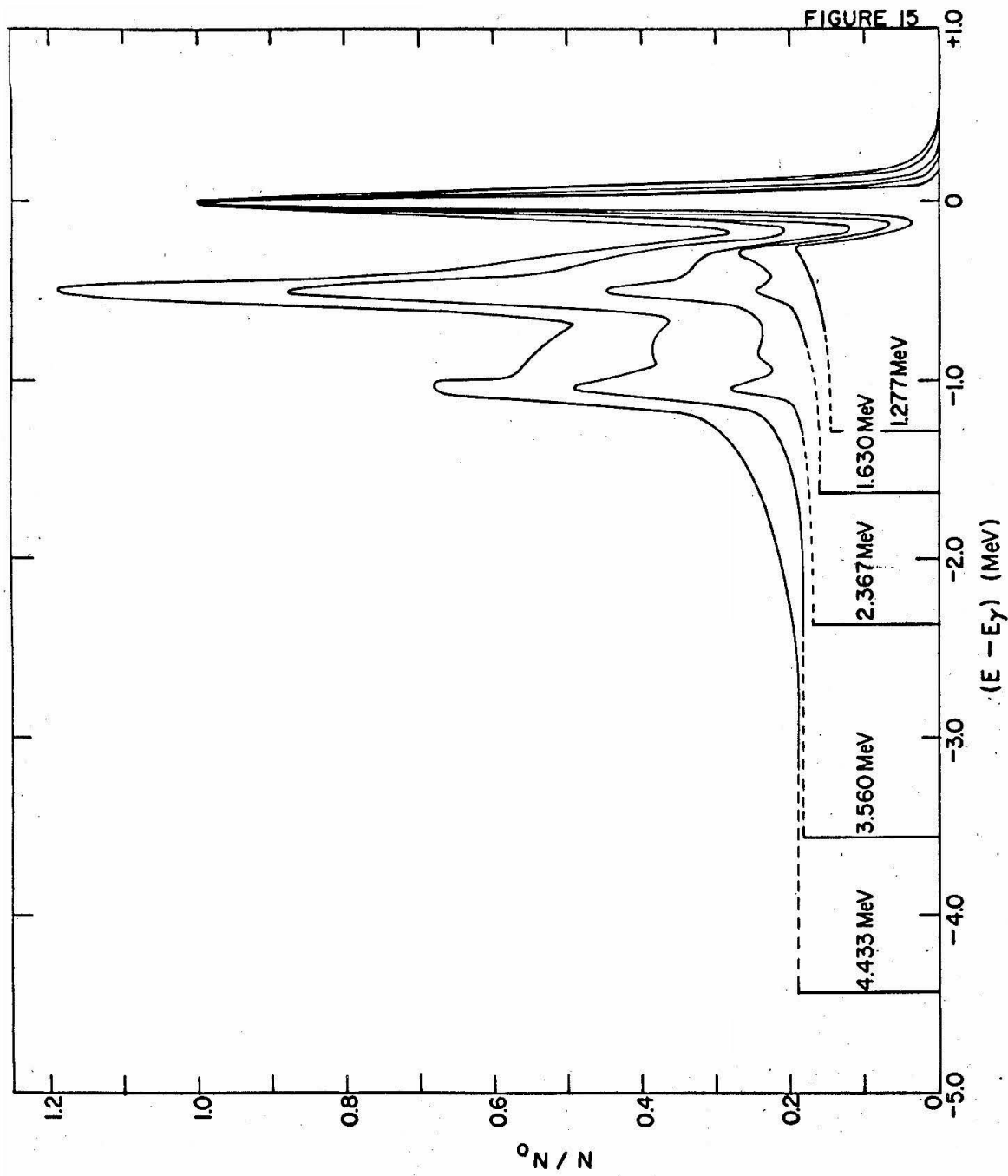


FIGURE 16: Response Functions for a Heavily Shielded 3" x 3" Well NaI(Tl) Crystal

These response functions, normalized to 1.000 at the full-energy peak, were obtained with the NaI(Tl) crystal heavily shielded and were used with interpolation to unfold the various components of the complex experimental spectra. The gamma-ray energy is indicated at the low-energy end of each function.

See text pages 74, 78 and 81.

-III-

FIGURE 16

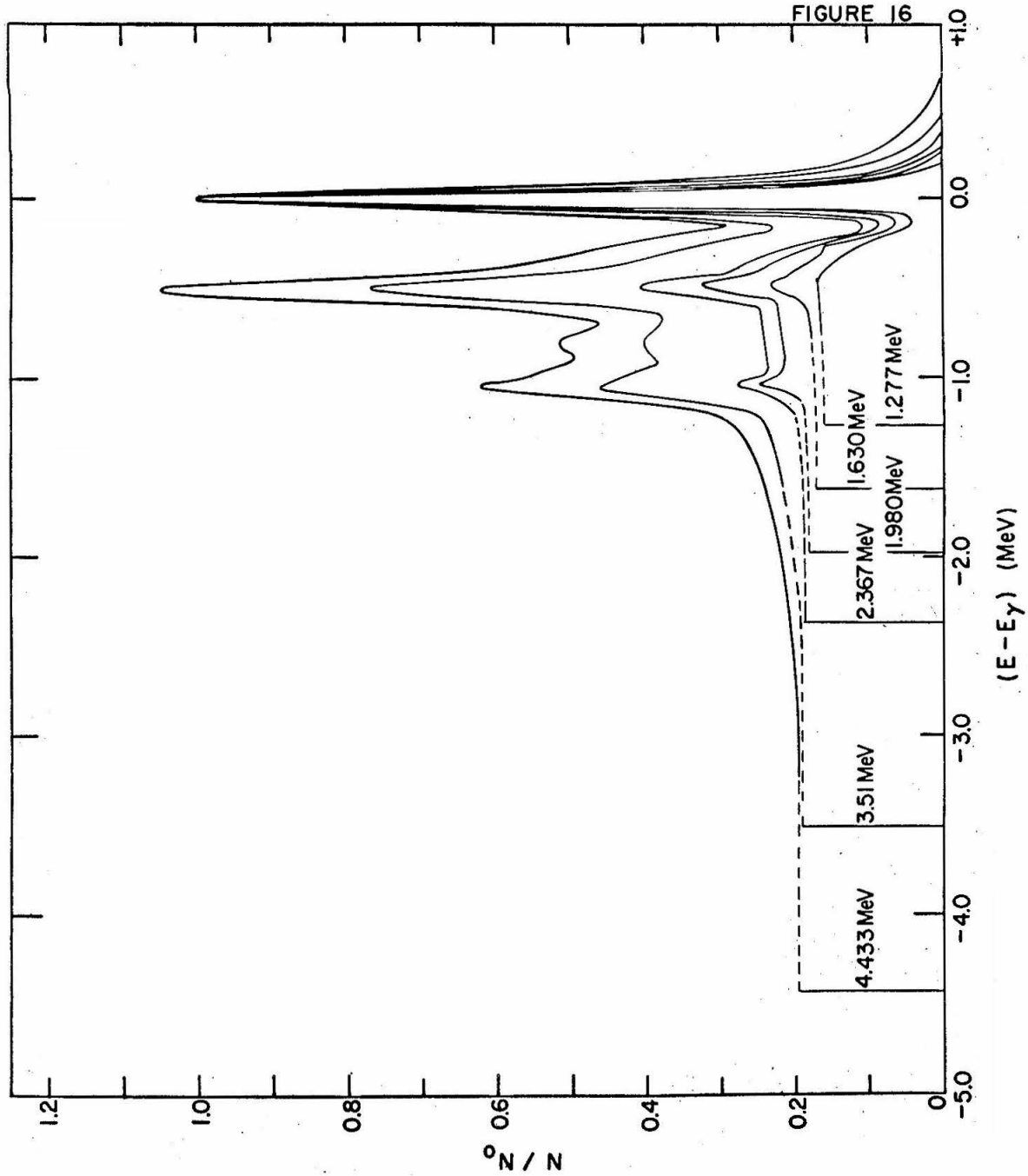


FIGURE 17: Alpha-Particle Stopping Cross Sections

The alpha-particle stopping cross sections (ϵ_a) for helium gas and nickel are plotted as a function of alpha-particle energy (E_a). These stopping cross sections were obtained by conversion from the proton stopping cross sections of Whaling (1958) by the relation

$$\epsilon_a(E_a) = R_a \epsilon_p\left(\frac{E_a}{3.97}\right)$$

where R_a is the effective squared-charge as also listed by Whaling (1958).

See text page 25.

FIGURE 17

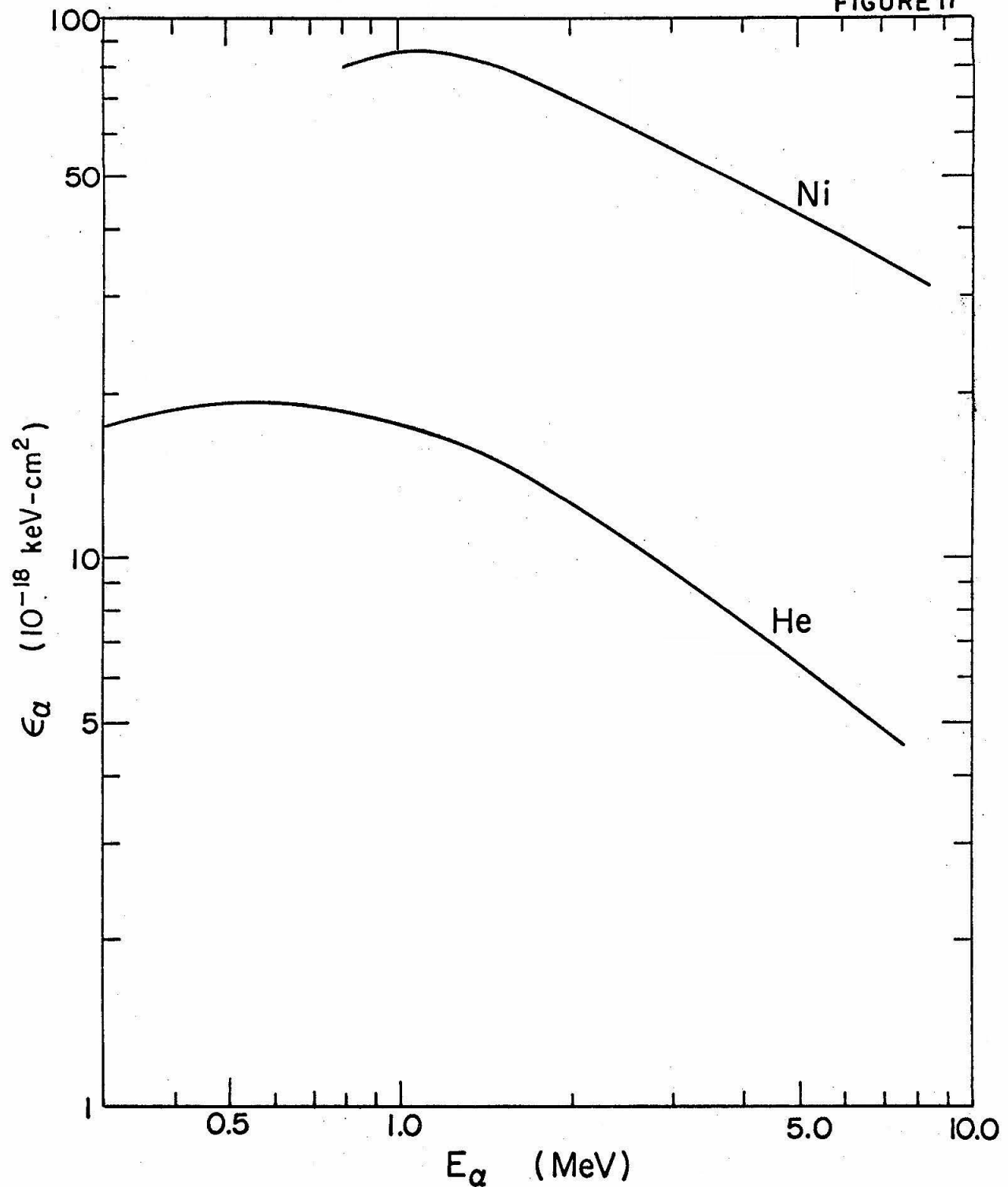


FIGURE 18: Gamma-Ray Doppler Shifts

The calculated maximum Doppler shift ($\Delta E_{\gamma} = E_{\gamma}(0^\circ) - E_{\gamma}$) for gamma rays from the $\text{He}^3(a, \gamma)\text{Be}^7$ reaction is plotted as a function of gamma-ray energy (E_{γ}). The measured Doppler shift is indicated at four points, showing the effect of the large solid angle of the crystal at 0° in slightly decreasing the observed shift compared to the shift calculated at 0° .

See text page 30.

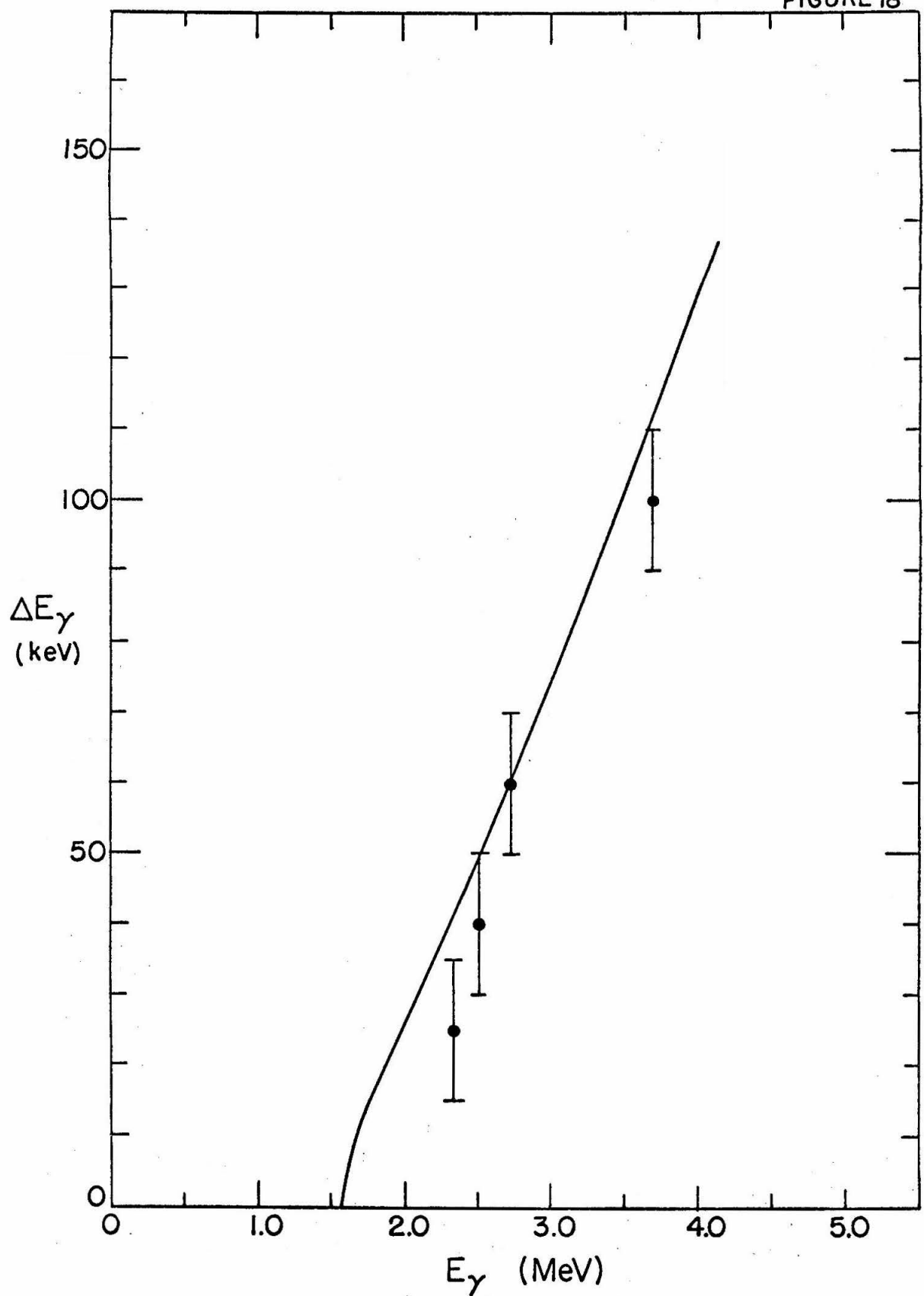


FIGURE 19: Data Reduction I

Figures 19 and 20 represent graphically the steps of data reduction for the case where $E_\alpha = 3.25$ MeV with the $3'' \times 3''$ NaI(Tl) crystal at 0° with respect to the alpha-particle beam. ($E_{cm} = 1248$ keV, $E_{\gamma 1} = 2890$ keV and $E_{\gamma 2} = 2458$ keV).

Figure 19(A) shows the appearance of the total spectra for the runs on the He^3 target and for the runs on the He^4 target, (approximately 1500 μC each).

Figure 19(B) shows the net experimental spectrum remaining when the He^4 spectrum is subtracted from the He^3 spectrum. Note the good agreement between the spectra in the region above channel 96, beyond the full-energy peak of γ_1 .

See text page 35.

FIGURE 19

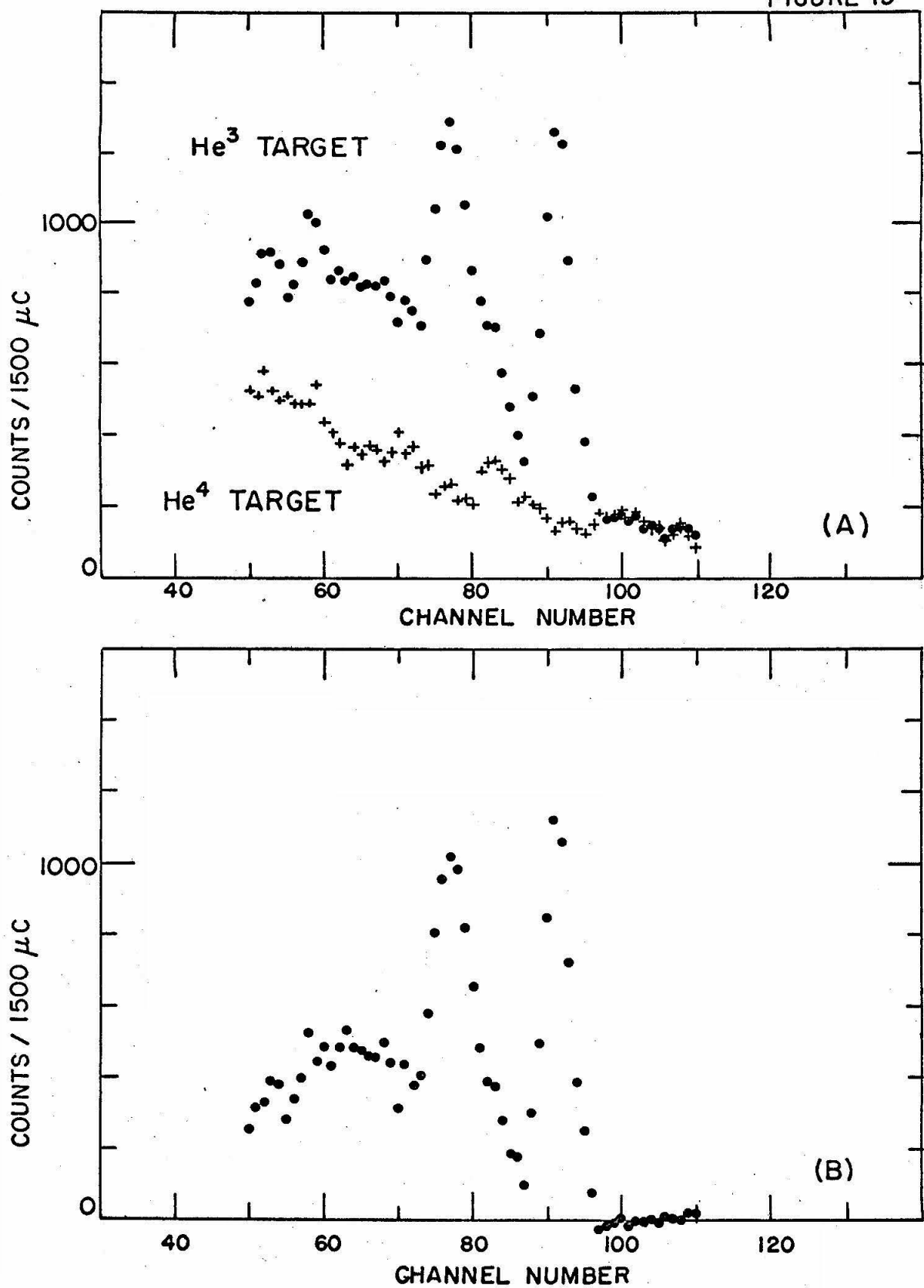


FIGURE 20: Data Reduction II

The net experimental spectrum of Figure 19(B) is plotted for comparison with the computed, least-squares fit (curve (1)) obtained using response functions interpolated from Figure 15. Curve (2) is the response function of a monoenergetic gamma ray with $E_{\gamma} = 2890$ keV, the crossover transition. Curve (3) is the cascade response function for two gamma rays with $E_{\gamma} = 2458$ keV and 432 keV, the cascade transition. Curve (4) is just that part of (3) which is due to summing. The normalizations of curves (2) and (3) are determined by the least-squares fit. Curve (1) is then just the sum of (2) and (3).

The cross sections for the ground-state (γ_1) transition and the cascade ($\gamma_2 + \gamma_3$) transition are now determined from these curves by assuming that the full-energy peaks are symmetric and determining the full-energy peak yields as

$$Y_{\phi_i} = 2 \sum_{\substack{(E-E_{\gamma_i}) > 0 \\ \gamma_1}}^{\text{500 kev}} N_i(E-E_{\gamma_i})$$

from curves (2) and (3) respectively. These yields are then related to the cross sections using the appropriate efficiencies and photo-fractions.

Note the contribution of the summing events to the full-energy peak and the lack of resolution of the various secondary peaks in the total response function.

See text page 38.

FIGURE 20

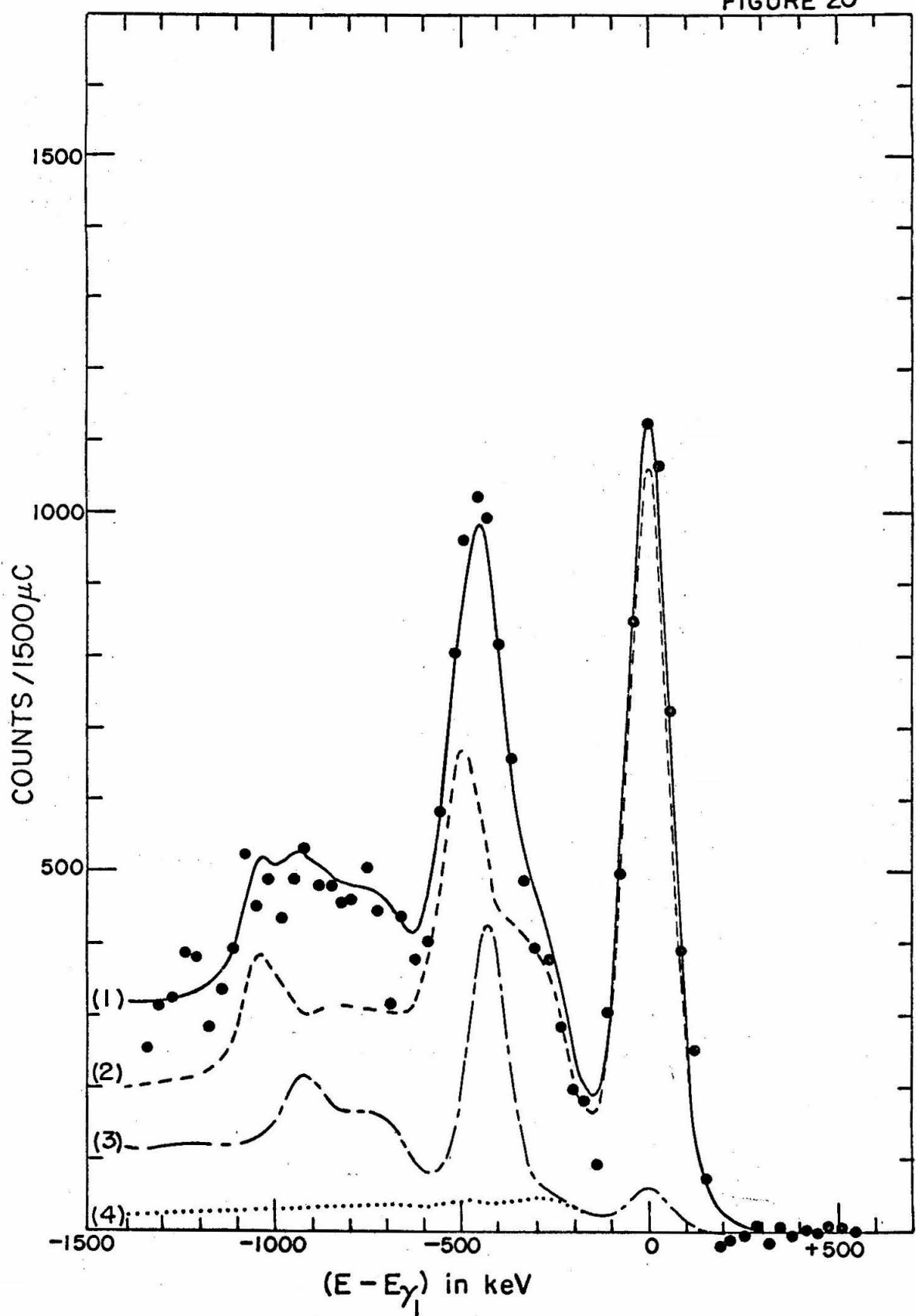


FIGURE 21: Total Direct-Capture Cross Section

The total direct-capture cross section (σ_{total}) is plotted as a function of the center-of-mass energy (E_{cm}) over the range of this experiment. The measured values of σ_{total} (see Table I) are plotted with their probable errors. The theoretically predicted cross section is shown by the solid line for the case of $R_0 = 2.80$ f, and $\theta_{3/2}^2 = 1.25$, $\theta_{1/2}^2 = 1.05$. See text page 54.

The solid square at 1380 keV and 2.5 μb is the coincidence measurement converted to σ_{total} . See text page 58.

FIGURE 21

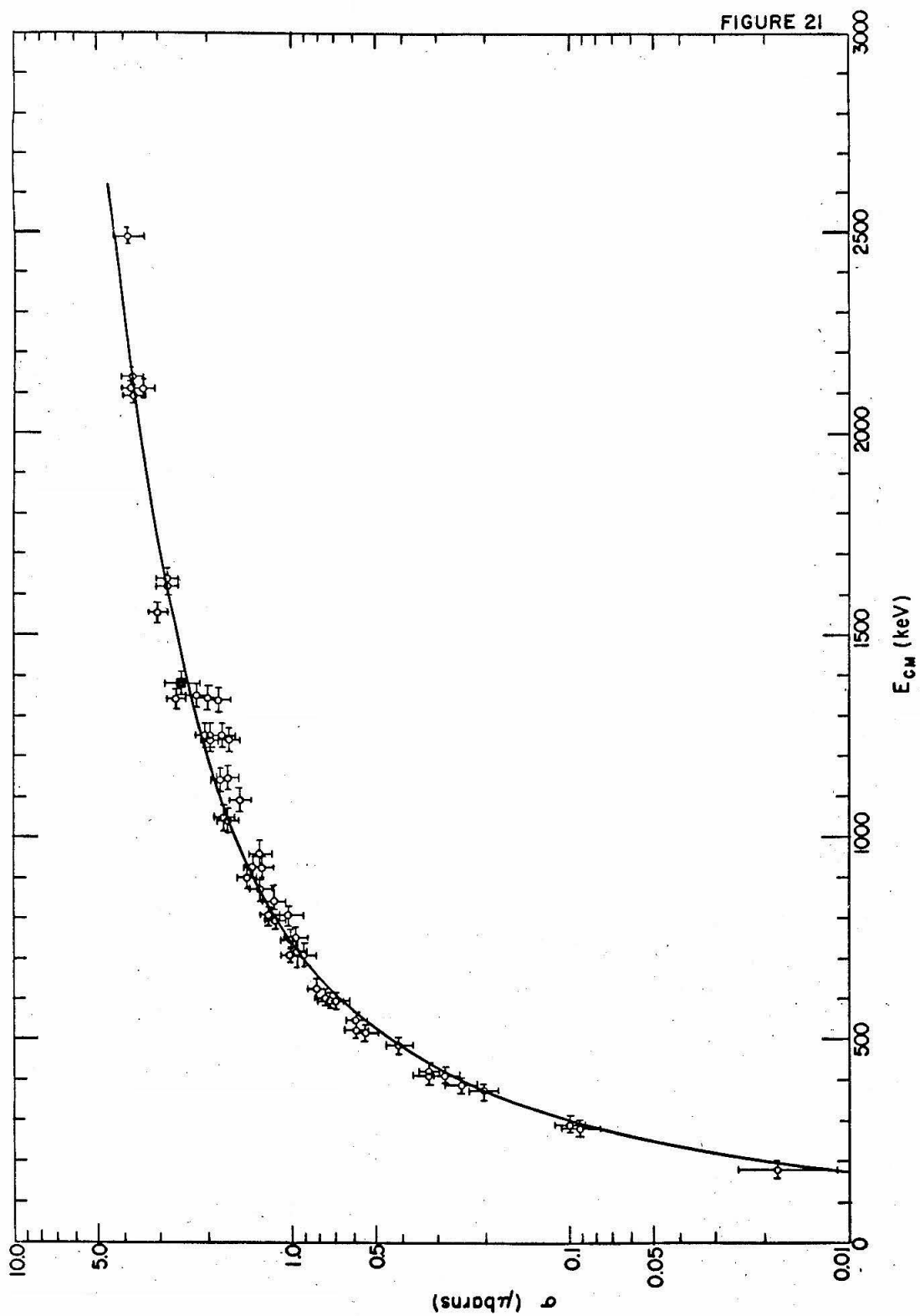


FIGURE 22: Partial-Wave Contributions to the Total Cross Section

The contributions of the various partial waves to the total calculated cross section are shown graphically for the range of energies covered in this experiment, for the same parameters used in Figure 21. The p-wave and f-wave contributions are lumped into the M1 and E2 cross sections; over the entire region these contributions, combined, never amount to more than about 2 per cent of the total cross section. The upward turn at the high energy end of the E2 curve is caused by the approach of the $^2F_{7/2}$ resonance at $E_{cm} = 2950$ keV.

See text page 57.

FIGURE 22

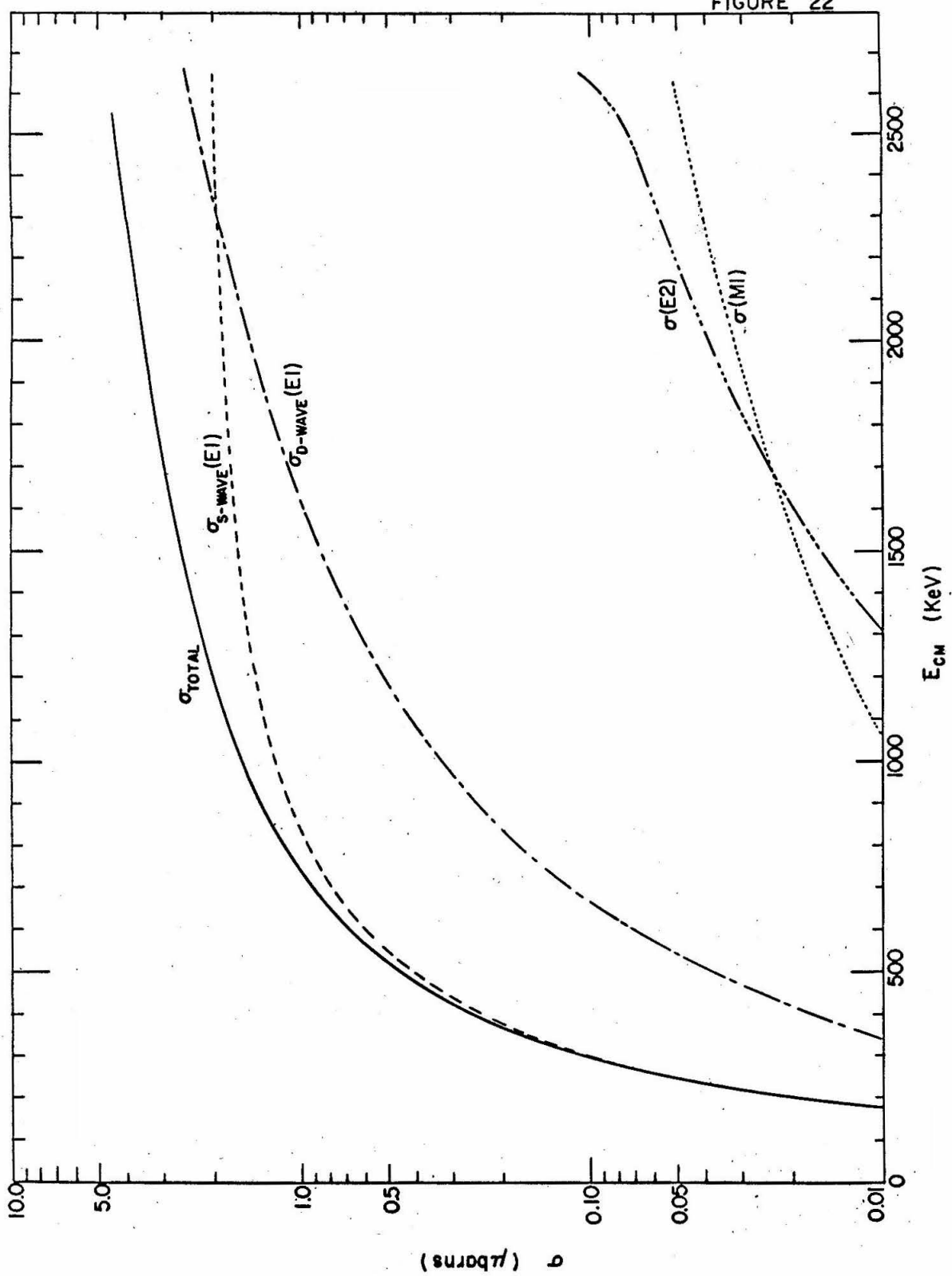


FIGURE 23: Branching Ratio

The branching ratio for the direct-capture gamma-ray transitions is plotted as a function of the center-of-mass energy. The branching ratio is defined as the ratio of the cascade cross section, $\sigma(\gamma_2)$, to the crossover cross section, $\sigma(\gamma_1)$. The experimentally determined values of this ratio are indicated with their probable errors. The solid curve is the theoretically predicted branching ratio using the same values for nuclear radius and the reduced widths as in Figure 21.

Assuming the branching ratio is constant over this energy region,

$$\bar{p} = 0.374 \pm 0.056$$

In other words, 73 per cent of the captures go directly to the ground state via γ_1 while 27 per cent go through the 432-keV excited state via γ_2 .

See text page 55.

FIGURE 23

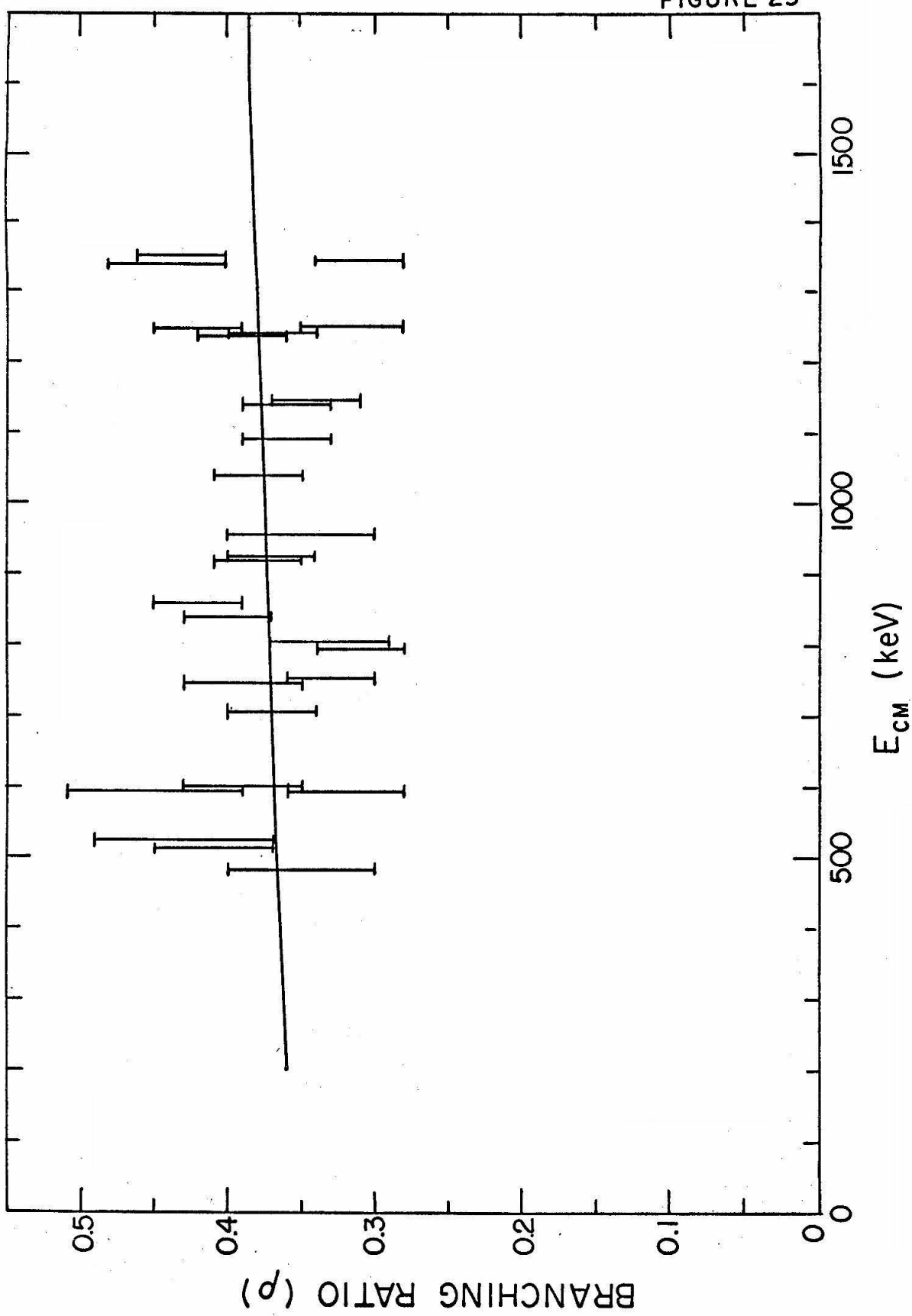


FIGURE 24: Angular Distribution Coefficients

The differential cross section has been shown to be of the form:

$$\frac{d\sigma(\theta)}{d\Omega} = \sigma_0(1 + a_1 \cos \theta + a_2 \cos^2 \theta + a_3 \cos^3 \theta + a_4 \cos^4 \theta).$$

The predicted behaviors of a_1 , a_2 , a_3 and a_4 are shown in this graph as functions of the bombarding energy (E_a) for a nuclear radius of 2.80 f. It is clear that over this whole region the coefficients remain fairly small. The behavior of the a_1 -coefficients at the high energy end of the curves is caused by the approach of the $^2F_{7/2}$ level in Be^7 at $E_a = 6.88$ MeV.

See text page 59.

FIGURE 24

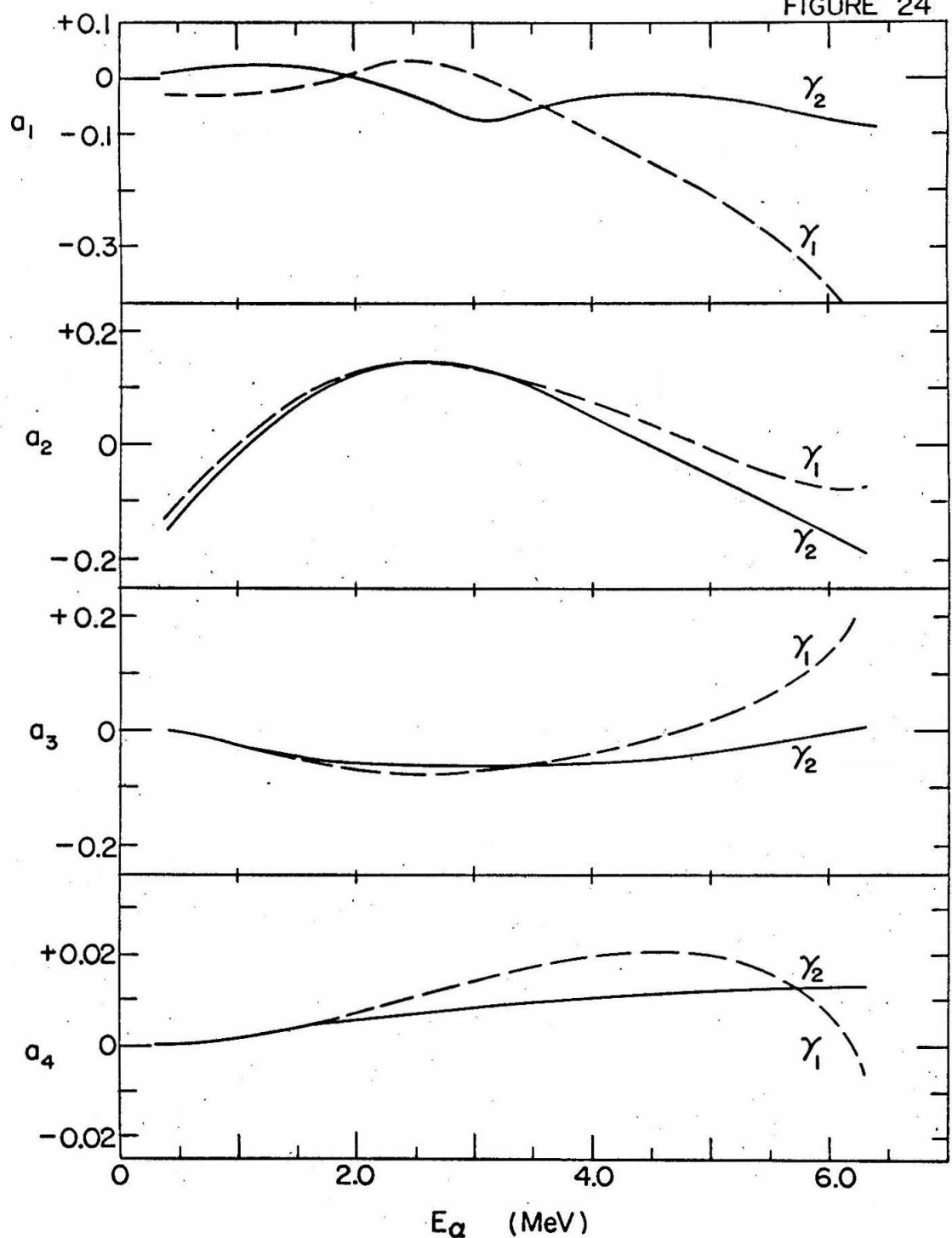


FIGURE 25: Cross-Section Factor

The cross-section factor, $S(E_{cm})$, is defined by Burbridge et al. (1957) as

$$S(E_{cm}) = \sigma(E_{cm})E_{cm} \exp [31.28 Z_1 Z_0 A^{1/2} E_{cm}^{-1/2}]$$

See text pages 53 and 59.

The experimentally determined cross sections have been converted to $S(E_{cm})$ and are plotted with their probable errors, (see also Table I). The solid curve again represents the theoretically predicted values of $S(E_{cm})$, obtained using the above equation to convert the curve in Figure 21.

The theoretical curve has been used to obtain a value for the low-energy cross-section intercept, S_0 , of

$$S_0 = 0.47 \pm 0.07 \text{ keV-barns.}$$

with a slope at the intercept, $(\frac{dS}{dE})_0$, of $(\frac{dS}{dE})_0 = -2.8 \times 10^{-4}$ barns. See text page 59.

-120-

FIGURE 25

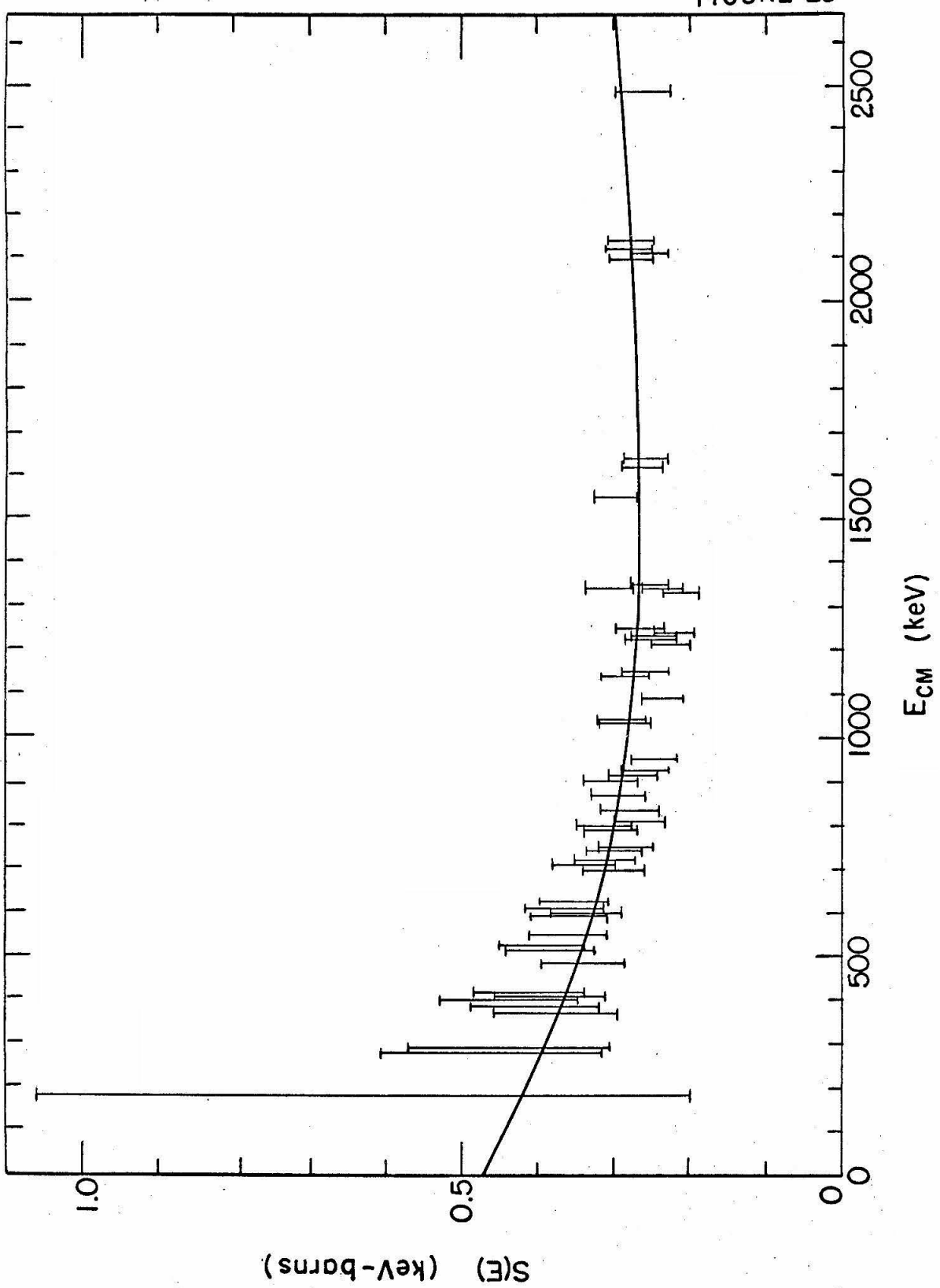


FIGURE 26: Proton-Proton Chain Terminations

The fraction of the He^4 produced through each termination of the proton-proton chain is plotted as a function of the temperature, assuming

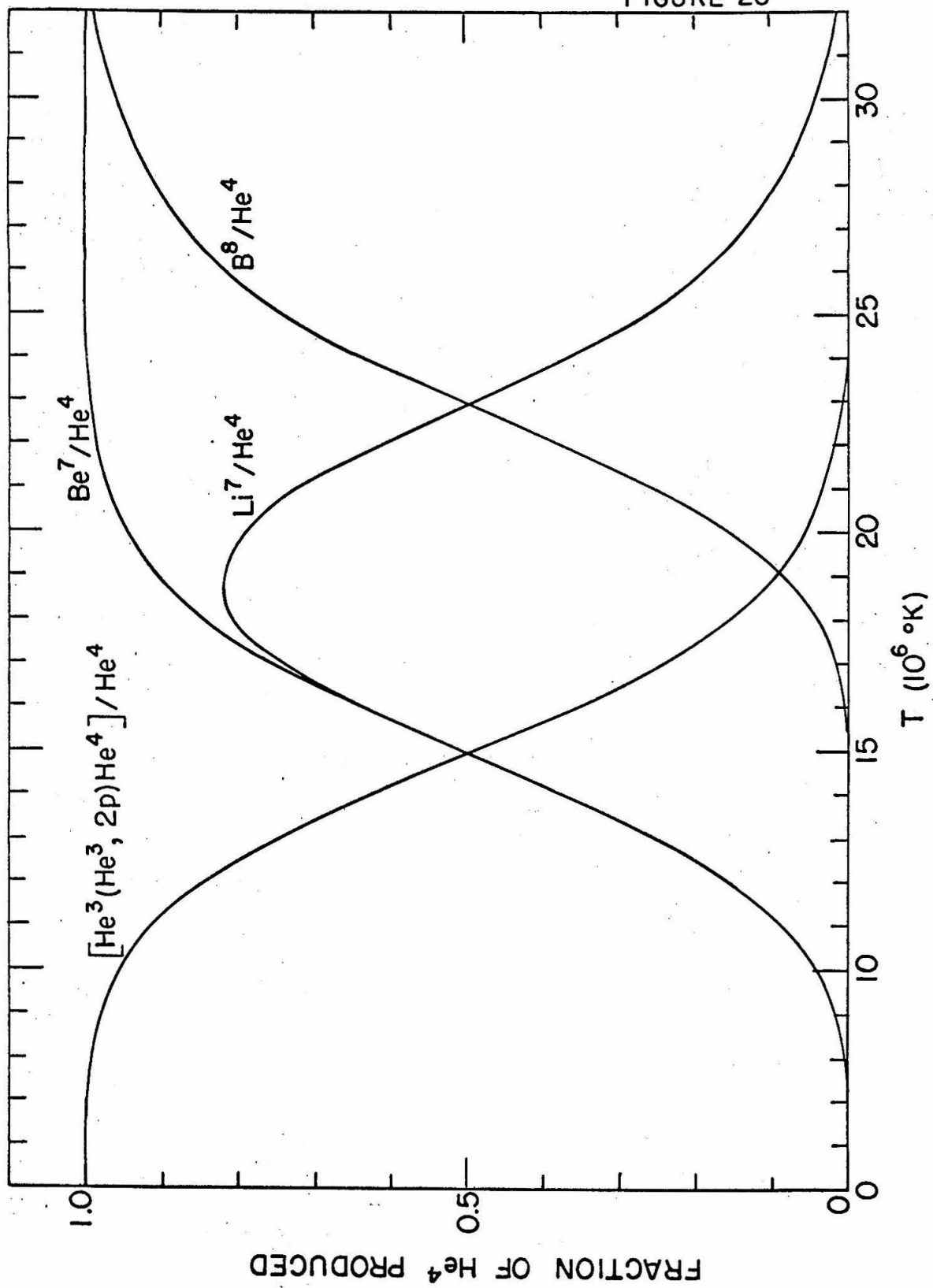
$$X_{\text{H}} = 0.50$$

$$X_{\text{He}}/X_{\text{H}} = 1.00$$

and using the cross-section factors listed in the text.

See text page 64.

FIGURE 26



FRACTION OF He^4 PRODUCED

FIGURE 27: Fraction of Terminations Through the $\text{He}^3(\alpha, \gamma)\text{Be}^7$ Reaction as a Function of the $(X_{\text{He}}/X_{\text{H}})$ Ratio and Temperature

The ratio $(\text{Be}^7/\text{He}^4)$, or the fraction of the proton-proton chain going to completion through the $\text{He}^3(\alpha, \gamma)\text{Be}^7$ reaction is plotted as a function of temperature for values of $(X_{\text{He}}/X_{\text{H}})$ of 0.25, 1.00 and 2.00, indicating the effect of the relative abundance of helium to hydrogen on the importance of this reaction as a step in the termination of the proton-proton chain.

Calculations (Bahcall et al., 1963) indicate that at present in the center of the sun,

$$T = 16.2 \times 10^6 \text{ }^{\circ}\text{K}$$

$$(X_{\text{He}}/X_{\text{H}}) \approx 2.00$$

so that at the center of the sun the proton-proton chain goes to completion through the $\text{He}^3(\alpha, \gamma)\text{Be}^7$ reaction approximately 84 per cent of the time.

For the sun as a whole at present (Fowler, 1962),

$$T_{\text{effective}} = 15 \times 10^6 \text{ }^{\circ}\text{K}$$

$$(X_{\text{He}}/X_{\text{H}}) \approx 1.0$$

so that the $\text{He}^3(\alpha, \gamma)\text{Be}^7$ reaction participates in about one-half of the terminations.

See text page 64.

FIGURE 27

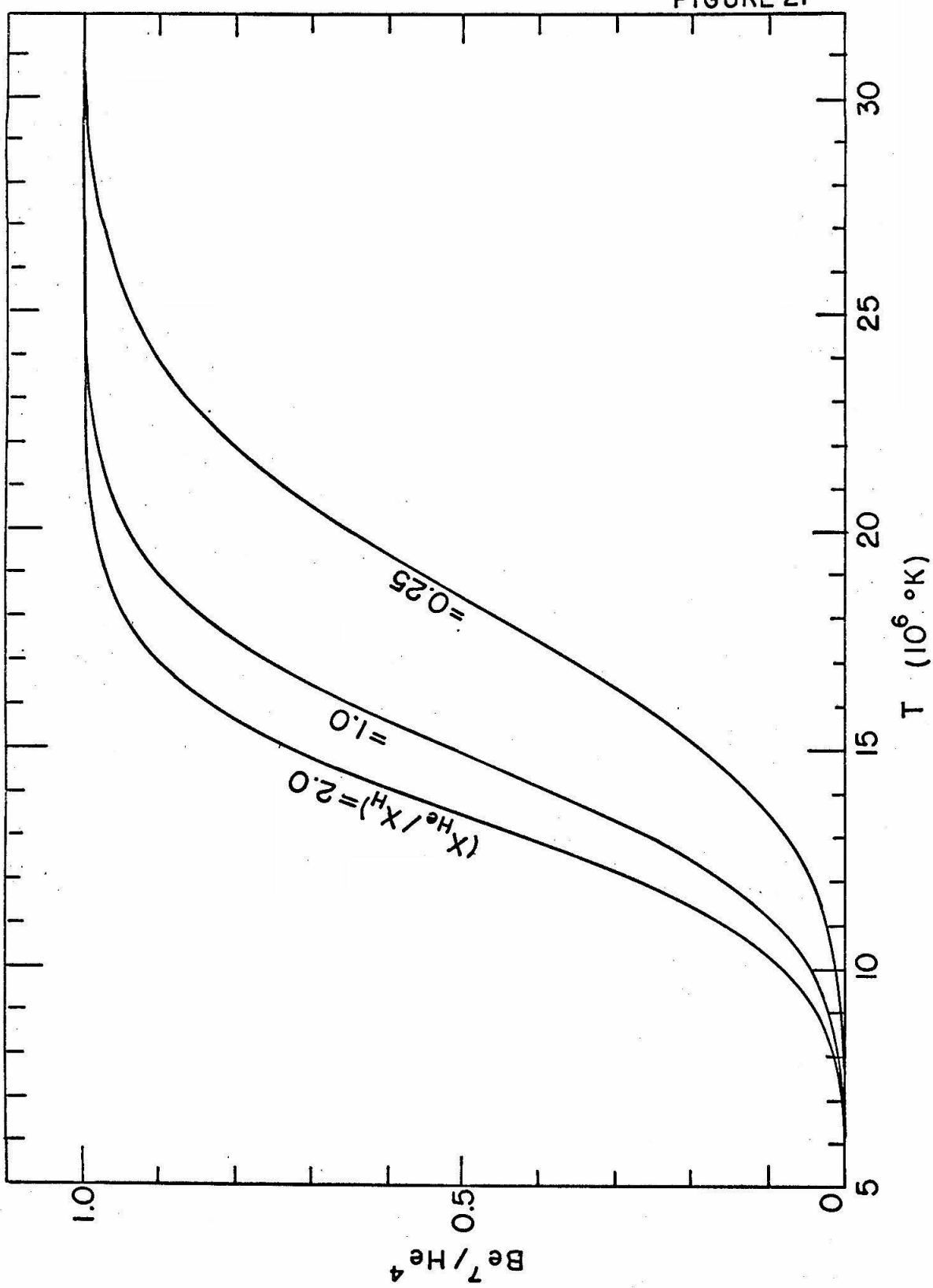


FIGURE 28: Proton-Proton-Chain Rate Factors

The He^4 -Production-Rate Factor, F_a , and the Energy-Generation-Rate Factor, F_ϵ , are plotted as a function of temperature, assuming $X_H = 0.50$ and $X_{\text{He}}/X_H = 1.00$.

F_a varies from 0.00 at low temperatures, where the proton-proton chain stops with the production of He^3 , producing no He^4 , to 0.50 at about 9×10^6 °K where the chain goes to completion only through the $\text{He}^3(\text{He}^3, 2p)\text{He}^4$ reaction, producing one He^4 for every two $\text{H}^1(p, \beta^+ \nu)D^2$ reactions, to 1.00 at higher temperatures where the chain is terminated through the $\text{He}^3(a, \gamma)\text{Be}^7$ reaction, producing one He^4 for every $\text{H}^1(p, \beta^+ \nu)D^2$ reaction. See text page 61.

F_ϵ varies from 0.255 at low temperatures, where the chain terminates with the production of He^3 , yielding only 6.68 MeV of useful energy for every $\text{H}^1(p, \beta^+ \nu)D^2$ reaction, to 0.500 at about 9×10^6 °K, where the chain goes to completion through the $\text{He}^3(\text{He}^3, 2p)\text{He}^4$ reaction producing 13.1 MeV of useful energy for every $\text{H}^1(p, \beta^+ \nu)D^2$ reaction, approaches a value of 0.98 under the influence of the $\text{He}^3(a, \gamma)\text{Be}^7(e^-, \nu)\text{Li}^7$ termination, but the onset of the $\text{He}^3(a, \gamma)\text{Be}^7(p, \gamma)\text{B}^8$ termination reduces this to approach an asymptotic value of 0.73 due to the energetic positron decay of B^8 .

See text page 65.

FIGURE 28

